Semiconductor optical amplifiers for ultra-wideband optical systems

Alexis Carbó Meseguer

Thèse

présentée pour obtenir le grade de Docteur
de Télécom SudParis

Spécialité : **Électronique and Communications**

Alexis Carbó Meseguer

Semiconductor Optical Amplifiers for ultra-wideband Optical Systems

Soutenue le 03 mai 2018 devant le jury composé de

Rapporteurs :
Alberto BONONI - Professeur - Université de Parme - Italie
Guang-Hua DUAN - Directeur général - 3SP Technologies - France

Examinateurs :
Didier ERASME - Professeur - Télécom ParisTech
Hélène DEBREGEAS - Docteure - Ingénieure - III-V Labs - France
Guy AUBIN - Ingénieur de recherche - C2N – France

Co-directeurs de thèse:
Jérémie RENAUDIER - Docteur - Ingénieur - Nokia Bell Labs
Yann FRIGNAC - Professeur - Télécom SudParis
Badr-Eddine BENKELFAT - Professeur - Télécom SudParis

2018TELE0010

Contents

Introduction

Over the past few decades the world has undergone a major revolution that has affected deeply the way we use communication networks. New services and applications have appeared such as social networks, online games or live streaming demanding a constant increase of channel capacity. Optical networks have evolved at par in order to cope with this demand of capacity and new technologies have been implemented: wavelength-division multiplexed (WDM), advanced modulation formats, coherent communications, and high efficiency forward error correction techniques are some examples of this evolution which have permitted to significantly increase the capacity of optical systems. But all these changes are still not enough and new technologies have to arise in order to tackle the challenges that will appear in the next future.

The increase of fibre capacity can be carried out by following one of these three independent axes: improving spectral efficiency (bps/Hz) by using more advanced digital signal processing techniques, increase of the optical bandwidth (Hz) and finally exploiting spatial division multiplexing (bps/Hz/m^2) that allows the possibility of launching several streams of data through the same optical fibre.

In the past, we have put a lot of effort in optimizing the different processing techniques with the aim of increasing the spectral efficiency of system. But we are reaching the fundamental limit, so it is becoming really challenging to further increase the capacity of the system by this means.

The motivation of this work is therefore moving to an orthogonal direction to further increase the fibre capacity. If we extend the bandwidth of an optical system, the channel capacity will increase since it depends linearly of the optical bandwidth of the system. Even considering a higher implementation penalty, the capacity can be notoriously increased by this technique as is assessed in

this work. But increasing optical bandwidth is not straight-forward since the current technology is not prepared yet for ultra-wideband signals.

In current systems, the technology most used worldwide to amplify the signal is Erbium Doped Fibre Amplification (EDFA). It is basically because this technology is the one that presents the best performance compared to other alternatives. But the major drawback of EDFA is optical bandwidth. This technology can successfully amplify two bands up to 35 nm, but it is extremely challenging to pull this band further. In the past other amplification systems have been used to increase the bandwidth of the signal such as all-Raman backwards amplification. This is a good solution to increase the bandwidth but with some drawbacks. The most important one is the matter of lumped amplification which is required in most types of optical systems. So, the use of this technology by itself has been never seriously considered and it is only deployed in hybrid EDFA and Raman solutions. So, discarded EDFA and all-Raman backwards pumping for the design of UWB systems, the other alternative is the use of semiconductor optical amplifiers (SOA).

The use of semiconductors to amplify the optical signal is not recent, but it was discovered many decades ago. However, it has never considered to compensate the fibre losses in transmission systems mainly because its high nonlinear nature. But the need of moving towards UWB systems has opened the door to recover this technology. In this work, we show that a well custom-designed SOA can not only amplify a wide band signal but also overcome some of the main drawbacks of the SOA in front of EDFA converting it as a serious alternative to take into account in order to become the next generation optical amplifier.

The use of SOA amplification changes completely the paradigm in the design of an optical system since all the impairments added by the SOA must be considered. That means that it is necessary to find an analytical or numerical model capable of characterizing the nonlinear nature of this device. Furthermore, this model must be the less complex as possible if we really want to simulate the performance a WDM system with a large number of channels.

The first immediate application we have found to assess the capabilities of a novel UWB SOA designed in the frame of the French project CALIPSO is data-centre interconnection. The data transmitted between data-centres is growing exponentially in last years, so companies such as Facebook are extremely interested in deploying ultra-wideband systems because they are able to cope with new traffic requirements in their networks. Furthermore the number of spans for DCI is limited, so the number of prototypes required for demonstration purposes is not very high.

This thesis is organized as follows. In the first chapter, some basic concepts of an optical transmission system are introduced, from the signal generation in the transmitter side to its reception and treatment in the receiver front-end.

In the second chapter we focus on the modelling of a semiconductor optical amplifier. We have decided to use the reservoir model because is a simple yet a powerful solution to study the nonlinear nature of a SOA amplifier. In the first part this model is introduced and its main parameters are experimentally extracted from a state-of-the-art SOA. Then, taking advantage of a high-sampling rate oscilloscope, we extract some important parameters that governs the dynamic regime of an SOA such as the linewidth enhancement factor from the temporal traces of a modulated signal after its pass though the SOA. Finally, some measurements are done with more advanced modulation formats and the matter of modelling a WDM transmission system with SOA amplification is introduced.

Next chapter is devoted to introducing the concept of ultra-wideband transmissions. Then, a novel UWB SOA designed in the frame of the French CALIPSO project is characterized putting emphasis in the differences with the state-of-the-art SOA. In this chapter a technique that could be use in the future to compensate the fibre nonlinearities in ultra-wideband systems is also introduced: digital multicarrier multiplexing.

Finally, in the last chapter we show the potential of the novel UWB SOA to become the next generation optical amplifier for data-centre-interconnect applications. Firstly, a transmission over 100 km is assessed using the novel UWB SOA. We have successfully transmitted up to 115.9 Tbps in a 100-nm continuous transmission bandwidth. And then, the UWB SOA stability is verified with real time line cards, both in C and in L bands, running PDM-16QAM at 250Gb/s per wavelength in a 24-hour soak test between two points of presence (POP) of Facebook deployed in the Paris area.

In the next future, the design of SOA amplifiers will be improved until its performance becomes comparable with EDFA. The future perspective of this technology is therefore the expansion to other applications such as metro and long-haul systems using the UWB SOA by itself or in hybrid SOA and Raman solutions.

Résumé

Au cours des dernières décennies, le monde a subi une révolution majeure qui a profondément affecté la façon qu'on utilise les réseaux de communication. De nouveaux services et applications sont apparus tels que les réseaux sociaux, les jeux en ligne ou le streaming en direct, qui ont besoin d'une augmentation constante de la capacité des systèmes de transmission. Les réseaux optiques ont évolué au pair pour faire face à cette demande de capacité et de nouvelles technologies ont été mises en place : WDM, formats de modulation avancés, communications cohérentes et techniques de correction d'erreurs à haut rendement sont quelques exemples de cette évolution qui a permis d'augmenter considérablement la capacité des systèmes optiques. Mais tous ces changements ne sont pas suffisants et de nouvelles technologies doivent apparaître pour relever les défis qui apparaîtront dans le futur.

L'augmentation de la capacité de fibre peut être réalisée en suivant un de ces trois axes indépendants : améliorer l'efficacité spectrale (bps / Hz) en utilisant des techniques de traitement de signal numérique plus avancées, augmenter la bande passante optique (Hz) et aussi exploiter le multiplexage spatial (bps / Hz / m2) qui permet de lancer plusieurs flux de données à travers la même fibre optique.

Dans le passé, on a mis beaucoup d'effort pour optimiser les différentes techniques de traitement du signal afin d'augmenter l'efficacité spectrale du système. Mais on est en train d'atteindre une limite fondamentale, donc il sera vraiment difficile d'augmenter plus la capacité du système de cette façon.

La motivation de ce travail se déplace vers une direction orthogonale afin d'augmenter encore plus la capacité de la fibre. Si on allonge la bande passante d'un système optique, la capacité du canal augmentera car elle dépend linéairement de la bande passante optique du système. Même en

considérant une pénalité de mise en œuvre plus élevée, la capacité peut être notoirement augmentée par cette technique. Mais l'augmentation de la bande passante optique n'est pas simple puisque la technologie actuelle n'est pas encore préparée pour les signaux à ultra large bande passante (UWB).

Dans les systèmes actuels, la technologie la plus utilisée pour amplifier le signal optique est l'amplification à fibre dopée à l'erbium (EDFA). C'est essentiellement parce que cette technologie est celle qui présente les meilleures performances par rapport aux autres alternatives. Mais l'inconvénient majeur de l'EDFA est la bande passante optique. Cette technologie peut amplifier avec succès deux bandes de jusqu'à 35 nm, mais c'est extrêmement difficile d'aller plus loin. Dans le passé, d'autres systèmes d'amplification ont été utilisés pour augmenter la bande passante du signal, comme l'amplification backward Raman. Elle est une bonne solution pour augmenter la bande passante mais avec quelques inconvénients. Le plus important est la question de l'amplification localisée qui est requise dans la plupart des types de systèmes optiques. L'utilisation de cette technologie n'a jamais été sérieusement envisagée et elle n'est utilisée que dans les solutions hybrides EDFA et Raman. Ainsi, abandonné EDFA et Raman pour la conception de systèmes de large bande passante, l'autre alternative est l'utilisation d'amplificateurs optiques à semi-conducteurs (SOA).

L'utilisation de semi-conducteurs pour amplifier le signal optique n'est pas récente, mais a été découverte il y a plusieurs décennies. Cependant, elle n'a jamais été utilisée pour compenser les pertes de la fibre dans les systèmes de transmission principalement par sa nature non linéaire élevée. Mais la nécessité de s'orienter vers les systèmes UWB a ouvert la voie à la récupération de cette technologie. Dans ce travail, on montre qu'un SOA bien conçu peut non seulement amplifier un signal à très large bande, mais également surmonter certains des principaux inconvénients de la SOA face à EDFA en le convertissant en une alternative sérieuse à prendre en compte pour devenir l'amplificateur optique de nouvelle génération.

L'utilisation de l'amplification SOA change complètement le paradigme dans la conception d'un système optique puisque toutes les dégradations ajoutées par la SOA doivent être considérées. Cela signifie qu'il est nécessaire de trouver un modèle analytique ou numérique capable de caractériser la nature non linéaire de ce dispositif. De plus, ce modèle doit être le moins complexe possible si on veut vraiment simuler la performance d'un système WDM avec un grand nombre de canaux.

Cette thèse est organisée comme suit. Dans le premier chapitre, quelques concepts de base d'un système de transmission optique sont introduits, depuis la génération du signal côté émetteur jusqu'à sa réception et son traitement au récepteur.

Le but du deuxième chapitre est de trouver un modèle capable de caractériser les performances d'un amplificateur optique à semi-conducteur dans le contexte de la conception de systèmes de transmission optique WDM.

Le modèle sélectionné est le modèle de réservoir qui est présenté et évalué. Ce n'est pas le modèle existant le plus précis mais il présente un bon compromis entre complexité et précision.

On a divisé l'évaluation en deux parties différentes. Dans la première partie, on a étudié le régime statique d'un SOA et on a extrait expérimentalement tous les paramètres importants tels que le gain et la puissance de saturation en fonction de la longueur d'onde et de la puissance d'entrée d'un SOA à la pointe de la technologie acheté chez Thorlabs. Dans la deuxième partie, quelques expériences ont été considérées pour analyser son régime dynamique. On a mesuré la réponse du bruit d'intensité relative (RIN) du SOA qui nous a permis d'estimer la durée de vie de la porteuse du SOA en 200 ps. En comparant les résultats expérimentaux avec ceux fournis par le modèle de réservoir, on a observé un bon ajustement qui nous permet conclure qu'il peut estimer avec succès la dynamique du SOA.

Enfin, on a extrait le facteur d'accroissement de la largeur de ligne (linewidth enhancement factor) du SOA à la pointe. Avec un récepteur cohérent équipé d'un oscilloscope à haut taux d'échantillonnage, on a obtenu quelques traces temporelles d'une signal OOK après avoir traversé une SOA. On a extrait l'amplitude et la phase du signal en utilisant des techniques de traitement du signal, puis on a obtenu ce paramètre en ajustant les traces expérimentales avec celles fournies par le modèle. Ce valeur a été estimé en 5. C'est la première fois que le facteur d'amélioration de la largeur de ligne d'un amplificateur optique à semi-conducteur a été estimé en utilisant un récepteur cohérent obtenant des résultats similaires à ceux estimés en utilisant des test-beds beaucoup plus complexes.

Une fois ce dernier paramètre a été obtenu, on a évalué le modèle en comparant les traces expérimentales avec celles obtenues en simulations numériques. On a vu que le modèle de réservoir peut parfaitement s'adapter aux courbes expérimentales d'amplitude et de phase pour les régimes linéaires et faiblement non linéaires. Le modèle commence à être imprécis dans les régimes hautement non linéaires, spécifiquement pour la phase du signal.

Pour les formats de modulation plus complexes, on a observé que le modèle offre encore une bonne estimation de la dynamique SOA pour les régimes linéaires et faiblement non-linéaires. Bien que pour les hauts régimes non linéaires le modèle de réservoir est trop simple et quelques considérations supplémentaires pourrait être considéré pour fixer ses imprécisions. Néanmoins pour les systèmes de transmission où le SOA sera principalement utilisé dans les régimes linéaires et faiblement non linéaires, le modèle de réservoir a été montré comme une bonne alternative qui probablement sera exploité dans le future pour modéliser des systèmes de transmission UWB avec SOA.

D'un autre côté, dans la dernière partie du chapitre, on souligne l'importance de l'utilisation de fibres de décorrélation dans la configuration de

transmission WDM pour assurer la décorrélation entre les différents canaux. Cette étude peut être utile dans les expériences de laboratoire où le nombre de modulateurs utilisés est généralement limité et les différents canaux de chargement sont donc partialement ou totalement corrélés. Des simulations numériques ont été réalisées pour déterminer la longueur minimale de la fibre de décorrélation qui a été établie en 25 km de SSMF lors de la transmission d'au moins 60 canaux. Puis plusieurs expériences ont été réalisées pour la valider. On a observé comment la bobine supplémentaire a aidé à décorréler les canaux et ainsi réduire la pénalité de la SOA.

Le prochain chapitre est consacré à l'introduction du concept des transmissions à très large bande. Dans une première section, un UWB SOA a été introduite et caractérisée. Pour ce nouveau dispositif, une structure de diversité de polarisation a été choisie dans le but à la fois d'augmenter la puissance de saturation de sortie et aussi de minimiser le bruit par rapport au SOA introduit dans le chapitre précédent.

Le SOA résultant a un gain plat de 20 dB dans une bande passante d'au moins 100 nm. La puissance de saturation a été considérablement augmenté permettant au UWB SOA de fonctionner avec des puissances de sortie plus élevées. Les pertes de couplage ont été réduites pour atteindre des valeurs de NF jusqu'à 6 dB.

Ensuite, le module a été caractérisé expérimentalement pour quantifier la pénalité introduite pour le SOA dans les différents régimes de fonctionnement. On a obtenu la mesure de la pénalité en fonction de la puissance d'entrée pour une longueur d'onde et on a vu qu'elle peut être généralisée pour n'importe quelle longueur d'onde donnée en tenant en compte le concept de puissance de saturation d'entrée. On a évalué que pour DP-QPSK et DP-16QAM, la puissance de saturation d'entrée peut être surmontée de 5 dB sans une pénalité significative. C'est une conclusion très positive car elle permet de considérer que ce nouvelle UWB SOA est capable de transmettre en systèmes WDM ce qui le fait devenir une alternative à l'EDFA pour devenir l'amplificateur optique de nouvelle génération.

Finalement, on a étudié la compensation non linéaire des fibres pour les systèmes UWB. Il a été démontré que les technologies actuelles utilisées pour la compensation des effets non linéaires de la fibre sont moins efficaces en systèmes à large bande passante. Ainsi, un nouveau schéma de modulation a été proposé dans la littérature afin d'optimiser le débit de symboles du signal pour atteindre un optimum du point de vue des non linéarités de la fibre: le multiplexage digital de porteuses. Les modèles analytiques ont affirmé que les avantages de cette approche peuvent être pris en compte dans les systèmes UWB. Cependant, nos expériences et simulations numériques n'ont pas montré la même tendance. On attribue cette différence au fait que le modèle analytique ne peut pas prendre en compte tous les effets possibles: les limitations Tx / Rx ou les problèmes d'un algorithme CPE standard pour éliminer le bruit de phase non linéaire. D'un autre côté, les expériences en laboratoire ont également

certaines limites pratiques. Par exemple, l'incapacité de moduler indépendamment tous les canaux de chargement qui peut avoir un important impact. Pour résoudre ce problème, les expériences devraient être effectuées dans un système réel avec des canaux complètement indépendants. Néanmoins, il sera difficile à réaliser puisque on a vu que le gain de cette approche n'est pas assez élevé pour tirer la mise en œuvre de cette approche dans les transpondeurs de la prochaine génération. En fait, toutes les expériences effectuées sont en ligne avec le fait que le gain relié au multiplexage digital de porteuses est clairement réduit pour les formats de modulation avancés, ce qui seront utilisés dans les systèmes de transmission de la prochaine génération.

La première application immédiate que on a trouvée pour évaluer les capacités de la nouvelle architecture SOA conçue dans le cadre du projet français CALIPSO est l'interconnexion des centres de données. Les données transmises entre ces centres ont connu une croissance exponentielle ces dernières années, qu'il a fait que des entreprises telles que Facebook sont extrêmement intéressées par le déploiement de systèmes à bande ultralarge, parce qu'elles sont capables de faire face aux nouvelles exigences de trafic de leurs réseaux. Dans ce travail, la première transmission de 100 nm de bande passante continue sur 100 km de fibre EX2000 est démontrée avec un débit total net de 115,9 Tbps. Cette expérience a permis de mesurer pour la première fois toutes les dégradations possibles associées à une bande passante aussi large, comme l'effet SRS d'une fibre de transmission optique.

Ensuite, on a également démontré la transmission d'un débit moyen de 475 Gb / s sur un système ultra large bande SOA amplifié à deux travées (> 100nm) entre deux points de présence (POP) de Facebook déployés dans la région parisienne. De plus, les performances avec des cartes de ligne en temps réel, en bande C et en bande L, fonctionnant sous PDM-16QAM à 250 Gbits / s par longueur d'onde, démontrent les performances extrêmement stables du SOA UWB sur un test de stabilité de 24 heures.

Avec cet essai sur le terrain, on a démontré toutes les capacités de la SOA pour devenir l'amplificateur optique de prochaine génération. Néanmoins, d'autres améliorations devraient améliorer ses performances. Une approche possible consiste à concevoir un système d'amplification hybride Raman et SOA. L'amplificateur hybride peut résoudre le problème de la figure de bruit plus élevé dans les systèmes SOA mais aussi la question de l'amplification localisée pour les réseaux avec des ROADM. C'est une bonne approche à utiliser dans les années à venir qui ouvre la voie à la mise en œuvre du UWB SOA pour les liaisons métropolitaines et longues distances.

Chapter 1. Optical coherent transmission system

1.1. *Introduction*

In this first chapter, basic concepts of an optical transmission system are explained. A coherent optical transmission system is divided in three main parts: the transmitter, the channel and the receiver. The transmitter is the part where the data to be transmitted is generated and transferred into the light domain. Some multiplexing techniques are exploited at the transmitter side to maximize the throughput launched into the transmission line such as Polarization Division Multiplexing or Wavelength Division Multiplexing. The channel is composed by few spans of optical fibre. The number of spans depends basically of the reach of the application: it can range from only one or two spans in data-centre-interconnect (DCI) networks to several tens of them in long-haul and submarine systems. The spans of fibre are separated by optical amplifiers which compensate the losses produced along the optical fibre. Both amplifiers and fibre degrade the signal either by adding noise or by distorting the signal with nonlinearities. These effects determine the maximum throughput that can be transmitted over a certain reach. Finally, the receiver is the part where the signal is coherently acquired and treated to recover the original data. Several digital processing techniques are used to accomplish this objective, which are explained in next sections. The development of error correction codes has permitted to increase significantly the transmission distance. These codes add redundancy in a smart way in the transmitted sequence of data to allow the possibility of correcting the errors produced in the decoding of the signal. Finally, in this chapter are also explained some signal

shaping techniques such as pulse and constellation shaping which have effectively been used to increase the spectral efficiency.

In Fig. 1.1 shows a basic example of an optical transmission system where we can easily delimit each of the three parts explained before.

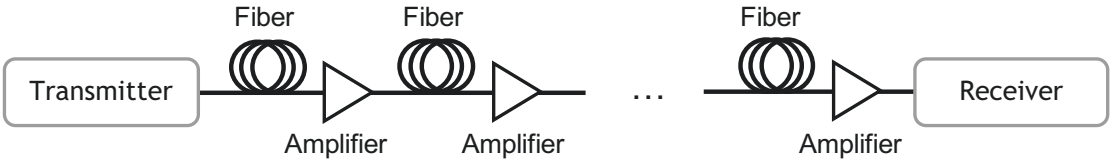

Fig. 1.1: Optical transmission system

1.2. *Optical transmitter*

1.2.1 Optical modulator

The optical modulator is the component that transfers the electrical data into the light domain. There are many approaches [1] that are used to accomplish this purpose such as direct modulated lasers (DML), electro-absorption modulators (EAM) or Mach-Zehnder Modulator (MZM). This work focuses on the last approach thus it has usually considered as the preferred one for coherent systems.

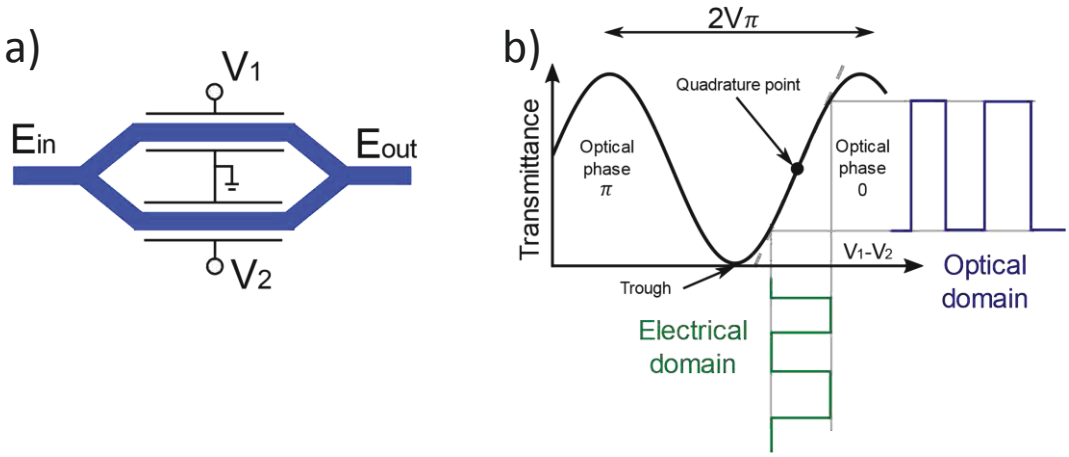

Fig. 1.2: Mach-Zenhder modulator scheme in (a) and MZM biased at the quadrature point in (b)

The apparatus was named MZM since the physicists L. Mach [2] and L. Zehnder [3] proposed a first approach in early 80s. It is an interferometer composed of two different arms of Lithium Niobate which are coupled as observed in Fig. 1.2-a). The modulation occurs by applying a different electric driving voltage to one or the two arms of the MZM. Electrical current changes the refractive index of the strips which causes that light propagates in the two arms at different speeds. The difference of phase generates an interferometric effect which creates constructive and destructive interferences. This effect modifies the amplitude of the input light and allow its modulation. For

transmission purposes, the input signal to be modulated is the optical carrier generated by an external laser.

The input-output characteristic of a MZM is given by:

$$E_{out} \propto E_{in} \cos\left(\pi \frac{V_1 - V_2}{2V_\pi}\right) \tag{1.1}$$

Where E_{in} and E_{out} are the input and output optical signals respectively, V_1 and V_2 are the voltages applied to the two arms and V_π is a characteristic driven voltage of the MZM modulator. In Fig. 1.2-b) the transmittance function of the MZM is shown, which depends of the difference between V_1 and V_2. Chosen the good values of these voltages, the MZM can be biased to a selected quiescent point. In the example of in Fig. 1.2-b), the bias point is set to the quadrature point. Working at this point the transfer function can be considered linear in a small-signal domain and the amplitude of the optical signal can be modulated. The amplitude of the electrical signal must be correctly bounded to avoid working in the nonlinear regime which would generate undesired distortions.

Advanced modulation formats also require modulating the optical phase. It is done by biasing the MZM at the trough point. At this quiescent point, optical phase can be modulated between 0 and π as it can be noticed in the figure.

1.2.2 Polarization division multiplexing

Polarization division multiplexing is a technique that consists in encoding two different signals in each of the two orthogonal polarizations of the light field and thus, doubling the rate launched into the channel. First polarization division scheme was proposed in 1992 by G. Evangelides for ultralong haul soliton transmission [4] and in 1996 A. Cheaplyvy et al successfully transmitted 1 Tb/s thanks to PDM [5]. The scheme is shown in Fig. *1.3*. The laser to be modulated is split in two different beams. Each beam is launched to an independent MZM driven by two independent DACs, which provides two different streams of optical data. Finally, one beam is rotated 90 degrees before the recombination with a polarization beam combiner (PBC).

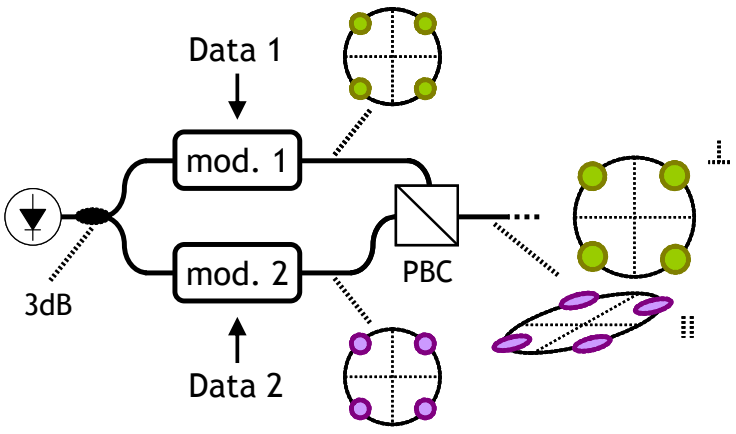

Fig. 1.3*: PDM transmitter scheme*

1.2.3 Wavelength division multiplexing

Wavelength Division Multiplexing (WDM) is a technique which is considered a key breakthrough in optical communications since it has provided a significant increase of throughput in optical systems. The principle of WDM consists in multiplexing several independently modulated channels at different wavelengths with the purpose of being transmitted simultaneously over the same optical fibre [6]. The total throughput is therefore the addition of all the individual throughputs of the whole bunch of channels. Furthermore, the use of pulse shaping techniques, with limits the optical bandwidth of a channel, has helped to increase even more the bandwidth efficiency of the WDM transmission system.

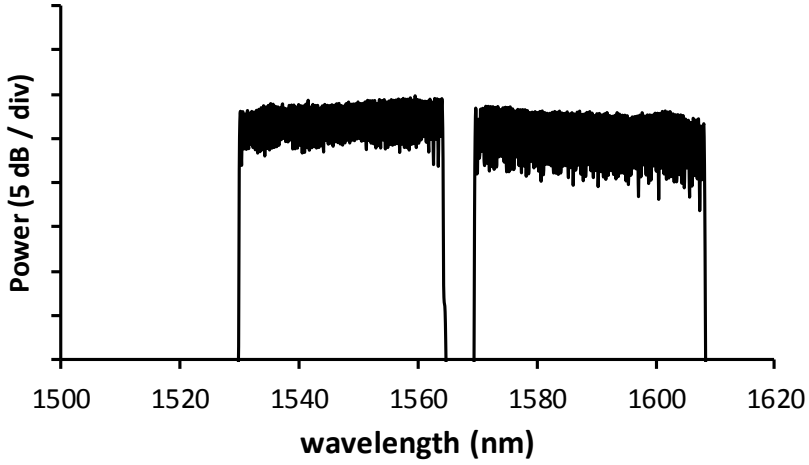

Fig. 1.4: Experimental spectrum of 178 channels multiplexing C and L bands with 50-GHz channel spacing.

To correctly allocate the different channels in the optical spectrum, several frequency grids have been defined [7]. In this work, we have selected the 50-GHz grid which was defined by the international telecommunication union (ITU), which is the most commonly used. The bandwidth of the system is fixed basically by the optical bandwidth of the amplifiers. Traditionally the C Band has been used, which ranges from 1530 nm to 1565 nm, with a total number of channels around 80-90 channels. This band could be extended to the L Band, from 1565 to 1610 nm. C+L signals can carry a total number of channels of not more than 180. For instance, in Fig. 1.4 we can see the optical spectrum for a C+L WDM transmission system with a total number of 178 channels.

1.3. *Modulation formats*

In digital communications, the different bits of information must be converted into symbols in temporal domain to be transmitted to the line. This is the goal of modulation formats. A modulation format is simply a mapping which defines how the different bits are coded into symbols in the temporal domain. The first modulation formats that appeared some decades ago only coded one

bit per symbol. New advanced modulation formats instead can code several bits into the same symbol increasing the spectral efficiency of the system. The main modulation formats used in this work are introduced below.

1.3.1 Amplitude modulation formats

a) On-off keying

The non-return-to-zero (NRZ) on-off keying (OOK) consists in coding a '0' bit with the lower optical-field power (ideally zero) in the whole symbol time and the higher input optical field power for the '1' bit. For several decades, this modulation format was the preferred one for commercial optical transmission systems. Nowadays, specifically in coherent systems, it has been mainly substituted by more advanced modulation formats. In Fig. 1.5-a) is shown the constellation mapping for this constellation.

1.3.2 Phase modulation formats

For the previous modulation format, the signal was only intensity modulated. Coherent detection permits to detect also the phase of the signal, so new modulation formats which modulate both amplitude and phase can be exploited.

a) PDM-QPSK constellation

In general, phase shift keying (PSK) is a family of modulations where only the phase of the signal is modulated, leaving the modulus constant for all the symbols. Several PSK modulations can be defined depending on the total number of symbols but the most known is quadrature phase shift keying (QPSK). QPSK defines a total of four symbols (each one contains two bits), which take the phases at π/4, 3π/4, -3π/4 and -π/4 radian. In Fig. 1.5-a) shows its constellation bit mapping. Inside this family there are other formats as binary phase shift keying (BPSK) where 2 bits are coded or 8PSK.

As discussed in a previous section we can use polarization division multiplexing to send two independent QPSK signals simultaneously. This type of modulation is named PDM-QPSK.

b) PDM-nQAM constellation

Another family of modulation formats is called n-ary quadrature amplitude modulations (n-QAM). Depending on the number of bits b which are modulated per symbol, we define n as $n=2^b$, where n is the total number of symbols. Constellations are defined in the complex plane where each axis codes the half part of the bits. This is the reason why b is usually an even number generating 4QAM (in fact is the same constellation than QPSK), 16QAM, 64QAM, 256QAM constellations. The symbols for each individual axis are equally spaced and the resulting mapping is something like a square. In Fig. 1.5-a) are shown the constellation mappings for some of these

constellations. For b equal to an odd number 8QAM, 32QAM… constellations can also be defined, but this is out of scope of this publication.

When we transmit a sequence of symbols, errors are usually produced between adjacent symbols. Considering this fact, we encode the different bits into the constellation symbols using Gray codes. These codes map the bits minimizing the difference between adjacent symbols to reduce the number of bit errors. In Fig. 1.5-b) we show the example for 16QAM, where the difference between two adjacent symbols is always one bit.

As in previous case we use the polarization diversity of the light to transmit two QAM signals simultaneously.

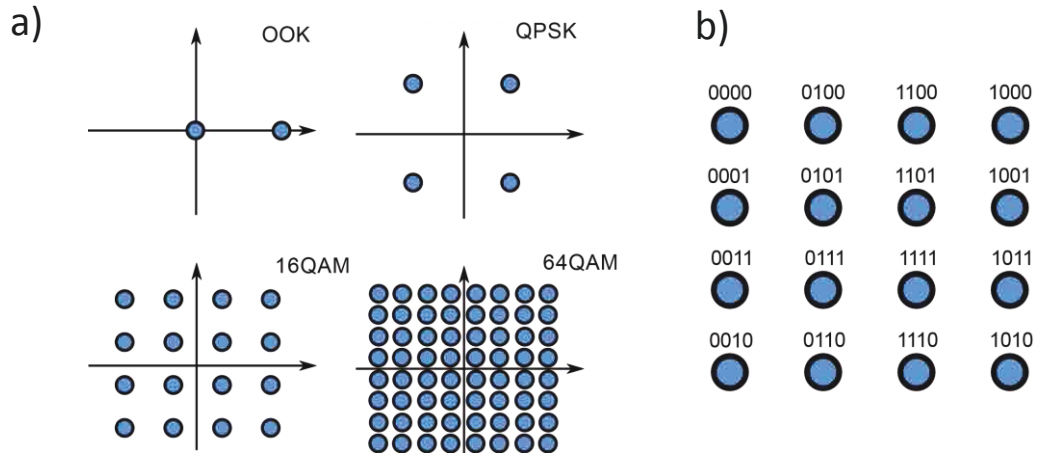

Fig. 1.5: a) Modulation formats considered in this work and b) example of Gray bit-to-bit symbol mapping for 16QAM

1.3.3 Pulse shaping

In a previous section, we have discussed about wavelength division multiplexing techniques, which consists in multiplexing several channels in the frequency domain and transmit them simultaneously. It is here where the spectrum of the transmitted signal must be characterized. In a WDM transmission system, the lower we can reduce the bandwidth of one channel, the more channels we will multiplex together. Or from another point of view, fixing the channel spacing (for instance at 50 GHz), the lower the channel bandwidth, the higher the channel symbol rate we can use.

Until now we have defined several modulation formats, but we have not talked yet about optical bandwidth. To do that first we must define mathematically how the transmitted signal looks like:

$$s(t) = \sum_{k} a_k \, p(t - k\,T_s) \tag{1.2}$$

where k is the indentation variable which ranges all the symbols. For each symbol, we define a_k as the complex value associated in the constellation

mapping to the symbol we want to transmit. T_s is the symbol duration. And p(t) is the pulse or basic waveform.

One of the simplest pulse responses that we can use is a rectangular one defined as:

$$rect(t) = \begin{cases} 1 & -\frac{T_s}{2} < |t| < \frac{T_s}{2} \\ 0 & otherwise \end{cases} \tag{1.3}$$

This pulse generates for instance the classic OOK if we take a_k as 1 when we want to transmit a one or 0 if we want to transmit a zero. The spectrum of the signal is related to the Fourier transform F of the pulse p(t). So, in case of using rect(t) as basic waveform the optical bandwidth will be the bandwidth of RECT(f) = F{rect(t)}.

$$RECT(f) = \frac{\sin(\pi\, T_s f)}{\pi\, T_s f} \overset{\text{def}}{=} \operatorname{sinc}(\pi\, T_s f) \tag{1.4}$$

This function basically has infinite bandwidth, so the construction of a WDM system would not be possible without cross-talk between channels. To solve this issue different pulses are used. The most important are explained below.

a) Sinc filter

Sinc filter provides a theoretical solution to reach the minimum bandwidth. If we use the sinc function in the temporal domain, the spectrum of the signal will be a rectangular pulse (due to the property of duality of the Fourier transform) with optical bandwidth equal to $1/T_s$. But, this solution has two major drawbacks. First one, the impulse response of the filter is not causal and second one it is infinite, making impossible its practical implementation.

b) Raised-cosine filter

Some practical approaches try to emulate the previous case but considering practical limitations. Raised-cosine filter is an example. In frequency domain, we define this filter as:

$$P(f) = \begin{cases} 1 & |f| \le \frac{1-\beta}{2\,T_s} \\ \frac{1}{2}\left[1 + cos\left(\frac{\pi\, T_s}{\beta}\left[|f| - \frac{1-\beta}{2\,T_s}\right]\right)\right] & \frac{1-\beta}{2\,T_s} < |f| \le \frac{1+\beta}{2\,T_s} \\ 0 & otherwise \end{cases} \tag{1.5}$$

Where β is defined as roll-off factor. In Fig. 1.6 we see the frequency response of some raised-cosine filters for different roll-off factors. We observe that playing with the parameter β, a trade-off between excess of bandwidth and the length of the impulse response can be obtained. This filter converges to the sinc filter when $\beta = 0$.

This filter can be applied half in the transmitter-side and half in the receiver-side so that the overall response corresponds to a matched Raised-cosine filter. If it is implemented like this however, the intersymbol interference between symbols can be reduced even more. This approach is known as the root-raised cosine (RRC).

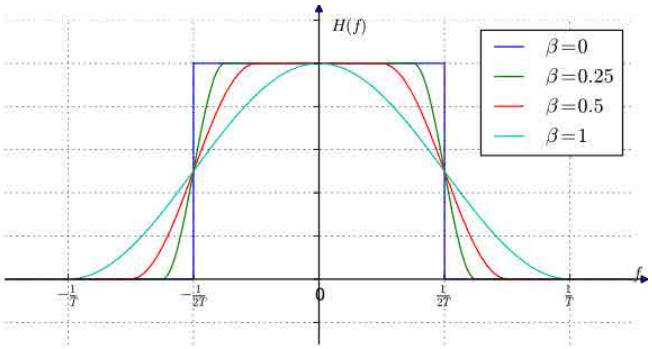

Fig. 1.6: Frequency response of raised-cosine filters with different roll-off factors (Image source: Wikimedia Commons)

1.4. *Information theory*

1.4.1 Introduction

In this section, we offer a more general overview of a telecommunication transmission system which is composed typically by a physical and a logical layer.

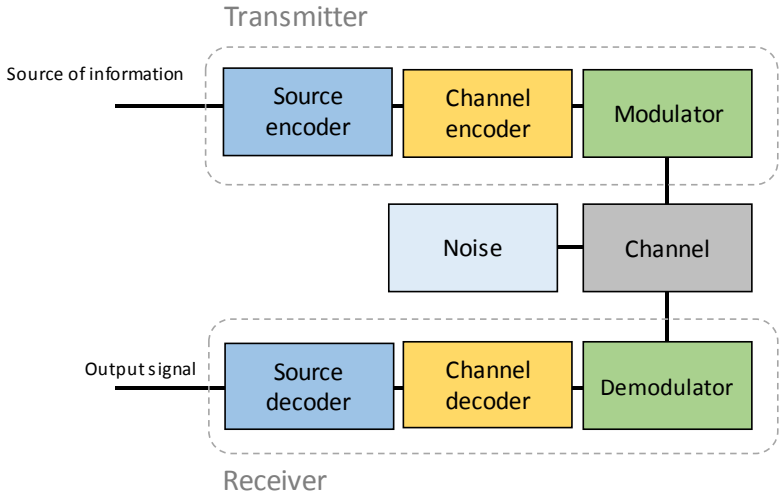

Fig. 1.7: General schematic of a telecommunication system from the information theory point of view

In Fig. 1.7, a general schematic of a telecommunication system is shown according to [8]. We observe that apart from the modulator, the channel and the demodulator other two pairs of blocks have been added. These blocks are in charge of treating the bits which later will be modulated and transmitted.

The first block is the source encoder. The goal of this block consists in reducing the total size of the digital sequence (or source of information) by removing all the unnecessary bits. Here information theory plays an important role because statistical properties of the data are considered to remove all the existent redundancy between bits.

Contrary to the source encoder, the channel encoder adds redundant bits to the sequence, but in a smart way which allows the detection or even correction of errors produced in the transmission of the signal through the channel. At the receiver, the complementary blocks decode the received signal.

In this section, general concepts of information theory are explained such as the concept of information, entropy or mutual information. Then, we define channel capacity, an important parameter that gives us the ultimate transmission limit. Finally, some details are given regarding the matter of channel coding.

1.4.2 Entropy

To study the statistical properties of a source of information, we usually define the concept of information entropy which was introduced by C. E. Shannon in 1948 [8]. As in other fields, entropy is a measure of the order, in this case of the information generated by a source. But first it is necessary to define what information is.

If we assume that a source of information can generate different symbols, each one can appear with probability p_i. The information (measured in bits) of an individual symbol as:

$$I = -\ log_2(p_i) \tag{1.6}$$

Information gives us the minimum number of bits necessary to transmit this symbol into the channel, based on its probability of occurrence. Averaging the information of all the possible symbols that can transmit the source scaled by their probabilities gives us the entropy of the source that can be defined as:

$$H = -\sum_i p_i\ log_2(p_i) \tag{1.7}$$

As a toy example, let's imagine that the source of information is tossing a coin and see the result. Every time that the coin is tossed we need to transmit the result into the channel. If the coin is not corrupted, we expect a probability of both head and tails equal to 50%. Applying this probability to the formula *(1.7)*, we obtain 1 bit of entropy. It has sense since we can code heads as '1' and tails as '0'. Only one bit is needed. Let's imagine that the coin is corrupted and the probabilities of heads and tails are 60% and 40% respectively. Then, the entropy of the source is 0.97 bits. We see that the entropy of the source is slightly smaller in this case. The fact of one symbol is more likely than the other adds redundancy that can be removed by encoding the source in an intelligent way. In other words, codes heads as '1' and tails as '0' is not the optimum

solution anymore. This example allows us to understand one of the main limitations of entropy and information theory in general. The entropy says that the minimum number of bits required to encode the information of the corrupted coin is 0.97, but it does not give us any mechanism to find this optimum code, it is just a lower boundary. The main conclusion of this example from the scope of this work is to notice that the entropy of a source reaches its maximum value when all the symbols are transmitted with equal probability.

1.4.3 Mutual information and channel capacity

Mutual information is a parameter used in information theory to measure the dependency between two random variables x and y. The mutual information can be seen as the amount of information shared by these two variables. If one of these variables is the transmitted signal and the other is the received one, the mutual information gives us the information that has successfully transferred from the transmitter to the receiver.

$$I(X,Y) = \sum_x \sum_y p(x,y)\, log_2\left(\frac{p(x,y)}{p(x)p(y)}\right) \tag{1.8}$$

$$I(X,Y) = \sum_x \sum_y p(x,y)\, log_2\left(\frac{p(y|x)}{p(y)}\right) \tag{1.9}$$

Where p(x) and p(y) are the probability distribution of the transmitted and the received signals, p(x,y) is the joint probability and p(y|x) is the probability of observing y when x is transmitted. *(1.9)* is obtained from *(1.8)* applying the Bayes theorem:

$$p(x,y) = p(y|x)\, p(x) \tag{1.10}$$

On the other hand, channel capacity is the maximum information throughput that we can transmit through a channel. We defined it as the maximum mutual information between the input and the output of a channel for any input density function.

$$C = \max_{p(x)} I(X,Y) \tag{1.11}$$

The channel considered is usually a white Gaussian complex channel where the receiver signal is corrupted by Gaussian noise with zero mean and variance $N_0/2$, N_0 being the noise power spectral density. Under these conditions, the conditional probability is a Gaussian function centred in the symbol x. This channel is named additive white Gaussian channel (AWGN).

When the noise added by the channel is high, there is no point to send a high number of bits per symbol because the noise will randomize them. So, channel capacity defines the maximum number of bits b we can send, in a reliable way, into every symbol. To derive the formula of channel capacity, let's consider a pulse amplitude modulation constellation of 2^b binary equispaced symbols.

The signal at the input of the optical modulator is confined to a defined range of voltages, where it works in the linear regime. Let's consider V_T as the total excursion voltage. In Fig. 1.8-a) is shown the mapping for every symbol. Notice that the voltage for each symbol is equal to $\pm\frac{\eta}{2}V_T/2^b$, where η takes odd numbers and the range ΔV confined for each symbol should be $V_T/2^b$. In Fig. 1.8-b) an example of a transmitted signal into the channel is shown.

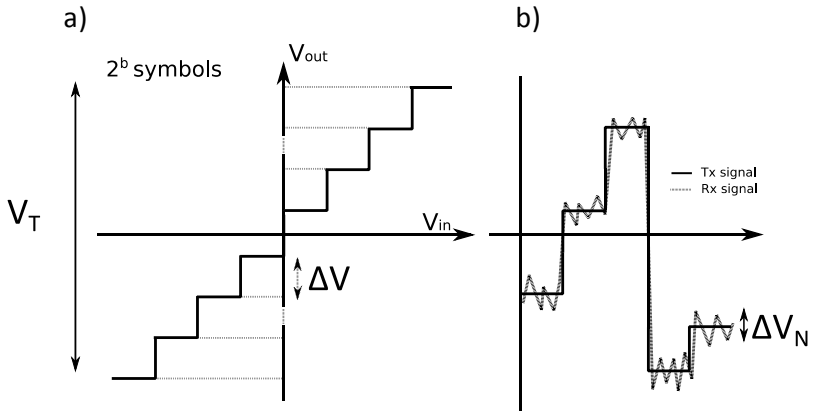

Fig. 1.8: Constellation mapping of the pulse amplitude modulation (a) and example of transmitted and received signals

After the transmission through an AWGN channel, the transmitted signal is polluted by the noise. Let's consider V_N as the noise voltage. In Fig. 1.8-b) an example of a received signal after a AWGN channel is shown.

The range ΔV establishes the maximum excursion of a symbol into the channel in order to be properly decoded in reception. Therefore, if we want to build a reliable system, there is no point in choosing a value for b which makes ΔV smaller than V_N. The noise will simply tend to randomize the actual voltage of the signal making meaningless any extra bits. Consequently, the maximum number of bits of information we can obtain is:

$$V_T/2^b \geq V_N \tag{1.12}$$

V_T is the sum of voltages of the signal and the noise, so we can obtain

$$2^b \leq \sqrt{\frac{(V_N + V_S)^2}{{V_N}^2}} \tag{1.13}$$

Where V_S is the power of the signal. Reordering the terms and neglecting the second order term:

$$2^b \leq \sqrt{1 + \frac{{V_S}^2}{{V_N}^2}} \tag{1.14}$$

$$b \leq log_2 \sqrt{1 + SNR} \tag{1.15}$$

The SNR is the signal to noise ratio defined as the ratio between the power of the signal and the noise. This is the maximum b we can define for a AWGN

channel at a given SNR. To derive the channel capacity from this equation now we consider that we do M, b-bit, measurements of the level in a time T the total number of bits of information is:

$$Mb \leq M log_2 \sqrt{1 + SNR} \tag{1.16}$$

This means that the information transmission rate I per unit time is

$$I \leq \left(\frac{M}{T}\right) log_2 \sqrt{1 + SNR} \tag{1.17}$$

From the Nyquist sampling theorem, we know that the highest practical sampling rate M/T is 2B, so:

$$I \leq 2B \, log_2 \sqrt{1 + SNR} \tag{1.18}$$

$$I \leq B \, log_2 (1 + SNR) \tag{1.19}$$

Thus, considering that channel capacity is the maximum reachable information transmission rate, the upper bound of this inequality leads the well-known Shannon formula which defines the channel capacity for a AWGN channel:

$$C = B \, log_2 (1 + SNR) \tag{1.20}$$

Fig. 1.9 shows in dashed line the maximum number of bits that can reliably be transmitted through an AWGN channel as a function of the signal to noise ratio.

As said before, channel capacity is considered as a fundamental limit for mutual information and sometimes is referred as the Shannon limit in recognition to its discoverer. Now, to see how close the different constellation formats are to this limit, their mutual information can be calculated by solving *(1.9)* for an AWGN channel.

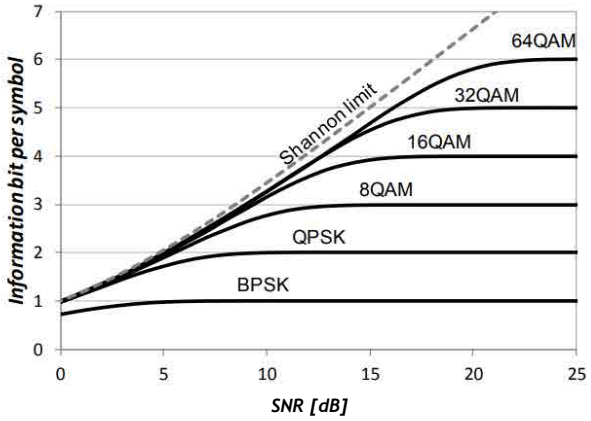

Fig. 1.9: Mutual information over a Gaussian channel for different modulation formats

We cannot solve this equation analytically, but we can use the Montecarlo method to solve the mutual information as a function of the signal-to-noise ratio. In Fig. 1.9, we show the mutual information over a Gaussian channel for different

modulation formats. Let's analyse the figure taking for instance 16QAM. For this modulation format, we can transmit 16 different symbols, thus the entropy of source that generates equiprobable 16QAM symbols is 4 bits. We observe that for high SNR, the mutual information of the input and the output is 4 bits. It means that we have successfully transmitted the 4 bits through the channel. If the SNR decreases, the mutual information is reduced gradually approaching to the channel capacity defined by the Shannon limit. The noise added in the channel corrupts the received signal, thus reducing the dependency between the input and the output. We can use the MI to quantify the useful information that can be recovered by the receiver for a given constellation format. For instance, for a 16QAM constellation, at 10 dB of SNR we can recover around 3 of every 4 bits launched into the channel.

The mutual information can also be calculated after performing a hard-decision, which consists in decoding each received symbol selecting the one from the alphabet that maximizes the probability density function of the observed symbol.

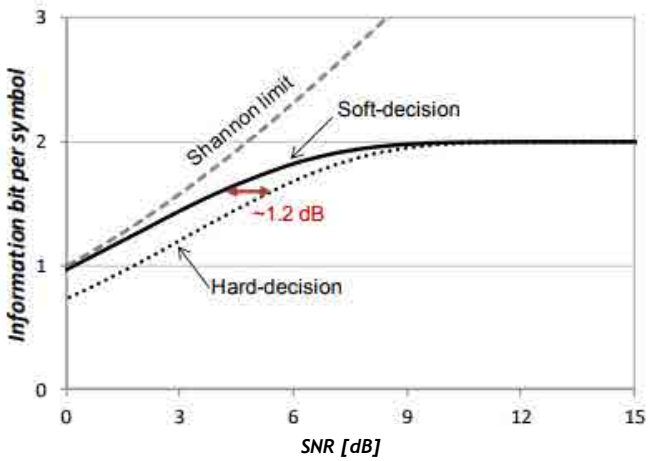

Fig. 1.10: Hard-decision vs Soft-decision for a QPSK constellation

We can intuitively deduce that hard-decision reduces the maximum achievable information rate because it does not take all the available information to decode the signal. In Fig. 1.10 the information bit per symbol is shown for a QPSK constellation performing a soft-decision and a hard-decision. It can be observed a penalty of about 1.2 dB in SNR at 1.6 bits per symbol.

Another approach is bit-wise decoding. This is an attractive alternative to reduce the decoder complexity in practical receivers. It consists in decoding every individual bit by itself and not taking the whole symbol information. We can calculate the bit-wise mutual information, which is interesting to quantify the achievable information rate of multi-level modulation decoded with bit-wise soft-decision. The bit-wise mutual information is sometimes referred as generalized mutual information (GMI). GMI is defined as:

$$GMI(X,Y) = \sum_i I(b_i, Y) \tag{1.21}$$

Where b is every individual bit. It can clearly be noticed that due to the fact of decoding every individual bit independently, and do not taking advantage of all the symbol information, this technique only may induce a degradation of the mutual information so:

$$GMI(X,Y) \leq I(X,Y) \tag{1.22}$$

In Fig. 1.11 is shown the mutual information and the GMI for a 8QAM signal as a function of the SNR. Note that GMI is slightly degraded for low SNR values. In summary, performing bit-wise soft-decision reduces the mutual information available at the decoder which results in lower achievable rate.

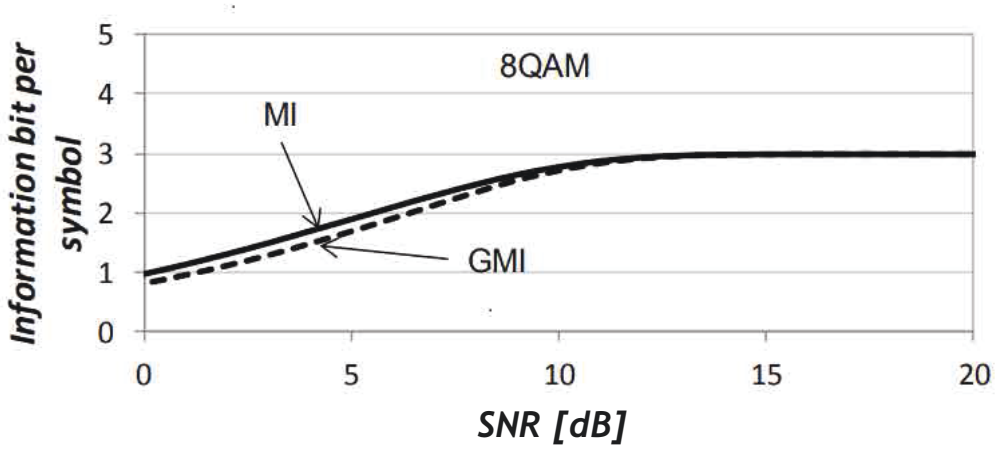

Fig. 1.11: Mutual information and GMI for an 8QAM modulation as a function of the SNR

1.4.4 Channel coding

The mutual information defines an upper bound of information rate for a given channel; however it does not tell us how to achieve this upper bound. This goal is obtained with channel coding. Channel coding consists on adding redundant information to the transmitted sequence with the aim of detecting and/or correcting errors (also called Forward error correction FEC) produced during the transmission through a noisy channel.

Let's consider that we have a sequence of k bits to be transmitted. We add r redundant bits, so the resulting block to be sent has a length of n = k + r.

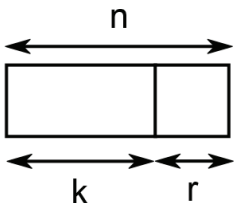

Fig. 1.12: Transmitted block with k bits of useful data and r bits of redundancy

The code rate R as

$$R = \frac{k}{n} \tag{1.23}$$

In the same way, we can also define the overhead OH:

$$OH = \frac{r}{k} = \frac{n-k}{k} = \frac{1}{R} - 1 \tag{1.24}$$

The American mathematician Richard Hamming was the first in working with block codes for correcting transmission errors [9]. In the following decades, some new codes such as Bose–Chaudhuri–Hocquenghem (BCH) [10][11] or Reed-Solomon [12] codes, which evolved from the initial ones discovered by Hamming, became popular. On the other hand, convolutional codes such as Turbo codes [13] have also been exploited in first decade of the XXI century. Their advantage is the fact that they can work with streams of arbitrary length but at expense of higher complexity.

In the last years, block codes have reappeared with Low-density parity check codes (LDPC). These codes were discovered by Robert Gallager in 1960 [14] with the aim of re-using block codes in a very efficient way. The fact that these codes can provide a performance very close to channel capacity [15] has popularized them and now they are used in the major part of all the recent high-speed communication standards [16]. In this work Spatially coupled LDPC codes have been used as a FEC technique which provide capacity approaching. Spatially coupled LDPC are LDPC codes with very long codewords done simply by connecting neighbouring blocks [17][18].

1.4.5 Probabilistically-shaped modulations

This concept has become popular in coherent optical communications for the last two years. Until now we have considered that all the symbols were transmitted with the same probability into the channel. This penalizes the GMI of our system because the quadrature modulation formats are suboptimal. Probabilistic shaping is a particular technique of constellation shaping which breaks with this idea by transmitting the symbols of the constellation in a non-equiprobable way. The concept exploited is the fact that in a Gaussian channel, the Gaussian distribution constellation is the one that maximize channel capacity [8]. So, varying the symbol probabilities of a traditional quadrature modulation format we can approach to a more Gaussian-like distribution which reduces the distance between the GMI and the fundamental capacity limit. Changing the symbol probabilities changes the entropy of the constellation. This is useful since we can tune this parameter to optimize the GMI for any given SNR.

In Fig. 1.13-a) we show an example of a probabilistically-shaped 64QAM (PS-64QAM) constellation. Notice in Fig. 1.13-b) that the probabilistic density of the in-phase symbols tends to approach to a Gaussian-like distribution.

In Fig. 1.13-c) we show the GMI for different modulation formats. If we focus in the two curves: PS-64QAM and for 64QAM as a function of SNR. We observe that PS-64QAM overcomes the performance of 64QAM and approaches rapidly to the Shannon limit for low SNR when the main impairment of the channel is the noise and the system behaves as a pure AWGN channel. Since the symbols are not sent with equal probabilities anymore, the entropy of the PS-64QAM is not 6 but a lower value. For the constellation shown in the figure the entropy is equal to 5.4 bits. Notice that at high SNR the GMI tends to converge to this value, while equiprobable 64QAM tends to converge to 6 bits. The conclusion is that PS-64QAM is not the optimum constellation in terms of GMI for all the SNR values. So we should have to adapt the entropy of the constellation to optimize the GMI of the PS-64QAM constellation for the region of operation we need to work. The benefit of shaped modulations was successfully assessed in [19].

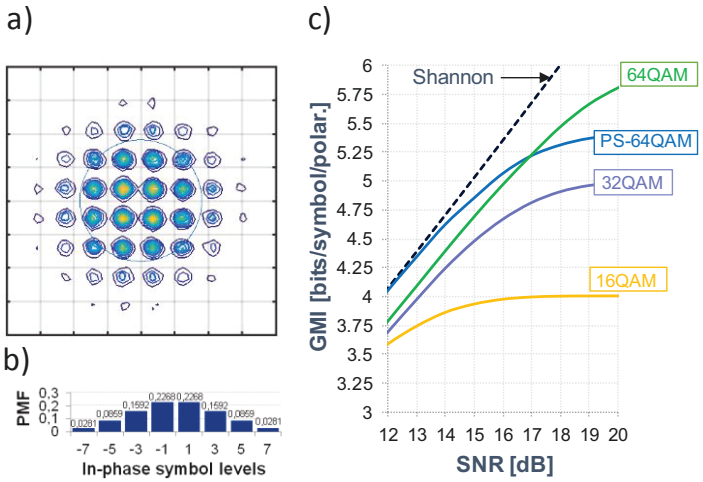

Fig. 1.13: Constellation format for a PS-64QAM (a), the probabilistic distribution for this modulation format of the in-phase levels (b) and GMI for different modulation formats as a function of SNR (c)

1.5. *Optical fibre*

The optical fibre is the physical medium to transfer information from one point to another by means of an optical signal. The use of optical fibres for telecommunication purposes at optical frequencies was proposed in 1966 [20]. Optical fibres are cylindrical dielectric waveguides commonly made of silica glass. Fig. 1.14-a) shows the different parts of an optical fibre which is formed by two different sections: the core and the cladding recovered by a coating. One possibility to confine the light within the core consists in doping the core with Germanium-Oxide. With this approach the refractive index of the core can be slightly increased and the light is confined thanks to the difference between its refractive index and that of the cladding [21].

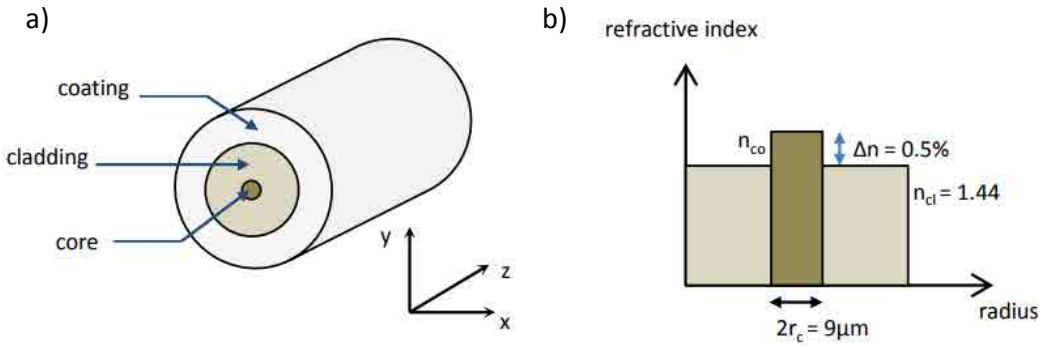

Fig. 1.14: Different parts of an optical fibre (a) and SSMF fibre dimensions (b)

As in all the waveguides, inside an optical fibre the signal propagates in discrete modes. To study the different propagation modes of an optical fibre, is more convenient to define a normalized frequency V [22] which depends on the fibre dimensions which permits to compare the different types of optical fibres:

$$V = \frac{2\pi r_c}{\lambda}\sqrt{n_{co}^2 - n_{cl}^2} \tag{1.25}$$

Where n_{co}^2 and n_{cl}^2 are the refractive indices of the core and the cladding respectively, λ is the wavelength and r_c is the radius of the core. The fundamental mode always propagates through the fibre. The second mode appears when the normalized frequency reaches 2.405 [23]. Thus, if V is lower than 2.405, only the fundamental mode is transmitted and the fibre is called single-mode. If higher, the fibre is called multi-mode.

In general, single-mode fibres are preferred, specifically for coherent optical transmission systems, because this type of fibre avoids detrimental pulse broadening effects produced by intermodal dispersion. In *(1.25)* we observe that the number of propagating modes depends basically of the core radius and in a minor degree in the refractive indices. The most commonly employed fibre for telecommunications has been standardized [24] and is called standard-single-mode fibre (SSMF). Dimensions of SSMF are shown in Fig. 1.14-b). Nevertheless, the core of SSMF is doped with GeO_2. Since this doping slightly increases fibre losses, better attenuation characteristics can be obtained by doping the cladding with fluoride [25]. An example of fibre which uses this type of doping is the pure-silica core fibre (PSCF). This fibre is particularly interesting for long-haul and submarine applications where the matter of reducing the losses is mandatory.

The use of multi-mode fibres is in general more challenging due to the cross-talk between modes and it was discarded when the technology allowed us to reduce the cost of single-mode fibres. However, the apparition of spatial division multiplexing (SDM) techniques has opened the door to the possibility of exploiting a fibre with a bounded number of modes, let's say 4-5 modes (in front of hundreds or even thousands of modes that these fibres used to have). This new type of fibre is called few-mode fibre and the idea is to transmit

different signals in each mode following a similar philosophy that the MIMO (Multiple input, Multiple output) channel in wireless domain. With similar objective multi-core fibres have also appeared, exploiting the possibility of adding more than one core inside the same cladding.

1.5.1 Linear effects

a) Attenuation

When an optical signal is propagated through an optical fibre its power is regularly attenuated due to absorption and scattering effects. If we consider the power in dBm and the attenuation in dB, we observe that the power is reduced linearly with distance. For practical reasons, we can define a parameter α which gives the attenuation in dB per km of a fibre.

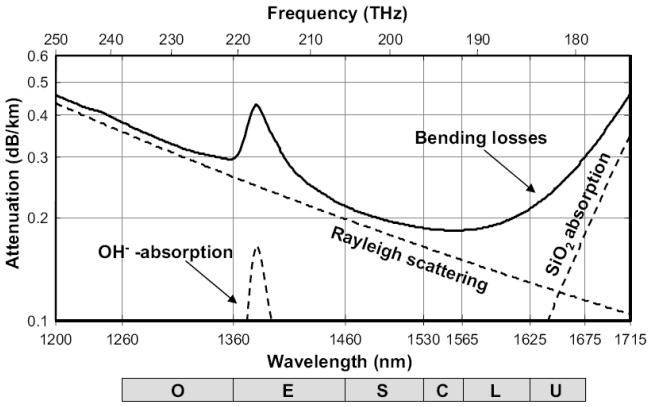

Fig. 1.15: Fibre attenuation dependence on the wavelength

In Fig. 1.15 we observe the evolution of α(dB/km) with wavelength for a SSMF. We observe two main effects which define the available optical bandwidth. For lower wavelengths, Rayleigh scattering effect becomes dominant whereas the SiO^2 absorption dominates at higher wavelengths.

Apart from these two mechanisms, a peak of attenuation is observed at 1.39 μm which corresponds to the absorption of the OH^- ions. Nevertheless, it can be nearly eliminated by reducing the concentration of hydroxyl (OH^-) ions in the core of the optical fibre [25][26][27].

Historically three different transmission windows have been exploited at 900 nm, 1300 nm and 1550 nm. More precisely, the telecommunication standardization sector of the international telecommunication union (ITU-T) defined six bands for transmission using single-mode fibre [28]: the O, E, S, C, L and U-band, as seen in Fig. 1.15. The band centred in C band (1550 nm) is the preferred one for long-haul transmissions because the losses of the fibre reach their minimum value: 0.2 dB/km in SSMF, 0.16 dB/km in PSCF or even less [29].

b) Chromatic dispersion

The speed of the light inside an optical fibre is not constant for all the wavelengths, so the different channels transmitted into the fibre propagates through the fibre at different velocities. This phenomenon causes the broadening of the transmitted pulses in time domain and generates intersymbol interference. We call this effect chromatic dispersion. As attenuation, chromatic dispersion increases linearly with distance and can be expressed with a parameter D in [ps/nm·km]. This parameter changes with the wavelength. In Fig. 1.16 the dependence of the fibre dispersion on this parameter is shown for SSMF. SSMF has a coefficient equal to 0 at 1320 nm and takes a value of 17 ps/(nm·km) at 1550 nm. Generally, this wavelength dependency is linear around 1550 nm so we can express a slope in [ns/nm^2 km], 0.057 ns/nm^2 km for SSMF.

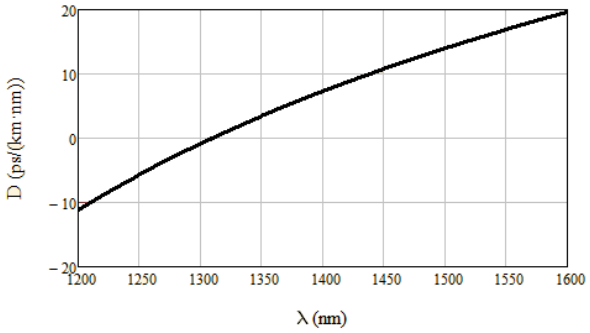

Fig. 1.16: Fibre dispersion dependence on the wavelength for SSMF

Before coherent systems appeared, chromatic dispersion was compensated by adding at the end of the span by using dispersion compensation fibres (DCF). This is a special type of fibre with negative chromatic dispersion parameter. In coherent systems however, the chromatic dispersion can easily be compensated with digital processing techniques at the receiver side and DCF are not needed anymore in the line.

1.5.2 Fibre nonlinearities

In previous sections we have discussed all the linear effects produced in the transmission along an optical fibre. In this section, we talk about the nonlinear distortions.

Kerr effect is the main cause of the nonlinear distortions experienced by the optical signal in WDM transmissions. Indeed, Kerr effect creates changes in the refractive index of the material in response to an electromagnetic field depending on its optical power $|E|^2$[30]:

$$\tilde{n}(\omega, |E|^2) = n_0(\omega) + n_2 \frac{|E|^2}{A_{eff}} \tag{1.26}$$

where A_{eff} is the effective core area of the fibre in [m^2] defined in [31], $n_0(\omega)$ is the linear contribution of the refractive index and n_2 is the nonlinear one

in [m^2/W]. The typical value of n_2 for silica is around $2.5 \cdot 10^{-20}$ m^2/W and is weakly dependent on the type of fibre.

The propagation of a signal along an optical fibre is described by the nonlinear Schrödinger equation (NLSE):

$$\frac{\partial E}{\partial z} = \underbrace{-\frac{\alpha}{2}E}_{\text{attenuation}} \underbrace{-\frac{j}{2}\beta_2\frac{\partial^2 E}{\partial T^2}}_{\text{dispersion}} + \underbrace{\frac{1}{6}\beta_3\frac{\partial^3 E}{\partial T^3}}_{\text{dispersion slope}} + \underbrace{j\gamma|E|^2E}_{\text{Kerr nonlinearities}} \tag{1.27}$$

Where E represents the envelope of the optical field, z is the distance, α is the attenuation coefficient, $T = t - \beta_1 z$ is the time measured in a retarded frame and γ is the nonlinear coefficient defined as:

$$\gamma = \frac{8}{9}\frac{2\pi}{\lambda}\frac{n_2}{A_{eff}} \tag{1.28}$$

The factor of 8/9 in the nonlinear coefficient has been verified experimentally [32][33]. It has to be noted that the factor of 8/9 becomes 1 in fibres with constant birefringence, such as PMF. The strength of the Kerr effect is proportional to the optical signal power $|E|^2$.

We observe that the first three terms of this equation refer to the linear effects of the optical fibre: attenuation and chromatic dispersion while the last term is the one related to Kerr effect. Kerr effect increases when the power is increased adding nonlinearities to the signal.

In Fig. 1.17, we present a table with a classification of the impairments that Kerr effect can generate. They are separated in two different parts corresponding to signal to signal interactions and signal to noise interactions. Among the signal to signal interactions we can find the intra-channel effects, which consist in the interactions of the channel with itself. The most important one is self-phase modulation (SPM). Then the inter-channel effects, where the interaction is produced between two or more channels: cross-phase modulation (XPM) and four-wave mixing (FWM) are the most important ones. Finally, there is the effect that takes into account the interactions between the signal and the noise known as nonlinear phase to noise (NLPN).

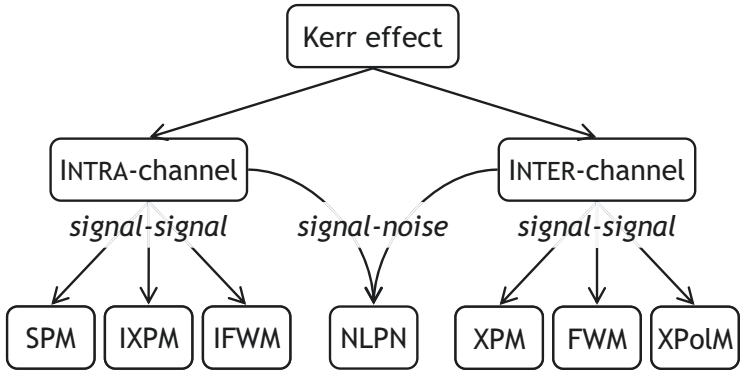

Fig. 1.17: Classification of nonlinearities in optical fibres

The baud-rate, type of fibre, length of the span, the use of uncompensated or compensated dispersion management determine which effect is predominant over the others. As the contribution of all these effects increases with fibre input power and they limit the maximum power of the system.

a) Self-phase modulation (SPM)

An electromagnetic field propagating through an optical fibre modifies the refractive index depending on its own instantaneous power. This variation is translated into a phase shift of the optical signal known as self-phase modulation.

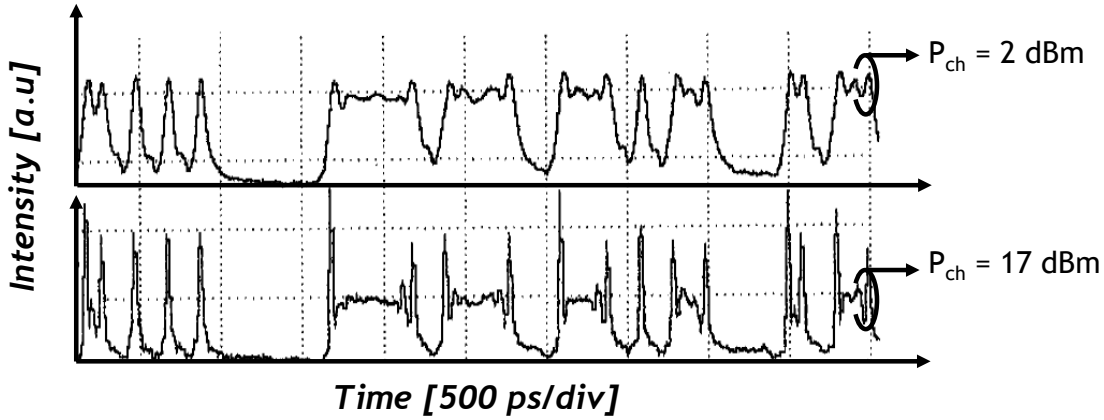

Fig. 1.18: Effect of phase-shift due to SPM and XPM for different channel powers

SPM translates into amplitude signal distortion through the interplay with chromatic dispersion. Nonlinearly-shifted frequency-components do not propagate at the same speed due to chromatic dispersion. When two pulse components with different frequency overlap, they interfere leading to nonlinear amplitude distortions, contrary to chromatic dispersion which induces a linear phase shift. The resulting effect is shown in Fig. 1.18 onto a 10 Gb/s NRZ signal after a propagation over 200 km of SSMF with the chromatic dispersion fully compensated. It can be clearly observed a deformation of the signal over the edges of the pulses for the highest power per channel.

b) Cross-phase modulation (XPM)

If SPM refers the phase shift experimented due to the instantaneous power variations of the own channel, the cross-phase modulation (XPM) is the same effect but produced by the other channels in a WDM transmission.

Consider the absence of chromatic dispersion. The effect of XPM is very close to SPM, with different strength, when the pulses of both wavelength channels overlap each other. In contrast, when the pulses at different wavelengths are only partially aligned the impact of the XPM is more detrimental since a part of the pulse is nonlinearly phase shifted while the other is not. The interplay between XPM and chromatic dispersion translates the

nonlinear phase shift into amplitude distortions. Besides, XPM scales with wavelength channel spacing and dispersion.

c) Four-wave mixing (FWM)

Four-wave mixing is the effect that takes into account the interactions between two or more frequency components. FWM, as in previous cases, is generated by the intensity-dependent refractive index of the silica.

From the point of view of quantum-mechanics, three photons at frequencies f_1, f_2 and f_3, can be annihilated with simultaneous creation of a single photon at frequency $f_4 = f_1 + f_2 – f_3$ generating a third harmonic. This condition is easier to satisfy when $f_1 = f_2$. According to this mechanism, two wavelength multiplexed channels at f_A and f_B will create FWM products at $f_C = 2f_A - f_B$ and $f_D = 2 f_B – f_A$. These new frequency components are shown in Fig. 1.19 and can generate cross-talk to other co-propagating channels.

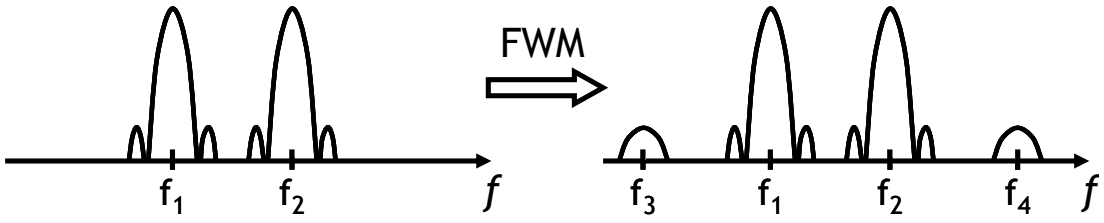

Fig. 1.19: The new frequency components generated through FWM

d) Non-elastic scattering effects

Besides the Kerr effect some other non-elastic scattering effects occurs in the fibre such as Stimulated Raman scattering (SRS) and stimulated Brillouin scattering (SBS). In this work, we only considered the SRS.

When a photon collides with a molecule of silica, it is normally scattered by Rayleigh scattering. The scattered photon then has the same energy as the incident one (elastic scattering) and no energy is therefore transferred to the silica molecule. However, a partial transfer of energy from the photon to the molecule occurs for a small fraction of collisions between photons and silica molecules (~10^{-6}). This is known as Raman scattering or Raman effect and is referred to as non-elastic since the energy of the scattered photon is lower than that of incident one. The silica molecule moves to a higher-energy vibrational state through the absorption of a fraction of energy of the incident photon whereas a lower frequency (higher wavelength) photon is generated. The scattered photon/wave is referred to as Stokes photon/wave. Stimulated emission through SRS only occurs when the power exceeds a threshold (SRS threshold). SRS threshold depends not only on the power of the optical field but also on the type of fibre [34]. Above this threshold, the amplification at longer wavelengths scales exponentially with the power of the shorter wavelengths. The maximum efficiency of SRS power transfer is found around 13.2 THz (~100 nm) away from the original frequency [35].

This effect is detrimental for WDM systems since it may result in unwanted energy transfer between the different channels. In this case, a fraction of the energy of the shorter wavelength (higher frequency) channels is transferred to the longer wavelength (lower frequency) channels. It results in a gain-tilt of the WDM spectrum, as depicted in Fig. 1.20.

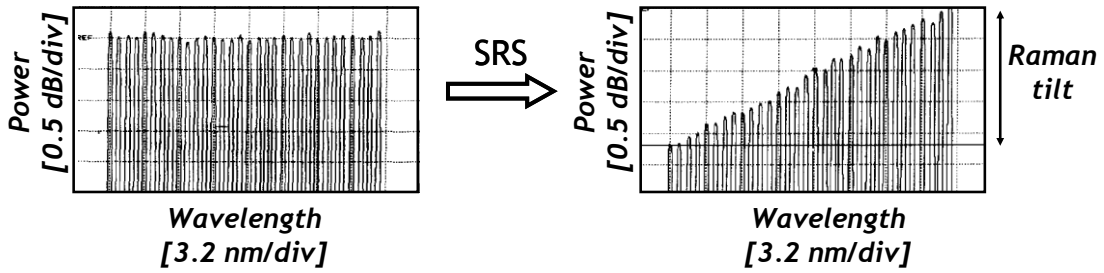

Fig. 1.20: Effect of stimulated Raman scattering onto a WDM multiplex.

1.6. *Optical amplification*

In section 1.5.1, we have talked about fibre losses. The optical receiver has normally a power sensitivity, which means that signal should arrive at the receiver higher than a certain power to ensure the successful demodulation of the transmitted data. Without something that compensates the fibre losses, the maximum transmission reach of an optical system should be confined to few tens of km and we would need to regenerate the signal for further distances. Here is where optical amplifiers have permitted to significantly increase the reach of the optical systems. Optical amplifiers take the weak signal at the output of the link and launch it into the system again at high output power. In this section, different types of optical amplifiers are described.

1.6.1 Erbium-doped fibre amplifier

Erbium-doped fibre amplifiers (EDFA) are without any doubt the most widely used amplifiers, they were introduced by E. Desurvire [36] et al and R. J. Mears [37] et al in 1987. The technique they use is basically doping a single-mode fibre with Erbium ions which is pumped by one or more pump lasers. Optical amplification takes place inside the Erbium-doped fibre which has a length around 10 m. The mechanism behind EDFA is stimulated emission introduced in [38]. The population inversion required for optical amplification is realised by pump laser at 980 nm or 1480 nm which correspond to Erbium absorption bands [39][40]. EDFA amplification provides an optical amplification window of 35-40 nm bandwidth in both C and L bands.

The huge advantage of this type of amplifier is the fact that the carrier lifetime is in the order of milliseconds [41], compared it to the typical symbol periods of the modulated signal (few hundreds of femtoseconds). The carrier lifetime is the time that the carriers need to recombine. So we observe that the EDFA is insensitive to envelope variations of incoming signals because they are so fast that do not permit the EDFA to react.

As any other type of amplifier, spontaneous emission of radiation is ineluctable. Apart from stimulated emission, spontaneously-emitted photons are launched to the output of the amplifier with arbitrary frequency and polarization. This effect is known as amplified spontaneous emission (ASE) and results into noise added to the signal. This effect is studied in more details in section 1.8.

1.6.2 Distributed backward pumped Raman amplification

Stimulated Raman scattering (SRS) can be used to achieve optical amplification as proposed by Stolen et al [42] in 1972 and demonstrated by Hegarty et al [43] in 1985. Contrary to EDFA which amplifies the signal in a lumped way, Raman amplifiers use the transmission fibre as the amplification medium corresponding to distributed amplification. In Fig. *1.21* is shown the power profile of the optical signal without Raman and with Raman. One can see how the signal has been gradually amplified.

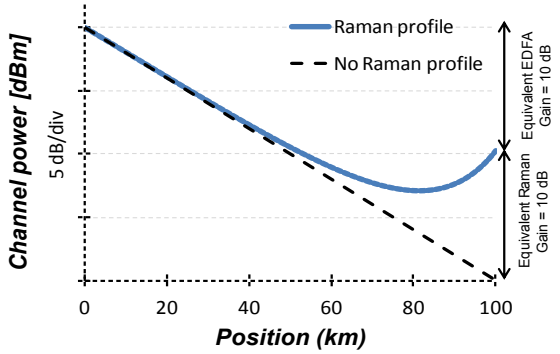

Fig. 1.21*: Power profile of an optical signal amplified by means of backward pumped Raman amplification.*

The 3-dB gain bandwidth of a single pump Raman amplifier is approximately 25 nm, but it can be extended using multiple pumps [35][44]. This is one good point of Raman amplification because 100 nm bandwidth can be achieved by using several pumps which range for instance from 1410 nm to 1510 nm. In Fig. *1.22*, we show a simulation of the Raman backwards pumping gain using 5 different pumps placed at 1410, 1435, 1460, 1485 and 1510 nm along 100 km of PSCF. In different colours is highlighted the contribution of each pump and in black the total gain of about 10 dB in a bandwidth higher than 100 nm. Currents of each pump can be equalized to compensate the higher losses of the fibre for shorter wavelengths.

Another good point of Raman amplification is the fact that as it can be observed in Fig. *1.21*, the minimum power along the link is higher for Raman amplification due to the distributed amplification than in lump amplification systems which translates in a better noise figure [44].

A weak point of distributed amplification is the fact that certain types of networks with reconfigurable optical add and drop multiplexers (ROAMs)

requires lumped amplification which can be done with a complex structure involving highly nonlinear fibres.

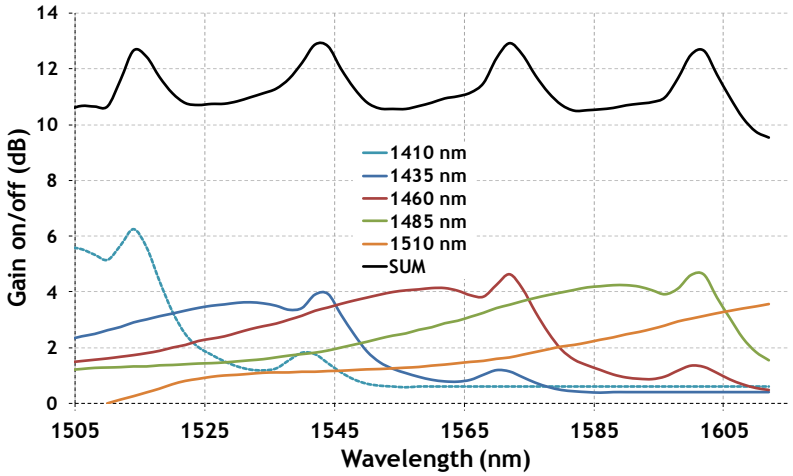

Fig. 1.22: Simulation of a Raman backwards pump along a 100 km of PSCF for 5 different pumps

1.6.3 Semiconductor optical amplifier

The semiconductor optical amplification principle is the same that the one used for designing a semiconductor laser [31]. The main difference is the fact that for the case of light amplification the signal travels in the forward direction only what is known as traveling-wave TW. To accomplish this objective, the facets of the Fabry-Perot cavity have been coated with an antireflection coating to reduce the reflectivity to an extremely low value, below 0.1%. An additional technique is also used to reduce the possible reflected waves that consist in tilting the active region from the facet normal. Such structure is referred to as the angled-facet or tilted-stripe structure. It is shown in Fig. *1.23*. In practice, the combination of both techniques produces reflectivities below 10^{-4}.

One of the main advantages of this type of amplification is the integrated optics which converts the SOA in a compact solution in front of other alternatives. However, the main drawback of this technology is the fact of having to manage the nonlinear distortions produced by the SOA since the carrier lifetime was much lower and comparable with the period of the transmitted signal (which makes the SOA sensitive to envelope variations). The envelope variations of incoming signals are converted into phase distortions. This impairment together with the incapability of having a high output power and the higher noise figure due to the additional coupling losses of the amplifier have historically delimited the use of SOA in different fields where its nonlinear nature can be exploited, but not optical amplification.

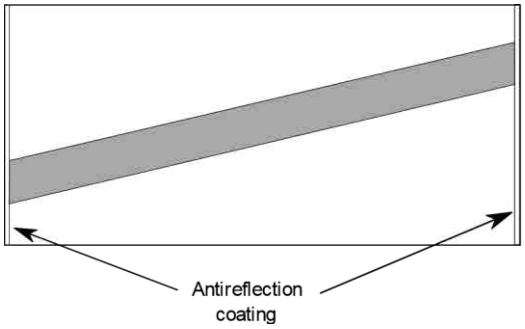

Fig. 1.23: Tilted-stripe structure for reduce the reflectivities in the cavity

1.7. *Coherent Optical Receiver and digital signal processing*

1.7.1 Coherent optical receiver

A coherent receiver can detect both in-phase and quadrature components of the two orthogonal polarization states by using four photodiodes and digital signal processing (DSP). Coherent detection was firstly investigated in the 80s [45]. Yet, the invention of EDFAs on one hand and the need for optical phase locking required to compensate the phase shift between the LO and the optical carrier on the other hand, made its implementation complex and unnecessary. Later, the interest in coherent detection was revived by the advancements in the increased performance, reliability and speed of dedicated integrated circuits that permitted to replace optical phase-lock loops with digital carrier recovery techniques and nowadays it is the most widely used alternative.

Signal coherent receiver [46] is depicted in Fig. 1.24. In a first step, received signal goes through a polarization beam splitter (PBS). The PBS divides the received signal into two, arbitrary at this moment, orthogonal components. Each component passes through a 90-degree hybrid and are mixed with a local oscillator (LO) laser. Depending if the laser used in the LO is the same laser, or not, that the one used to generate the signal, we can differentiate between homodyne (both lasers are the same) or heterodyne (an independent laser is used in LO) detection. As a general case and the most typical one here we use heterodyne detection. In this case, the LO frequency is set close to the same frequency of the laser used in transmission. As the lasers are not locked, the frequency and phase mismatch must be recovered with DSP.

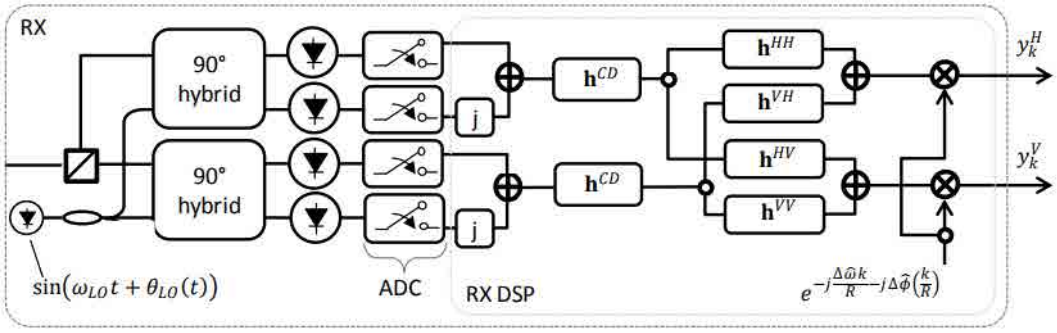

Fig. 1.24: Optical coherent receiver and digital signal processing scheme

At the output of the 90° hybrids we have the in-phase and quadrature components of two arbitrary polarizations which are detected by four balanced photodiodes and sampled into the digital domain with an analog-to-digital converter (ADC) at 2 samples per symbol (sps), which is the minimum sampling rate required to recover the transmitted signal according to the Nyquist-Shannon sampling theorem. For laboratory purposes, we usually use an oscilloscope which records the waveforms in the digital domain which will be post-processed using off-line algorithms. In this case a resampling is needed to down convert the waveforms to 2 sps if the oscilloscope sampling rate is not twice the symbol rate to emulate an ADC operating at 2 sps.

1.7.2 Digital signal processing

The different digital signal processing (DSP) techniques used to recover the transmitted sequence are the following ones. In a first step, we compensate the accumulated chromatic dispersion into the optical link. As seen in a previous section, chromatic dispersion is a linear impairment so it can be compensated by two polarization-independent linear filters which we represent with h^{CD}. The second step is to recover the original polarization states. We can do it with a butterfly equalizer (h^{HH}, h^{HV}, h^{VH}, h^{VV}). This equalizer can also find the optimal sampling instant. We use carrier frequency and phase estimation algorithms to correct the mismatches between the laser used in transmission and in the LO. Finally, with a post-equalization we compensate I/Q imbalances and the skew of the transmitter. The bits are decoded by the error correction code to correct the possible errors in the received signal and the bit error rate (BER) is finally extracted comparing the received signal with the transmitted one.

a) Chromatic dispersion compensation

As said in a previous section, chromatic dispersion used to be compensated for using a special type of fibre named dispersion compensation fibres with negative chromatic dispersion coefficient. However, the appearance of coherent systems allowed the possibility of compensating the cumulated dispersion directly at the end of the link using digital processing techniques. This alternative is cheaper to be implemented together with the fact that it outperforms the other one.

Chromatic dispersion after propagation can be modelled as:

$$G(\omega) = e^{-j\frac{DL\lambda^2}{4\pi c}\omega^2} \tag{1.29}$$

Where D is the dispersion coefficient, L is the transmission distance, λ is the wavelength and c is the speed of light. The filter used to compensate the dispersion can be written as:

$$h_k^{CD} = \sqrt{\frac{jcT^2}{D\lambda^2 L}\, e^{-j\frac{\pi cT^2}{DL\lambda^2}}} \tag{1.30}$$

The length of these filters is proportional to the amount of CD to be compensated for [47].

b) Adaptive equalization

A polarization rotation effect occurs when a signal is transmitted through an optical fibre, so at the receiver front-end we receive two orthogonal components, but at an arbitrary polarization state. The main aim of this block is to successfully recover the original in-phase and quadrature components. But in addition to polarization dependent impairments, this adaptive equalizer can also be used to approach the matched filter, find the optimal sampling rate, compensate residual chromatic dispersion and even mitigate possible low pass filtering impairments.

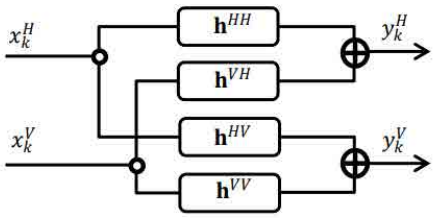

Fig. 1.25: Adaptive equalizer

The adaptive equalizer is implemented with a butterfly structure, shown in Fig. 1.25, which makes a linear estimation of the channel behaviour with the output signal being computed as:

$$\begin{bmatrix} y_k^H \\ y_k^V \end{bmatrix} = \begin{bmatrix} (h_k^{HH}) & (h_k^{VH}) \\ (h_k^{HV}) & (h_k^{VV}) \end{bmatrix} \begin{bmatrix} x_k^H \\ x_k^V \end{bmatrix} \tag{1.31}$$

The h^{HH}, h^{HV}, h^{VH} and h^{VV} components can be estimated using either data-aided or blind algorithms. The latter approach has the benefit of not increasing the sequence over-head so is often preferred. A common blind approach for constant amplitude signals such as PDM-QPSK is known as constant modulus algorithm (CMA) as proposed in [48]. This solution tries to estimate the filter components to force to the output constant amplitude on both polarization states by minimizing the following error function: $(\varepsilon_k)^2 = (1 - |y_k|^2)^2$ for both polarizations.

PDM-nQAM modulations are not constant amplitude signals, however this error function can be generalized by dividing the symbols in groups with constant amplitude. The resulting algorithm is known as the radius-directed equalizer proposed in [49].

The filter is implemented using a least mean squares (LMS) algorithm and the adaptive coefficients can be updated as:

$$\begin{aligned} h_{k+1}^{HH} &\rightarrow h_k^{HH} + \mu\, \varepsilon_k^H\, y_k^H\, x_k^{H^*} \\ h_{k+1}^{HV} &\rightarrow h_k^{HV} + \mu\, \varepsilon_k^V\, y_k^V\, x_k^{H^*} \\ h_{k+1}^{VH} &\rightarrow h_k^{VH} + \mu\, \varepsilon_k^H\, y_k^H\, x_k^{V^*} \\ h_{k+1}^{VV} &\rightarrow h_k^{VV} + \mu\, \varepsilon_k^V\, y_k^V\, x_k^{V^*} \end{aligned} \tag{1.32}$$

Where μ is the convergence parameter. As said before, the adaptive equalizer finds the optimal sampling rate and does the functions of the match filter so finally, we can already down-sample the signal to 1 sample per symbol.

This technique is interesting since it is tolerant to frequency detuning as phase noise distortions which do not affect the amplitude information. These impairments will be compensated in next stage.

c) Frequency and phase estimation

In heterodyne detection lasers used in the generation and in the local oscillator are different. Due to practical implementations, these two lasers have slightly different central frequencies and different instantaneous phases. However, it is assumed that these phase components vary slowly over time. Signal at the output can be modelled as:

$$y_k = x_k\, e^{j\omega k + j\phi} + n_k \tag{1.33}$$

y_k is the signal at the output and x_k the signal at the input. n_k is just the ASE Noise modelled as a complex white Gaussian noise. Finally, ω and ϕ are respectively the frequency offset and the phase mismatch that we must estimate. We split this problem in two different parts. First, we estimate the frequency and secondly the phase.

In the first part, we compensate the frequency offset. At this part, we assume that the phase mismatch is negligible in front to the frequency offset. We also assume that symbols x_k have constant amplitude. $\widehat{\omega}$ can be found by maximizing the following equation:

$$\widehat{\omega} = arg \max_{\omega} \left| \sum_{k=0}^{N-1} (y_k e^{-j\omega k})^n \right| \tag{1.34}$$

It can be intuitively interpreted as a frequency tuning, the same tuning we used to do with a FM receiver. In fact we test several frequencies until we keep the one that maximizes the signal. Another intuitive interpretation of this

equation is considering that $\sum_{k=0}^{N-1} y_k e^{-j\omega k}$ is the Fourier transform of the signal, so we set $\hat{\omega}$ as the highest frequency component. This approach is called periodogram.

Until now we have treated the case where x_k is always 1. This is not true since for instance QPSK takes four different values {1, -1, j, -j}. To deal with this problem we usually work with the 2nd or the 4th power of the signal [50]. With this approach remove the phase dependency of the transmitted data. This solution is called nth-periodogram.

Second part is phase estimation. Phase estimation is implemented with a blind phase search estimation that tries to minimize the following argument:

$$\hat{\phi} = arg \min_{\phi} \left| \sum_{n=-N}^{N} y_{k+n} - x_{k+n} e^{j\phi} \right|^2 \tag{1.35}$$

This sum of squared distances is minimized by the estimated phase

$$\hat{\phi} = arg \left(\sum_{n=-N}^{N} y_{k+n}{}^{*} x_{k+n} \right) \tag{1.36}$$

Where N is the length of the sliding window used to estimate the phase. For this block selecting a good length of N is important. In channels where the ASE noise is the dominant impairment is good to average the phase so choosing a N larger will improve the results. However, this is a suboptimal solution for nonlinear regimes.

The last step of the DSP is a LMS-DD post-equalizer composed of a T-spaced decision directed adaptive linear equalizer followed by a decision feedback equalizer (DFE) to mitigate the impact of residual symbol interference and other transmitter impairments (Fig. 1.26).

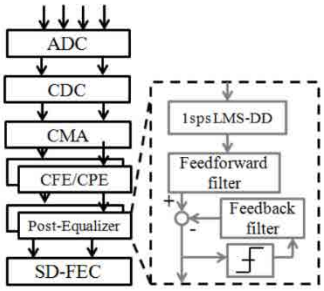

Fig. 1.26: Post-equalizer scheme

1.8. *Optical Signal-to-noise ratio*

Optical amplifiers add ASE noise which degrades the performance of the optical signal. A useful parameter to measure the impact of ASE noise is optical signal to noise ratio (OSNR) that consists in measuring the difference between the power of the signal and the power of the noise. We use an optical spectrum analyser (OSA) to measure the OSNR. The resolution or the optical filter used

will determine the power of the noise floor, so the OSNR is commonly expressed at a given resolution, usually 12.5 GHz (0.1 nm).

In Fig. 1.27 is shown the evolution of the signal power and the noise power in an amplified optical link with multiple spans of 100 km. We observe how the noise is increasing gradually in every pass of the signal through an optical amplifier. This degrades progressively the OSNR. Typical error correction codes can correct the errors in the sequence of data received if the OSNR of the received signal is above a certain value.

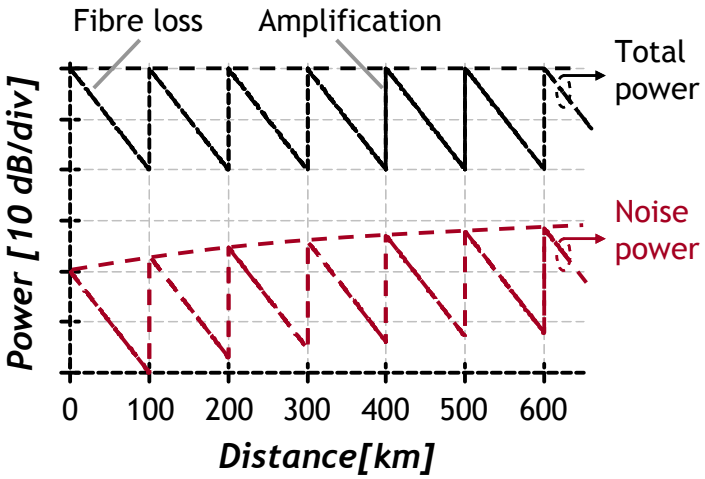

Fig. 1.27: Evolution of total power and noise power as a function of the distance for a system relying in discrete amplification.

Mathematically we can define the OSNR as [51][39].

$$OSNR = \frac{P_{signal}}{P_{ASE}} = \frac{P_{signal}}{2\,N_{ASE}\,B_{ref}} \tag{1.37}$$

Where P_{signal} is the signal power and P_{ASE} the noise power. We can also express the ASE noise in terms of noise power spectral density per polarisation mode, N_{ASE}, which is expressed in [*W/Hz*] and B_{ref} is the reference bandwidth of the filter, generally 12.5 GHz. The factor 2 results from the two orthogonal polarization modes of the optical field. The power spectral density is considered constant inside the reference bandwidth and is given by:

$$N_{ASE} = n_{sp}\,h\,f_o(G-1) \tag{1.38}$$

We can distinguish n_{sp} as the spontaneous emission factor, h as the Planck's constant ($6.626068 \cdot 10^{-34}$ J·s), f_o as the reference frequency in [*Hz*] and G as the gain of the amplifier.

1.8.1 Noise figure

To measure the impact of adding a given amplifier into a link, a parameter called noise figure is defined which allow us to compare the performance of different amplifiers.

We define noise figure in [dB] as:

$$NF = 10\log\,(F-1) \tag{1.39}$$

Where F is the noise factor. For one amplifier F is defined as [52]:

$$F = \frac{OSNR_{in}}{OSNR_{out}} \tag{1.40}$$

Where $OSNR_{in}$ and $OSNR_{out}$ are the OSNR at the input and at the output of the amplifier. Taking into account (1.37), (1.38) and (1.40):

$$F = \frac{P_{signal}^{in}\Big/ hf_oB_{ref}}{G\,P_{signal}^{in}\Big/ [hf_oB_{ref} + 2\,n_{sp}\;h\,f_o(G-1)\,]} = 1 + \frac{2\,n_{sp}\,(G-1)}{G} \tag{1.41}$$

Where P_{signal}^{in} is the signal power at the input. In the high gain region, this factor can be approximated by F – 1 ≈ 2 n_{sp}. This demonstrates that even an ideal amplifier, with $n_{sp} = 1$, has a noise figure of 3 dB.

The total noise factor of a chain of amplifiers with noise factor F_n and gain G_n can be contributed by means of the Friis formula:

$$F = F_1 + \frac{F_2-1}{G_1} + \frac{F_3-1}{G_1G_2} + \cdots + \frac{F_n-1}{G_1G_2G_3\ldots G_{n-1}} \tag{1.42}$$

Note that the values G_n are usually high so the noise figure of a chain of amplifiers tends to be determined basically by the first amplifier.

Assuming that all the spans have the same span loss and all the amplifiers are equal, the ASE Noise after transmission along N_{spans} spans is:

$$P'_{ASE} = N_{spans}\,P_{ASE} \tag{1.43}$$

So the OSNR after amplification can be expressed by:

$$OSNR = \frac{P_{signal}^{out}}{[G\,(F-1)-1]\,h\,f_oB_{ref}N_{spans}} = \frac{G\,P_{signal}^{in}}{G(\,F-1)\,h\,f_oB_{ref}N_{spans}} \tag{1.44}$$

Where P_{signal}^{out} is the power of the signal at the output of the amplifier. We have also approximated the term $[G\,(F-1)-1]$ to $G\,(F-1)$ since the product $G\,(F-1)$ is supposed to be much greater than 1. This formula can be expressed in dB:

$$\begin{aligned} OSNR &= 10\log_{10}\left(\frac{G\,P_{signal}^{in}}{G(\,F-1)h\,f_oB_{ref}N_{spans}}\right) = \\ &= 10\log_{10}\left(h\,f_oB_{ref}\right) - P_{signal}^{in} - NF - 10\log_{10}(N_{spans}) \end{aligned} \tag{1.45}$$

Sometimes for simplicity the term $10\log_{10}\left(h\,f_oB_{ref}\right)$ is substituted by 58 dBm, that is obtained when using B_{ref} of 12.5 GHz and $\lambda_o \approx 1550\,nm$. In any

case we observe how the OSNR decreases logarithmically along the link with the number of spans.

$$OSNR = 58\ dBm - \ P_{signal}^{in} - NF - 10\log_{10}(N_{spans}) \tag{1.46}$$

We can use the previous formula to measure the noise figure of an amplifier. First we add linearly the OSNR of the input signal and the one added by the amplifier. The output OSNR can be obtained as follows:

$$10^{OSNR_{out}/10} = \ 10^{OSNR_{in}/10} + \ 10^{OSNR_{ampli}/10} \tag{1.47}$$

From the measurement of the OSNR of the signal at the input and at the output of the amplifier, we can obtain the NF as:

$$\begin{aligned} NF = 10\log_{10}(h\ f_o B_{ref}) - \ P_{signal}^{in} + \\ + 10\ log_{10}(10^{OSNR_{in}/10} - \ 10^{OSNR_{out}/10}) \end{aligned} \tag{1.48}$$

If we consider that the $OSNR_{in}$ is high enough, B_{ref}= 12.5 GHz and $\lambda_o \approx 1550\ nm$ we can simplify the formula to the following expression:

$$NF = 58\ dBm - \ P_{signal}^{in} - \ OSNR_{out} \tag{1.49}$$

1.9. ***Trade-off between OSNR and fibre nonlinearities***

If we only consider the OSNR of the link and according to *(1.45)*, it seems that the higher the input power is, the better the OSNR becomes and therefore the quality of the signal. But it is not exactly true since at higher power the nonlinear effects of the fibre increase and become the main impairment of the system. It is the reason why we have to find a trade-off between OSNR and fibre nonlinearities.

In Fig. 1.28 we can observe the Q² factor as a function of the power per channel. We observe that for low input powers we are limited by ASE noise so the Q² factor increases linearly with the power, and therefore the OSNR. When power increases beyond, the fibre finally adds nonlinear distortions that degrade the performance, so the Q² factor reduces despite the fact the OSNR is increasing. We call this region as NL limited.

We define the nonlinear threshold (NLT) as the input power where the performance reaches the maximum. NLT is the optimum power to be placed at the input of the span. NLT depends on the link configuration such as type of fibre, length of the span, dispersion per span... NLT can also be increased by using nonlinear compensation techniques such as digital-back propagation (DBP) which reduces the fibre nonlinearities.

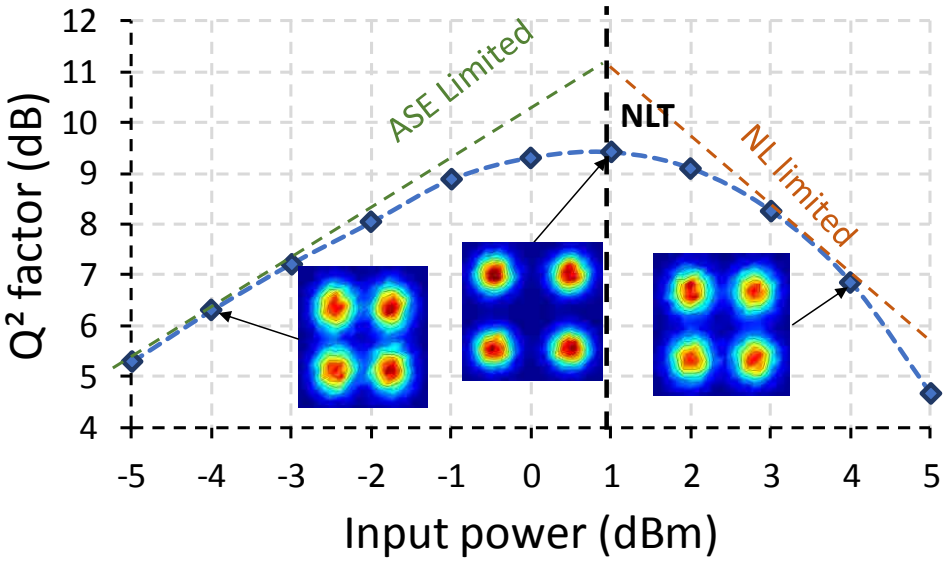

Fig. 1.28: (a) Evolution of performance as function of power per channel

Fibre nonlinearities accumulate periodically along the pass through the different spans of the transmission system, defining a Nonlinear Shannon limit that bounds the spectral efficiency at any transmission distance.

Chapter 2. Semiconductor optical amplifier: Modelling for Coherent systems

2.1. *Introduction*

In system design, we are interested in developing a numerical or analytical tool which permits to estimate in a fast way the quality of the received signal in terms of OSNR, nonlinearities… A good approximation of these parameters allows us to calculate the potential of an optical link without the necessity of deploying the whole system. Furthermore, it also offers the possibility of optimizing it in a more efficient way. This not only reduces the time, but also the costs, because there is even no need of investing on the required physical components.

As a reminder, in Fig. 2.1 an optical transmission link is depicted. It consists of several spans of optical fibre followed by optical amplifiers. The purpose of optical amplifiers is to recover the initial optical power after the losses along the span. Traditional systems use Erbium-Doped Fibre Amplifiers (EDFA) amplifiers. The high carrier lifetime of this type of amplifier, in the order of milliseconds, makes this technology completely robust in terms of nonlinearities. As EDFA generate very few nonlinearities, the main complexity in simulations used to be focus on the propagation of the light along the optical fibre. This issue was already solved by using the Split-step Fourier method (SSFM), which computes the nonlinear Schrödinger equation introduced in *(1.27)* with numerical methods. In fact, the only impairment added by EDFA

amplifiers usually considered by numerical simulations, is ASE noise that progressively corrupts the optical signal-to-noise ratio OSNR.

The use of SOA to amplify the optical signals in a transmission system changes completely the current paradigm, because carrier lifetime is usually in the order of hundreds of picoseconds. It means that the simulation of an optical system has to take into account also the nonlinearities of the optical amplifier since the SOA is sensible to envelope variations. This issue is translated into the addition of some lumped nonlinearities to the optical signal which corrupt the signal.

In the past, several models have been published in the literature with the aim of modelling a semiconductor optical amplifier [56, 57]. The most recognized is the model introduced by Connelly [58], which is capable of precisely modelling the behaviour of the SOA in nonlinear regime, but requiring high computational times even to simulate a single step function. This fact makes it impractical for simulating the performance of an optical transmission system due to both, its high computational complexity and the huge quantity of parameters to be handled.

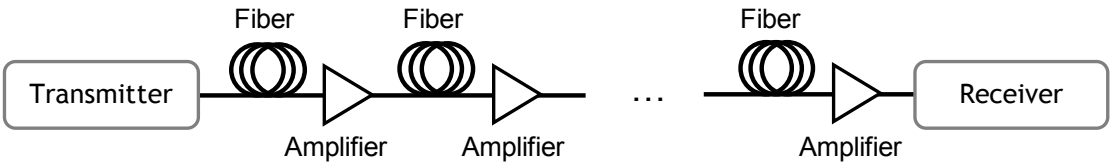

Fig. 2.1: Optical transmission system

Things become even more challenging if we consider a fully loaded WDM system. In WDM system analysis, the compromise between precision and complexity is overriding, and the need of finding a model to simulate the performance of a WDM optical transmission in a reasonable computing time, is mandatory. It is the reason why in this work the reservoir model has been chosen. It is not by far the most accurate model, but it simulates the dynamics of an SOA in a powerful way. This model is introduced in this chapter and then, some characterization is done with a state-of-the-art SOA with the aim of extracting its main parameters. Finally, some experiments are done using different types of modulation formats which are compared with the results of the numerical simulations to assess the performance of the model.

2.2. *Semiconductor optical amplifier*

Semiconductor optical amplifiers are made from group III-V compound semiconductor crystals such as GaAs/AlGaAs, InP/InGaAs, InP/InGaAsP and InP/InAlGaAs[31] [59][60].

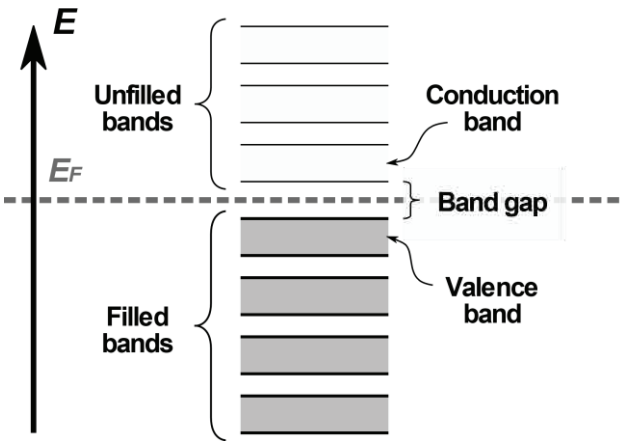

Fig. 2.2: Energy bands of a semiconductor (Figure source: Wikimedia Commons)

The optical properties of a SOA can be analysed by studying the energy bands of semiconductors [61]. By nature, carriers tend to move to the less energetic states so, as it is shown in Fig. 2.2, in thermal equilibrium we can differentiate two different types of bands: the bands where the carriers tend to be placed, which are called filled bands, and the ones that tend to be empty, the unfilled bands. These two types of bands are delimited by the Fermi level. Fermi level is defined as the energy required to add another carrier to the semiconductor. We define the valence band (VB) and conduction band (CB) as the bands closest to the Fermi level. For simplicity, we only study the effects that happen between these two bands. Let's consider that the carriers are called electrons in the CB and holes in the VB.

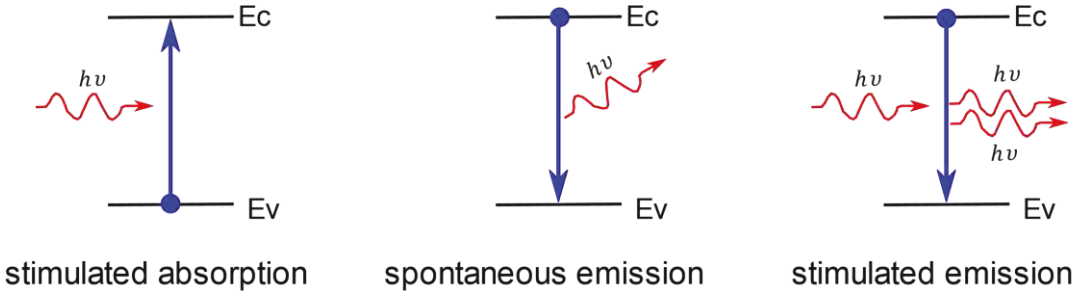

Fig. 2.3: Light interaction with carriers can be explained with three different processes

Light photons interact with carriers through different processes. The most important ones are stimulated absorption, spontaneous emission and stimulated emission. In Fig. 2.3, these three processes are shown. An incident photon can interact with a hole in the VB and, if the energy of the photon is sufficient, the hole can absorb this energy and go up to the CB. This process is called stimulated absorption. As said before, carriers tend to move to lower energy bands. An electron after certain time in the CB can spontaneously descend to the VB. This electron generates a photon with arbitrary frequency and phase. This process is called spontaneous emission. Finally, an incident photon can interact with an electron in CB moving it to VB. The result of this

iteration is a new photon with same properties than the original one. This process is called stimulated emission.

For light amplification purposes, we are only interested in stimulated emission of radiation. This operation can be cascaded during the pass of the photons along the cavity generating more and more photons, thus amplifying the input signal. On the other hand, spontaneous emission of radiation generates photons with random frequency and phase which induce the well-known ASE noise that contaminates the optical signal.

In thermal equilibrium, the distribution of carriers is not the most favourable for stimulated emission of radiation. In this state, holes in the VB dominate in front of the electrons in the CB and spontaneous emission dominates in front of stimulated emission. We can solve this issue by increasing the density of electrons in the CB, what is called the population inversion (when the density of carriers is greater in the upper level), by electrically pumping the semiconductor. With population inversion, the stimulated emission dominates and there is gain in the cavity.

To model this gain, we may consider that gain increases linearly with N, the number of electrons in the CB, as expressed in *(2.1)*. We call N_0 the transparency value, defined as the minimum value of electrons needed in the CB to guarantee the population and σ_g, the differential gain.

$$g(N) = \sigma_g(N - N_0) \tag{2.1}$$

We can express mathematically the different formulae which govern the basic dynamics of the SOA:

$$\frac{dP_h}{dt} = gP_h + R_{sp} - \frac{P_h}{\tau_p} \tag{2.2}$$

$$\frac{dN}{dt} = \frac{I}{q} - \frac{N}{\tau_c} - gP_h \tag{2.3}$$

We call P_h the number of photons inside the cavity, R_{sp} refers to the spontaneous emission term, I is the bias current to force the inversion of population, q is the charge of an electron equal to 1.602 10^{-19} C . Finally, τ_p and τ_c refers to what is called photon and carrier lifetime. We define them as the mean time that a photon or an electron, respectively, needs to recombine. These two equations are highly related between them and represent the evolution of photons and electrons inside the cavity. We can interpret them in an intuitive way. We observe that the term gP_h is present in both equations, it represents the stimulated emission of radiation. When stimulated emission of radiation occurs, it generates new photons from the electrons in the CB which moves to the VB. The spontaneous emission represented by R_{sp} generates new photons. The two terms that contains them in the equations represent respectively the loss of photons due to the absorption of the cavity, and the loss of carriers due to either spontaneous emission or non-radiative recombination.

Finally, the term I/q refers to the electric pumping of electrons where I is the bias current and q is the charge of an electron. Notice that all the effects commented in Fig. 2.3 have been taken into account in the definition of these equations. These equations are the same as the ones used to model a semiconductor laser. In fact, a SOA can be seen as a laser but without reflectivity in the facets of the cavities.

2.3. *Agrawal's model*

Let $\vec{r} = (x, y, z)$ refer to the spatial coordinates of the SOA, where z is the coordinate along the SOA waveguide longitudinal axis, x and y are the coordinates in the transversal plane. The optical field inside the SOA waveguide is written as:

$$\vec{E}(\vec{r}, t) = \hat{e} f(x, y) \sum_{i=1}^{N_{ch}} A_i(z, t)\, e^{-j(\omega_i t - \beta z)} \tag{2.4}$$

Let's consider a transmission of N_{ch} channels where i is the index of each channel. Where $\hat{e}$ is the unit polarization vector, t is the time, $f(x, y)$ is the fundamental mode transversal field profile of the SOA waveguide, A(z, t) is the varying envelope of the optical field, ω_i is the angular frequency at the center of each channel, and β is the propagation constant.

Let's consider that the energy of each photon is $E = h\,\vartheta$, where h is the Plank constant and ϑ the frequency. So, substituting this value and *(2.1)* in *(2.3)*, and considering the transversal spatial coordinate and temporal dependency, and arranging the terms we obtain:

$$\frac{dg(z,t)}{dt} = \frac{\sigma_g \left(\frac{I\,\tau_c}{q} - N_0\right) - g(z,t)}{\tau_c} - \frac{\sigma_g\, g(z,t)}{h\vartheta}\, p(z,t) \tag{2.5}$$

Where p is the input power of the signal. In steady state, that means when the carrier and photons populations stabilize. We can equal this equation to zero and obtain the static gain which can be expressed as:

$$g(z) = \frac{g_o}{1 + \frac{p(z)}{P_s}} \tag{2.6}$$

We define these new terms as the small-signal gain g_o and the saturation power P_s:

$$g_0 = \sigma_g \left(\frac{I\,\tau_c}{q} - N_0\right) \tag{2.7}$$

$$P_s = \frac{h\vartheta}{\sigma_g \tau_c} \tag{2.8}$$

Once these parameters are defined, we can simplify *(2.5)* by substituting *(2.7)* and *(2.8)*:

$$\frac{dg(z,t)}{dt} = \frac{g_0 - g(z,t)}{\tau_c} - \frac{g(z,t)}{\tau_c P_s} p(z,t) \tag{2.9}$$

Coming back to the WDM system defined in *(2.4)*, we consider that the envelope $A_i(z,t)$ varies slow enough to see significant differences of signal along the transversal axis of the SOA, so for every channel we have the following equation:

$$\frac{dg_i(z,t)}{dt} = \frac{g_{0_i} - g_i(z,t)}{\tau_{c_i}} - \frac{g_i(z,t)}{\tau_{c_i} P_{s_i}} \sum_{i=1}^{N_{ch}} |A_i(z,t)|^2 \tag{2.10}$$

What it is important to note here is the impact of the power of the rest of the channels to the channel under test i.

In studying traveling-wave amplifiers we examine the slowly varying envelope in the moving frame. The propagation equation for each channel is given by [62][63]:

$$\frac{dA_i(z,t)}{dz} = \frac{1}{2} g_i(z,t)(1 - j\alpha)A_i(z,t) - \frac{1}{2} \gamma_i(z,t)A_i(z,t) + \varepsilon(z,t) \tag{2.11}$$

Where α is known as the Henry factor or linewidth enhancement factor, $\gamma_i(z,t)$ is the loss coefficient that includes both carrier-independent and carrier-dependent SOA losses. Finally, $\varepsilon(z,t)$ is the amplified spontaneous emission modeled as a complex Gaussian random process. We can neglect the impact of the ASE noise term and the distribution loss so the propagation equation is simplified to:

$$\frac{dA_i(z,t)}{dz} = \frac{1}{2} g_i(z,t)(1 - j\alpha)A_i(z,t) \tag{2.12}$$

2.4. *Reservoir model*

We also define the integrated reservoir gain from the input to any position along the longitudinal axis of SOA as [63]:

$$h_i(z,t) = \int_0^z g_i(z',t)dz' \tag{2.13}$$

We define L as the length of the SOA in the longitudinal axis. To simplify notation, we consider that:

$$h_i(t) = h_i(z,t)|_{z=L} \tag{2.14}$$

The input and output fields and powers are defined as:

$$A_{in}(t) = A(z,t)|_{z=0},\ A_{out}(t) = A(z,t)|_{z=L} \tag{2.15}$$

$$p_{in}(t) = p(z,t)|_{z=0},\ p_{out}(t) = p(z,t)|_{z=L} \tag{2.16}$$

At any position, fields and powers at the input and output of the SOA can be written as:

$$p_{out}(t) = \sum_{i=1}^{N_{ch}} p_{in_i}(t) e^{h_i(t)} \tag{2.17}$$

$$A_{out}(t) = \sum_{i=1}^{N_{ch}} A_{in_i}(t) e^{\frac{1}{2}(1-j\alpha)\, h_i(t)} \tag{2.18}$$

Finally, we obtain for each channel:

$$\frac{dh_i(t)}{dt} = \frac{g_{0_i} L - h_i(t)}{\tau_{c_i}} - \left[e^{h_i(t)} - 1\right] \frac{p_{in}(t)}{\tau_{c_i} P_{s_i}} \tag{2.19}$$

We define h_{0_i} as $g_{0_i} L$ and $\bar{p}$ as the power normalized to P_s:

$$\tau_{c_i} \frac{dh_i(t)}{dt} = h_{0_i} - h_i(t) + \left[e^{-h_i(t)} - 1\right] \bar{p}_{out}(t) \tag{2.20}$$

Thus, we reach to the differential equation that models the dynamics of the SOA according to the reservoir model. We can contribute the value of this differential equation by numerical methods.

2.4.1 Static gain and saturation power

The static gain of the amplifier can be modeled from *(2.6)*. We must integrate $g(z)$ through all the SOA to obtain G, the total gain as:

$$G = g_0\, e^{-\frac{G-1}{G}\frac{P_{out}}{P_S}} \tag{2.21}$$

The resulting equation depicted in *(2.21)* cannot be solved analytically but with numerical methods. The extraction of the parameters g_o and P_s, which are dependent of the wavelength, is done by measuring experimentally the gain for different wavelengths as a function of the input power.

In Fig. 2.4 we observe a generic curve of the gain of a SOA as a function of the input power. With the help of *(2.21)* , we can easily identify that for low input powers the exponential term is negligible so the total gain G is equal to g_0 . It is referred as the linear gain of the SOA or also called small signal gain. Then the gain saturates gradually when increasing the input power on the SOA. The regime where the gain of the SOA is close to the small signal gain is called linear regime. When the SOA operates in linear regime no nonlinear effects are expected since in *(2.20)* the exponential term is negligible for low powers. On the other hand, the region where the gain is reduced is called saturated or nonlinear regime. The power that delimits the two regimes is usually called

saturation power. Notice that in practice there is no a clear limit defined limit between the two regimes because in fact the saturation occurs progressively. By convention it is common to define the saturation power P_{sat}^{-3dB} as the output power where the gain is reduced by 3 dB. It is because this saturation power can be derived easily from the gain curve.

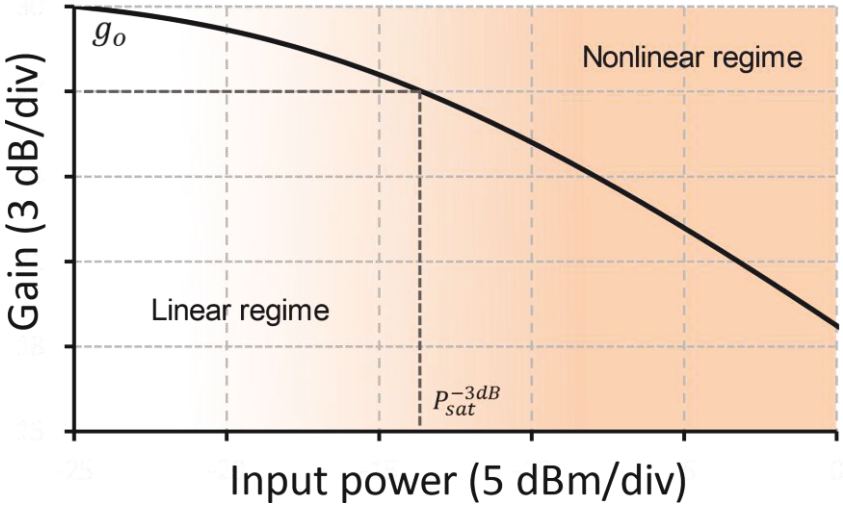

Fig. 2.4: Gain measured as a function of the Input power

It is important not to get confused between P_{sat}^{-3dB} and P_s, both parameters refer to the same concept, the saturation of the SOA, but from a different point of view. However, we can easily find a relation between them by substituting P_{sat}^{-3dB} in *(2.21)* and knowing that, by definition, the gain at this point is $g_0/2$. We obtain:

$$P_s = \frac{2(g_0 - 2)}{\ln 2} P_{sat}^{-3dB} \tag{2.22}$$

2.5. *Small signal model*

From the previous equation *(2.20)*, we can deduce that considering the perturbative theory, the SOA gain can be modelled as a first order filter. We can find this filter by expressing $h_i(t)$ as:

$$h_i(t) = \bar{h}_i + \partial h_i(t) \tag{2.23}$$

Where $\bar{h}_i$ is the average of the integrated gain and $\partial h_i(t)$ are the zero-mean fluctuations. In the small-signal model approach, it is supposed that $\bar{h}_i \gg \partial h_i(t)$. So we have the total output power as:

$$p_{out}(t) = \sum_{i=1}^{N} p_{in_i}(t) G_i(t) \tag{2.24}$$

The gain $G_i(t)$ is written as a constant term and the small signal time variation:

$$G_i(t) \approx \bar{G}_i(1 + \partial h_i(t)) \tag{2.25}$$

We can linearize the time variations as:

$$dh_i(t) \approx l_i(t) * \ d\bar{p}_{in}(t) \tag{2.26}$$

Where * denotes convolution in time domain and $l_i(t)$ is a low-pass filter. The impulsional response is the one expected for a first order low-pass:

$$l_i(t) \triangleq K_i e^{-t/\tau_{eff_i}} u(t) \tag{2.27}$$

Where u(t) is the unit step function and K_i and τ_{eff_i} are given by:

$$K_i \triangleq \frac{1 - e^{\bar{h}_i}}{\tau_{c_i}} \tag{2.28}$$

$$\tau_{eff_i} \triangleq \frac{\tau_{c_i}}{1 + \bar{p}_{out}} \tag{2.29}$$

More details of this derivation can be found in appendix B. Note that τ_{eff_i} defines the cut-off frequency f_c of the filter as:

$$f_{c_i} = \frac{1}{2\pi\tau_{eff_i}} \tag{2.30}$$

The variations of $h_i(t)$ are converted into phase variations due to the linewidth enhancement factor defined in *(2.12)* and are the responsible of the SOA nonlinear chirp. So the small signal model let us to conclude that the saturation of the SOA gain can be modelled as a first order low pass filter with cut-off frequency equal to f_{c_i}.

From *(2.12)* in fact we can deduce that electrical field at the output of the SOA will be:

$$E^i_{out}(t) = \ E^i_{in}(t)\ e^{h_i(t)(1-j\alpha_i)/2} \tag{2.31}$$

Different terms can be identified in this formula if we consider the perturbative model *(2.23)*:

$$E^i_{out}(t) = \ E^i_{in}(t) * e^{\frac{\bar{h}_i}{2}} * e^{j\frac{\alpha_i \bar{h}_i}{2}} * e^{\frac{\partial h_i(t)}{2}} * e^{j\frac{\alpha_i \partial h_i(t)}{2}} \tag{2.32}$$

First exponential represents the gain of the SOA. Second exponential is a constant phase shift related to the linewidth enhancement factor. This term is not considered as a severe impairment since it can be compensated with CPE algorithms in coherent receivers. Third term represents the changes in the envelope of the signal to the variations in gain. This value is related to relative intensity noise (RIN) response. Finally, the last term is the one which transfers envelope variations to phase variations, also called as nonlinear phase noise (NLPN), induced by the linewidth enhancement factor. So, we see that analyse the RIN response of the SOA allows us to characterize the dynamic regime of the SOA.

2.6. *Relative intensity noise response*

In order to extract the carrier-lifetime of the SOA, the dynamic regime of the SOA, represented by $\partial h_i(t)$, must be studied.

As in semiconductor lasers, the RIN response describes the power fluctuations of the signal. We can define the RIN response as the variation of the output power normalized to its constant power as:

$$RIN = \frac{\partial P_{out}}{\overline{P_{out}}} \tag{2.33}$$

Where P_{out} is the sum of a constant term $\overline{P_{out}}$ and the term which changes in the time ∂P_{out}.

$$P_{out} = \overline{P_{out}} + \partial P_{out} \tag{2.34}$$

This magnitude is frequently measured in frequency domain. We can define the RIN response in this domain as:

$$RIN(\omega) = \frac{\partial P_{out}(\omega)}{\overline{P_{out}(\omega)}} \tag{2.35}$$

Where ω is the angular frequency. Using previous equations we can finally reach to a formula which presents the form:

$$RIN(\omega) = 1 - \frac{H_0}{1 + j\omega\tau_{eff}} \tag{2.36}$$

Where H_0 is defined as:

$$H_0 = \frac{(\bar{G} - 1)}{(\bar{G} + \frac{1}{\overline{P_{in}}})} \tag{2.37}$$

Note that the RIN response can be expressed as the complementary filter of the one obtained for the saturation of the SOA gain with the small signal model. The RIN response can be modelled as a high pass filter and its cut-off frequency is f_c which is already defined in *(2.30)*.

2.7. *Model parameters extraction*

2.7.1 Device under test

In this section we extract experimentally the different parameters such as gain, saturation power, noise figure which are needed to assess the reservoir model depicted previously. As a device under test (DUT) a state-of-the-art SOA has been selected. This SOA, commercialized by Thorlabs, has been optimized to work in C-band (according to its specifications from 1528 nm to 1562 nm). We have decided to use this standard multi-quantum well SOA to avoid possible additional effects associated to an ultra-wideband SOA. Indeed, the fact of

using a state-of-the-art SOA in this chapter allows us to emphasize in the next chapter the differences with the novel ultra-wideband SOA.

In Fig. 2.5 we show the specifications of the DUT provided by Thorlabs. In Fig. 2.5-a) we observe the optical output power and the forward voltage as a function of the bias current. Note that as explained in *(2.1)* the SOA has a transparency current. Below this value the inversion of population is not accomplished and the output power is low. For this state-of-the-art SOA, the transparency current is around 100 mA. The output power then increases gradually with current. A biased current of 500 mA is selected, which is considered the operating current for this entire chapter.

The ASE noise spectrum can be obtained by measuring the output power of the SOA when there is no input signal. The ASE noise spectrum gives us a first idea of the total optical bandwidth of the SOA device. In Fig. 2.5-b) we observe the ASE noise spectrum at the operating current. It has been highlighted in this figure the optical band of the SOA considering it as the region between the two points where the ASE noise spectrum is decreased by 3 dB from the maximum value. As commented previously the band of this device is centred in the C Band, more precisely between 1525 and 1575 nm, leaving 50 nm of total optical bandwidth.

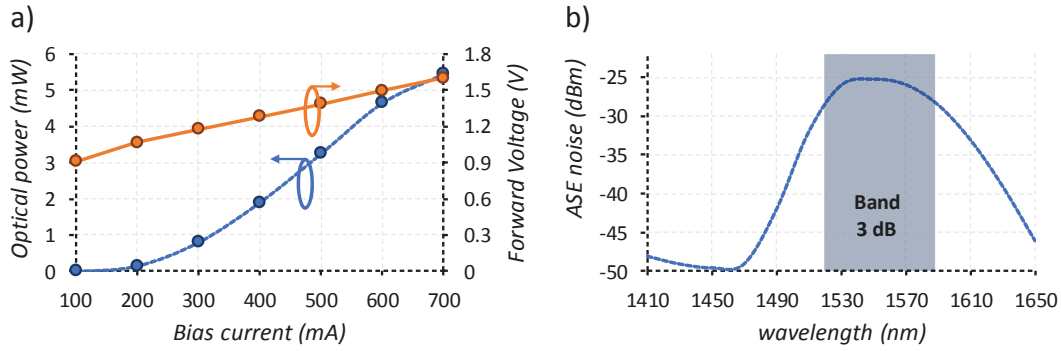

Fig. 2.5: Specifications given by Thorlabs: optical power for different bias currents in (a) and ASE noise spectrum at 500 mA in (b)

2.7.1 Test beds for SOA characterization

We can differentiate two different operation regimes in the SOA, the static and the dynamic regimes. Each regime uses certain parameters that must be characterized to model the SOA. To extract them, two different set ups have been considered.

a) Gain, saturation power and noise figure (static parameters)

In this section, the test bed used to characterize the gain and the saturation power of an SOA is explained and depicted. Firstly, some continuous wavelengths (CW) are generated by using several DFB lasers. These channels are multiplexed by an optical coupler. The wavelengths are selected in order to cover the whole operational range of the SOA. The multiplexed signal passes

through a variable optical attenuator (VOA) to control the input power that enters inside the SOA. Then a 99/1 optical coupler and an optical isolator are placed with the aim of monitoring the input signal and isolate the possible feed-back of the SOA. The 1% arm is connected to an optical switch, the 99% signal goes to the SOA under test. Finally, the output of the SOA is also isolated and connected to another port of the switch. On the other hand, the common output of the switch is connected to an Optical Spectrum Analyzer (OSA). Before starting the measurements, all the channels of the switch have been calibrated with a power-meter.

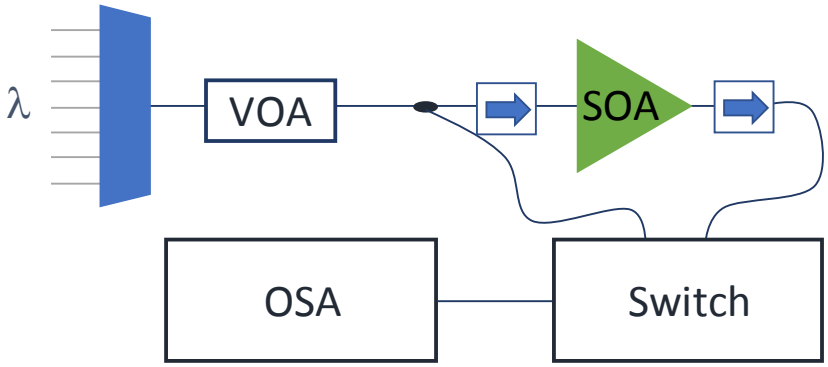

Fig. 2.6: Test-bed used for characterizing the gain and the noise figure of the SOA

To measure the NF of the amplifier we apply the formula depicted in *(1.48)*. According to this formula, input power and the optical signal to noise ratio (OSNR) at the input and at the output must be measured for all the channels. It can be done with the set up presented in this section but taking into account one consideration. If we transmit at high input power, the output OSNR is near to the input OSNR. In the formula *(1.48)* there is a subtraction of the contribution of input and output OSNRs in dBs. Therefore, if we cannot extremely precise the OSNRs, the value to be estimated will be extremely sensitive to measurement uncertainties. It is even more accentuated if we consider that input OSNR is generally elevated, even impossible to be accurately measured due to the noise floor of the OSA.

To avoid this issue, a low input power is selected. If we operate at this regime we succeed in increasing the difference between the input and the output OSNR. With these conditions, the contribution of output OSNR dominates, making even negligible the input OSNR and increasing significantly the accuracy of the estimation.

b) Relative Intensity Noise response (for dynamic parameters)

The carrier lifetime for semiconductor optical amplifiers is in the same order of magnitude than the signal symbol period. It makes the SOA reactive to amplitude changes and the dynamic regime must be characterized. A good choise is to measure its Relative Intensity Noise because indeed we can extract easily the carrier lifetime from it.

In the past, several techniques have been used to measure the RIN

response [64]. In our case, the procedure selected consists in launching some white noise into the SOA centred at the wavelength under test with a bandwidth of at least several tens of GHz. The setup used to do that is specified in Fig. 2.7. We cascade the ASE noise generated by three different stages of EDFA, filtered by two filters of 1.1 nm bandwidth, centred at the target wavelength. Then, two optical switches are used to measure the input and the output signals of the SOA. Finally the signal is converted to the electrical domain with a photodiode and measured with an electrical spectrum analyzer (ESA). In the ESA we can see the frequency response of the RIN suffred in the pass along the SOA. Several aquisitions are taken per wavelength which and averaged in order to reduce the noise in the measurements. Using the frequency response of the injected signal and substracting it from the frequency response of the SOA output, we obtain the RIN response of the SOA.

The graphic plotted in Fig. 2.7. shows an example of the RIN response measured for a SOA amplifier. In this figure, the spectrum of the signal at the input of the SOA is represented in blue. Then the RIN response at the output is shown in red. We can see how the SOA has filtered the white noise at the input for lower frequencies. Processing these two signals be obtain the RIN response of the amplifier, plotted in green. In section 2.6.4 we provide the results of the RIN response for the DUT.

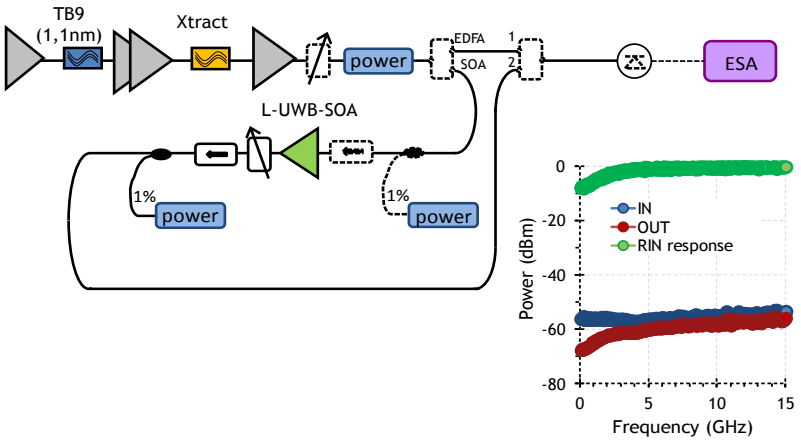

Fig. 2.7: Test-bed used for characterizing the RIN response of the SOA

2.7.2 Gain and saturation power

Fig. 2.8-a) shows the gain measured experimentally for the DUT at 5 different wavelengths which have been distributed though the whole band. The test bed used was already described in section 2.6.1. To obtain the dependences with input power, and obtain the gain at the different operational regimes of the SOA, we have ranged this value uniformly from -18 dBm to 4 dBm. Finally, we have taken a point at -22 dBm to measure the gain at high linearly regime which corresponds with g_o. We have not taken a lower input power because the contribution of the ASE noise cannot be neglected for lower input power values corrupting the signal power measurement. First thing to notice is the fact that g_0 is not the same for the whole band but slightly increases

at higher wavelengths. Fig. 2.8-b) shows the measured values of g_0 for the 5 wavelengths. We observe a small signal gain g_o around 28.5 dB. It is important to notice that g_0 behaves similarly as the ASE noise spectrum depicted in Fig. 2.5-b) with a maximum value around 1550 nm.

In Fig. 2.8-b), the saturation power (P_s) is also shown. P_s ranges from 9 dBm at short wavelengths to 15 dBm at higher wavelengths. This behaviour of increasing the saturation power along the band is expected since P_s, defined in *(2.6)*, depends on the frequency of the signal. In EDFA amplification this effect is even positive because EDFA can work in saturated regime without generating nonlinearities and the fact that the saturation power changes along the band helps adjusting the gain tilt with the bias current. In SOA by contrast, this effect may become an issue as shorter wavelengths enter in the nonlinear regime at lower input powers than other wavelengths.

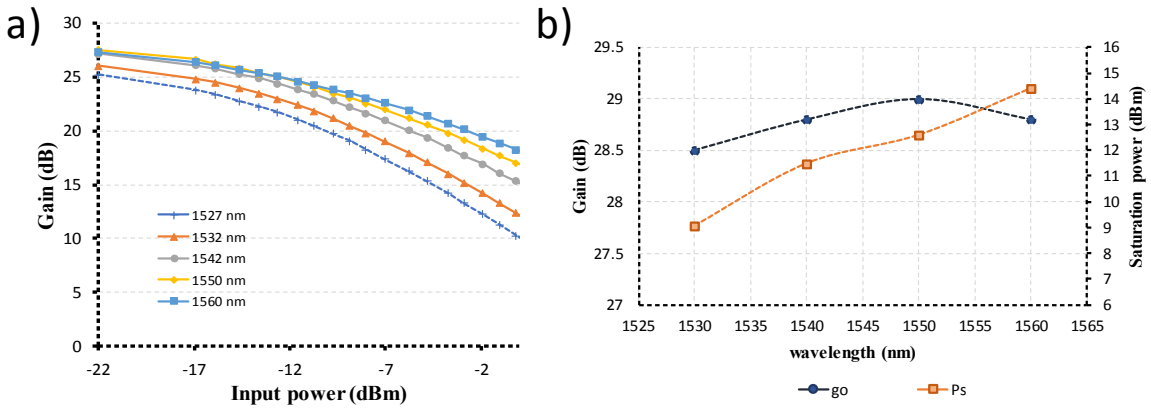

Fig. 2.8: Gain of the SOA as a function of input power for different wavelengths as a function of the input power in (a) and Gain (left axis) and P_s (right axis) as a function of the wavelength (b)

These measured values of P_s are used for tuning the reservoir model, however it is difficult to deduce a system interpretation. From the point of view optical of WDM transmission system design, it may be more interesting to deal with the input saturation power $P_{sat_{in}}^{-3dB}$ because it gives us a better idea of the input power we can operate the SOA without nonlinear impairments. In Fig. 2.9-a) is shown the input saturation power of the SOA for different wavelengths. We observe that this parameter ranges from -19 dBm to -12 dBm. It means that at -19 dBm of total input power, the shorter wavelengths will start saturating. This saturation effect does not reach the longer ones until the power is increased up to -12 dBm.

The total power at the output of the fibre is usually ~0 dBm. So, we observe that this SOA does not match with the requirements for WDM transmission. In next sections, we quantify the nonlinear penalties generated by the SOA when working in nonlinear regime. In Fig. 2.9-b, the total output power of the SOA is shown. We observe that at the operating current (500 mA) the output power is hardly higher than 15 dBm. For a C band system, the output

power of the SOA should be at least 19-20 dBm to ensure a power of 0 dBm per channel corresponding to the nonlinear threshold of typical optical fibres.

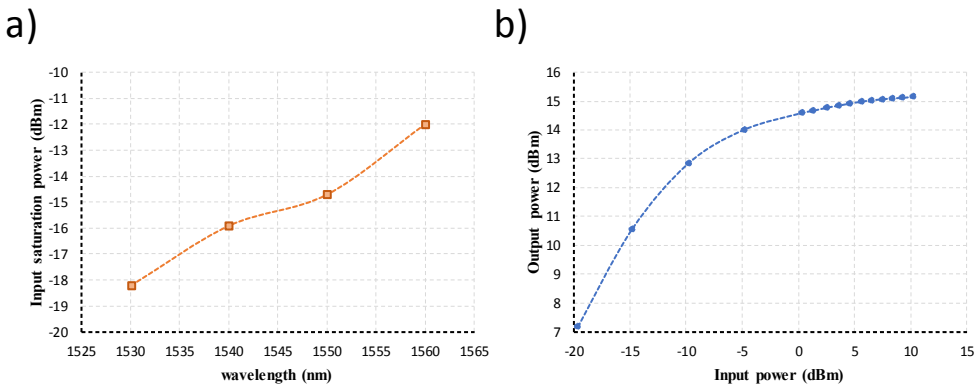

Fig. 2.9: Input saturation power as a function of the wavelength in (a) and total output power as a function of total input power (b)

2.7.3 Noise figure

In this section, the noise figure of the state-of-the-art SOA is estimated by using the procedure and the test bed depicted in Fig. 2.6. Noise figure is an important parameter in system design since it limits the final reach of the link. In Fig. 2.10, the NF for 5 different wavelengths is shown. It is observed that NF presents a tilted shape with the optical band. While this value is estimated in 10 dB at 1525 nm, it comes down to 8.5 dB at 1560 nm. This behaviour is explained by the fact that inversion of population of carriers is not completely accomplished for lower wavelengths so the contribution of the spontaneous emission of radiation becomes more important increasing the NF at this part of the spectrum.

This figure is very illustrative since it enables us to see the fact that NF tends to be higher for lower wavelengths. It is in line with *(2.8)* because it shows that the saturation power presents a linear dependence with frequency. It also permits to see the fact that the SOA has higher NF than EDFA due to the extra losses inside the cavity. As a comparison, EDFA amplifiers have a NF of around 5 dB. This supposes an important degradation of the OSNR if we cascade several spans, see *(1.45)* where OSNR is given as a function of the link parameters.

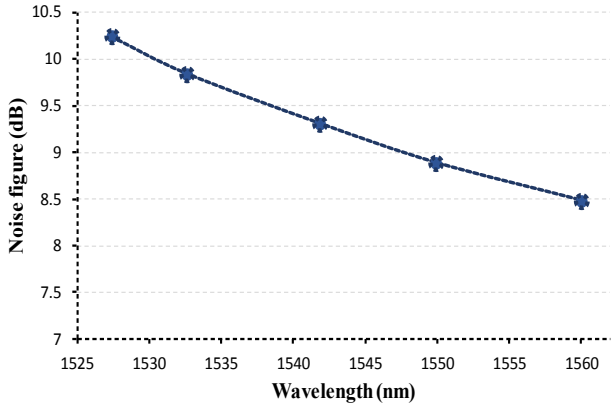

Fig. 2.10: Noise figure for different wavelengths

2.7.4 Relative intensity noise response

With the test bed depicted in section 2.6.1, the RIN response of the SOA has been measured. In Fig. 2.11, it is represented as a function of the frequency for the DUT at 1550 nm for different input powers which range from -10 dBm to 2 dBm. The values measured experimentally are represented with dots. We observe the characteristic filtering effect explained in the model that becomes more important when moving into the high nonlinear regime. This effect can be modelled by using the parameters defined in the equations *(2.36)* and *(2.37)*: Ho and τ_{eff}. Ho can be easily derived from the static parameters which have been extracted before: the gain and the saturation power. For the τ_{eff}, the effective carrier lifetime, it is also necessary to estimate the carrier life time τ_c. We know that the RIN response can be represented by a high pass filter of first order and the cut-off frequency is related with the τ_c as depicted in equation *(2.30)*. We consider that the τ_c is equal to 200 ps since it is the value that better fits with the experimental results. The results of the model for this value of carrier lifetime have been also plotted in the same figure. We observe how our model can effectively match the RIN response and therefore predict the dynamic regime of the SOA from the static values measured.

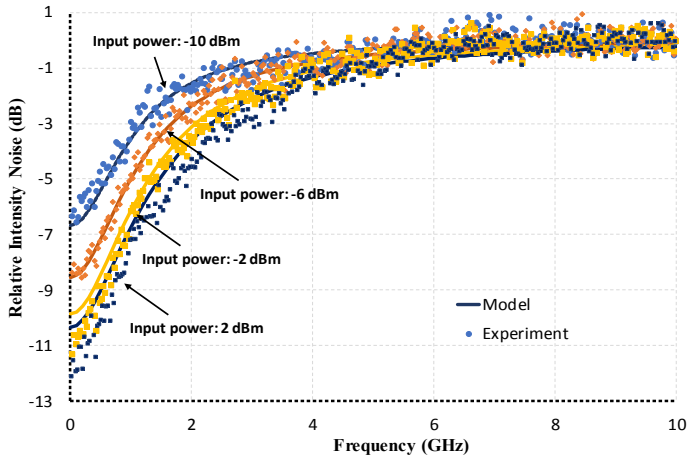

Fig. 2.11: RIN response for different input powers into the SOA in points the experimental values and in continuous line the model prediction at 1550 nm

Finally in Fig. 2.12 we can see the values of Ho and τ_{eff} estimated by the model and the ones obtained from the values of RIN response measured experimentally for two different wavelengths. We see a good agreement between them. The small discrepancies for 1530 nm are attributed to the fact that the gain of the SOA is lower for this wavelength adding more difficulties to correctly discriminate the RIN response from the own noise floor of the ESA. However, the fact that Ho is lower for 1530 nm can be predicted by the model. The lower this parameter is, the higher the saturation regime becomes. This is in line with what we have observed previously that saturation power was lower at this region of the spectra. We can notice in the figure on the right that τ_{eff} is independent of the wavelength, but decreases when increasing the input power. Although not measured beyond 2 dBm, it seems to progressively saturate at high input power, which may be of interest for WDM system operation with dual stage amplification structures.

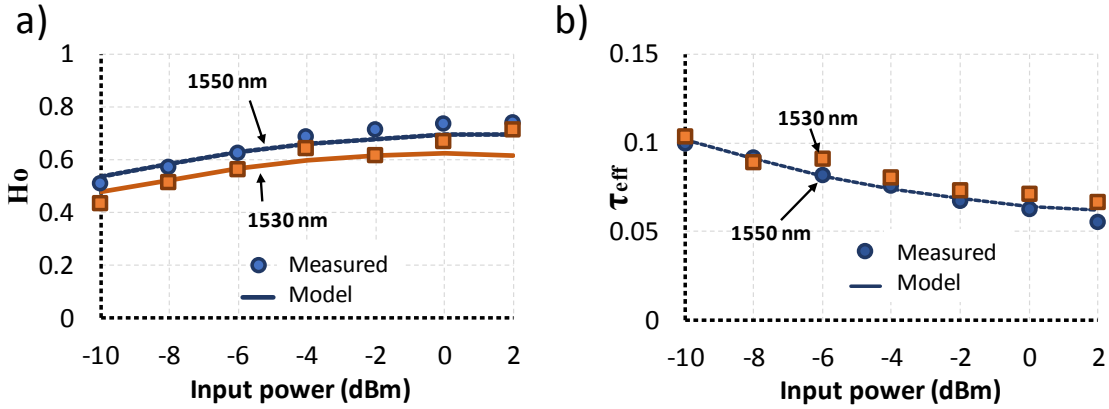

Fig. 2.12: Ho and τ_{eff} estimated by the model and measured experimentally for 1530 nm and 1550 nm

2.8. ***Experimental assessment of the reservoir model***

In previous sections some important parameters of the state-of-the-art SOA such as gain, saturation power and carrier lifetime have been extracted. The last parameter to be characterized to correctly model the dynamics of the SOA is the linewidth enhancement factor. The linewidth enhancement factor, also known as Henry factor, is introduced in *(2.11)* and it is responsible of the conversion of the amplitude variations into nonlinear phase noise. In the past, some techniques have been proposed in order to estimate this parameter [65, 66]. In our case, we have chosen to estimate it with a coherent receiver by analysing the signal traces in time domain obtained experimentally with a high-sampling rate oscilloscope. The results are compared with those obtained numerically from the reservoir model, defined with the equation *(2.20)*.

We begin with a simple constellation format, OOK, at a low symbol rate in order to estimate the linewidth enhancement factor of the SOA and then we

assess the reservoir model with more complex modulation formats at higher symbol rates.

2.8.1 Single-channel 11 GBd OOK

The goal of this section is to estimate the linewidth enhancement factor of the state-of-the-art SOA.

a) Test bed

The fact that the carrier lifetime is in the same order of magnitude as the symbol duration of the transmitted signals makes the SOA reactive to envelope variations of the total optical field. This effect is similar to the SPM in the optical fibre and distorts the waveform of the signal in the time domain. With a high-sampling rate oscilloscope capable of measuring signals at a high sampling per symbol (sps) rate and choosing the adequate input signal, it is possible to clearly observe the nonlinear impairments produced by the SOA in nonlinear regime.

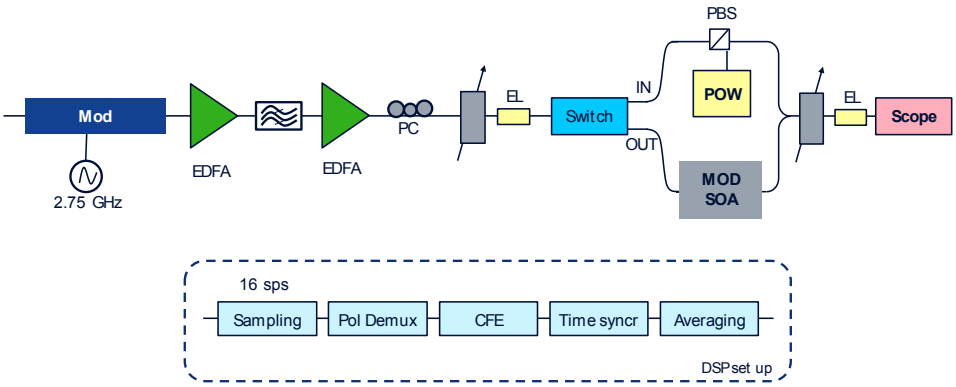

Fig. 2.13: Test-bed used for single-channel measurements

In Fig. 2.13 is shown the test bed considered. The test channel is generated with a dual-polarization I/Q modulator driven by a dedicated DAC operating at 88 Gsamples/s and loaded with Debruijn sequences of length 2048 symbols. The same sequence is loaded in both I/Q polarizations to emulate a single polarization transmission. The modulation used is an 11 GBd on-off keying filtered by a Bessel filter. The wavelength used as a carrier is centered at 1545.72 nm and has been generated with a DFB laser. To compensate for the modulation insertion losses, this channel is amplified in a two stage EDFA amplifier with a filter of 1.1 nm bandwidth inserted in the middle to filter out the ASE noise. A polarization controller is used at the input of the SOA to control the polarization state of the signal. We control the input power with a variable optical attenuator (VOA). Using a switch, we launched either the input signal or the signal at the output of the SOA into the oscilloscope. A second VOA is used to control the power that enters the oscilloscope.

In reception, several long acquisitions of the signal are registered with the high-sampling rate oscilloscope to be processed offline. The signal is sampled at 16 sps so that distortions from the SOA can be observed. Offline, we make the polarization demultiplexing to recover the polarization. The carrier

frequency estimation (CFE) is also done before temporal synchronization of the different acquisitions. The last step is to average them out to minimize the impact of the noise caused by the phase of the laser.

The constellation which better permits to see the nonlinear impacts of the SOA is OOK since it is an intensity modulation format, so it is the one selected to modulate our signal. On the other hand, as the reservoir model has shown, the SOA saturates progressively as a first order filter. The higher the symbol period is, the higher the nonlinear effect is expected. This is why a symbol rate down to 11 GBd has been selected to clearly see the SOA nonlinearities. We check this statement later in this section.

b) Intensity characterization

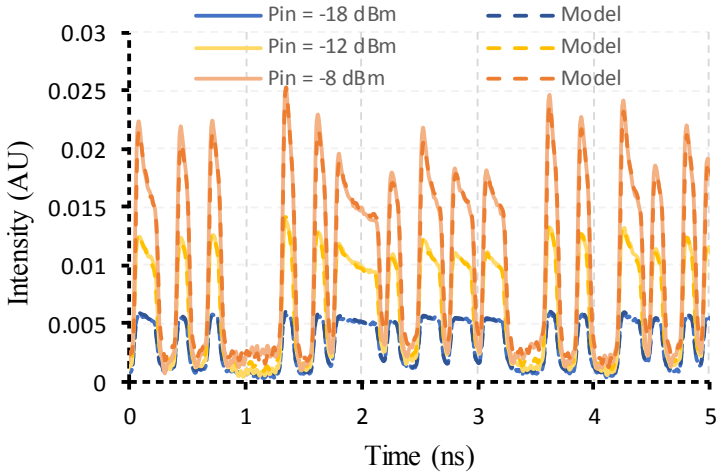

Fig. 2.14: Experiments (continuous line) vs model (dashed line) for single-channel SP-11GBd OOK. The intensity is represented in time domain

Fig. 2.14 shows the intensity of the optical field for different input powers at the output of the SOA. In continuous line the experimental data is shown while the results of the model are plotted in dashed line. We have decided to take some measurements at different input powers to see the SOA operates in linear and in saturated regime: -18 dBm, -12 dBm and -8 dBm. It is important to remember that the input saturation power at this wavelength (1545.72 nm) is -14 dBm according to Fig. 2.9.

We observe that when input power increases, nonlinear effects become higher because the saturation of the SOA becomes more and more important. At -18 dBm, the SOA operates practically in linear regime and the degradation suffered is not significant. At -12 dBm the degradation begins to be remarkable. Finally at -8 dBm, the SOA operates clearly in nonlinear regime and the impact degrades notoriously the signal.

We also observe how precisely the model is able to follow the intensity effects produced by the SOA for every input power. There is a very good matching even in highly nonlinear regime. It confirms that it is a good approximation to consider that the SOA saturates as a first order low pass filter.

c) Phase characterization

To model the phase of the OOK signal first we need to find the correct value of the linewidth enhancement factor. The procedure used to estimate it is the following one: we have computed the phase variance of the experimental data for every input power. Then we have compared it with the results provided by the model at different linewidth enhancement factors which range from 2 to 7. Finally, we have taken the one that provides the best fit with the experimental results. The metric used to calculate the fitting is the normalized root-mean-square deviation (RMSD).

Results are plotted in Fig. 2.15-a). We can see the normalized RMSD as a function of linewidth enhancement factor (used by the model). We observe that this function takes a minimum value of 1% for a linewidth enhancement factor equal to 4.8. It means that this is the best estimation of the Henry factor which is consistent with the values commonly measured [66, 67].

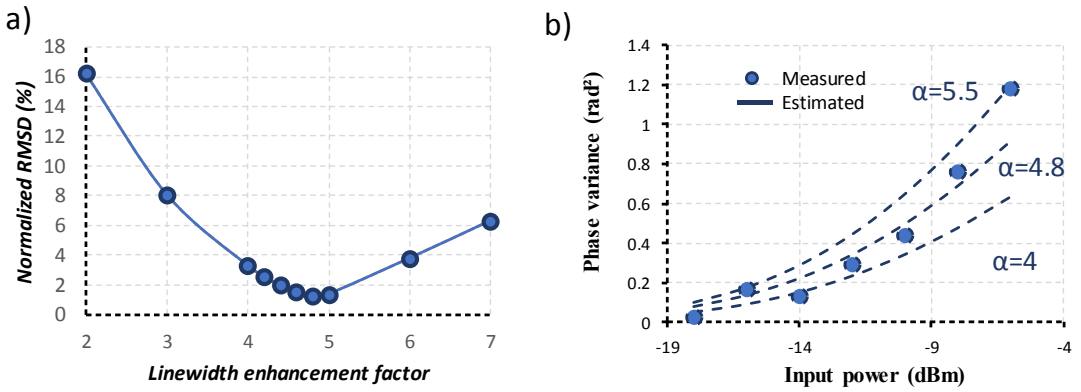

Fig. 2.15: Normalized root-mean-square deviation of the phase variance as a function of the linewidth enhancement factor in (a) and Phase variance measured (circles) vs model (line) in (b)

Besides, in Fig. 2.15-b), the experimental phase variance is plotted together with the ones computed by the model for linewidth enhancement factors equal to 4, 4.8 and 5.5 as a function of input power. Although a Henry factor of 4.8 shows a good approximation, a fine adjustment can be made as a function of the input power. We observe that the best fit for low input powers (linear regime) is obtained for values closed to 4 while for high input powers (non-linear regime) is next to 5.5 confirming that Henry factor slightly increases with input power [66, 67].

In Fig. 2.16-b), we show the phase variance measured and the estimated by the model taking this consideration into account. We observe a good match that allows us to conclude that a coherent receiver can be successfully used to measure the linewidth enhancement factor of a SOA.

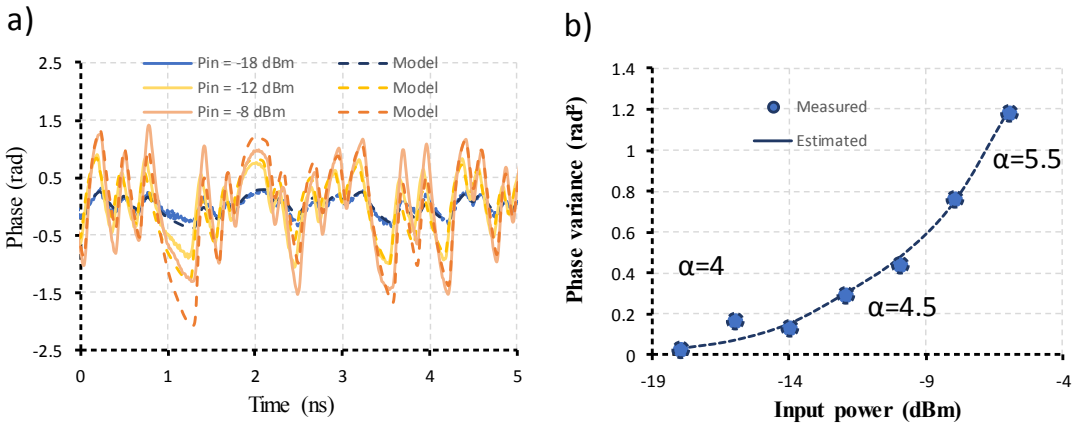

Fig. 2.16: Experiments (continuous line) vs model (dashed line) for single-channel SP-11GBd OOK. The phase is represented in time domain

In Fig. 2.16-a), the behaviour of the phase is shown for the same input powers than for the intensity characterization: -18 dBm, -12 dBm and -8 dBm. We have fitted the linewidth enhancement factor of the model with the values that presents a better fit which are 4 for -18 dBm, 4.5 for -12 dBm and finally 5.5 for -8 dBm.

The phase is correctly estimated for linear regime; however, the accuracy of the model is lower for high nonlinear regimes. We observe that when the input power increases, forcing the SOA to operate in the nonlinear regime, the behaviour of the phase is not well estimated by the model.

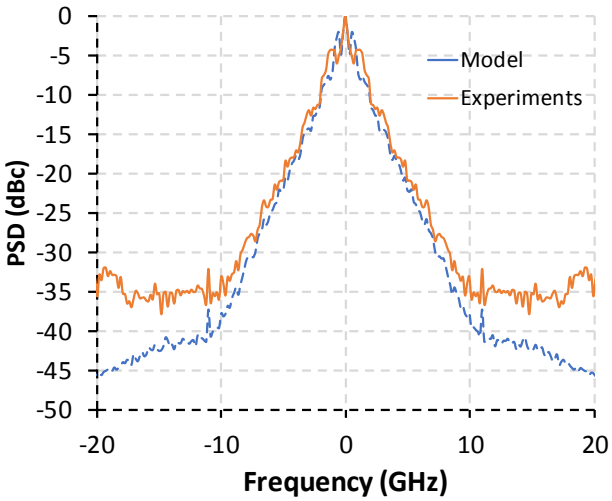

Fig. 2.17:PSD of the phase, measurement vs model

Finally, we have measured the power spectral density (PSD) of the phase at the output of the SOA and we have compared it with the one obtained by the reservoir model. Fig. 2.17 shows the results of this comparison. We plot the PSD for both cases at input power of -12 dBm and considering a linewidth factor of 4.8 (model). The phase at the output of the SOA is not zero but it presents some nonlinear phase noise due to conversion of the amplitude variations in phase variations. We observe that this phase obeys the classical

response of a first order filter to a pulse signal with the cut-off frequency measured previously with the RIN response. The good matching between model and observations demonstrates that the reservoir model is capable of well predicting the dynamics of the SOA for an OOK input signal.

d) Impact of symbol rate

Before moving to complex constellations and higher symbol rates, let's analyse the impact of symbol rate in the nonlinearities coming from the SOA. As we have said before, the SOA saturates as a first order low pass filter with τ_c equal to the carrier lifetime. It means that for a given carrier lifetime, the lower the symbol period is, the higher the nonlinearities from SOA will become because the SOA gets more saturated. It means that for a low symbol rate value, we expect higher nonlinear phase distortions. To assess this behaviour, a numerical simulation using the previous setup and the Reservoir model has been done but now changing the symbol rates to 11 GBd, 22 GBd and 44 GBd.

Fig. 2.18 shows the results of the phase variance of this three symbol rates as a function of the input power. We have used the linewidth enhancement factor fitted with previous experimental results. Let's take the input power equal to -6 dBm. We see that for 11 GBd, the phase variance is 1.2 rad², while for 22 GBd is 0.7 rad² and for 44 GBd is 0.3 rad².

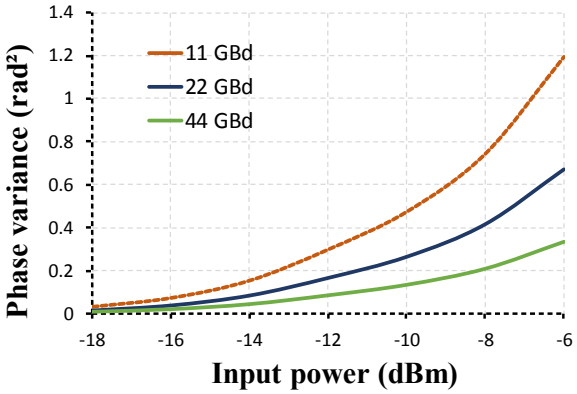

Fig. 2.18: Phase variance as a function of the input power for three different symbol rates: 11 GBd, 22 GBd and 44 GBd obtained with numerical simulations

This simulation has permitted to see the impact of the symbol rate in the nonlinear distortions of the SOA at a given carrier lifetime. The conclusion obtained is the higher the symbol rate is, the lower the nonlinearities introduced by the SOA will become.

2.8.2 Complex Constellations and coherent detection

Once estimated the linewidth enhancement factor of the SOA. In this section we assess the performance of the reservoir model for advanced modulation formats at more realistic symbol rates.

a) Single-channel

In this section, results of the model are compared with experimental data coming from different modulation formats such as quadrature phase-shift keying (QPSK) and 16-quadrature amplitude modulation (QAM). For this experiment, dual-polarization 44 GBd signals are loaded into the DAC using a randomly-generated sequences of length 36492 symbols that it is the maximum number the symbols allowed due to the DAC memory limitation. Pulse shaping was performed using root-raised cosine pulses with roll-off factor equal to 0.01. At the receiver, several acquisitions of the signal are registered with the high-sampling rate oscilloscope. The offline processing is the one described in section 1.7.

For these cases, we measured the performance in terms of Q^2 factor for different optical signal-to-noise (OSNR) values. Fig. 2.19-a) and b) show the curve of OSNR sensitivity for QPSK and 16QAM modulation formats respectively. These curves enable us to measure the impairments caused by the SOA and also to assess the performance of the model for different noise conditions. In both figures, the experimental values are plotted in continuous line while the predictions done by the model are plotted in dashed line. Finally, in black we observe the theory obtained with Montecarlo simulations in order to allow the comparison.

We have measured three different cases to see the degradation caused by the SOA at different operation regimes. In Fig. 2.19-a) we show in continuous line the experimental results for QPSK. The blue curve represents the performance at -20 dBm of total input power. As the input saturation power at this wavelength is -15 dBm, the SOA operates in linear regime and no degradation due to nonlinearities is expected. If we compare the experimental results with theory we observe a penalty of about 1 dB attributed to the imperfections in the transmitter and receiver.

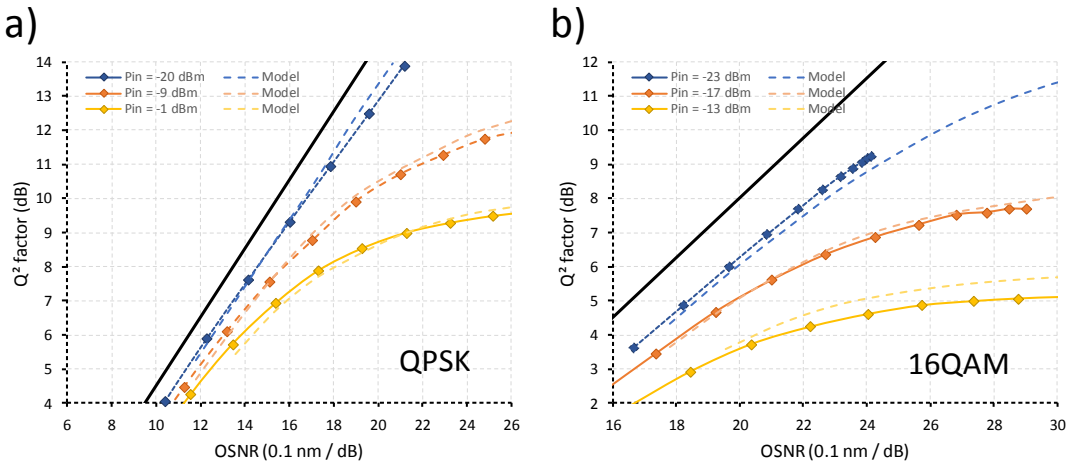

Fig. 2.19: Experimental results (continuous line) vs model prediction (dashed line) for QPSK (a) and 16QAM (b)

In orange, the same curve is plotted at -9 dBm of total input power. The SOA operates now in weakly nonlinear regime. We start to observe some

Q²factor degradation for high OSNR values due to the nonlinearities introduced by the SOA. Finally, we represent the performance at -1 dBm of input power. The SOA operates here in highly nonlinear regime. The nonlinear effects produced by the SOA become important and strongly degrade the performance at OSNR above 20 dB/0.1 nm.

The penalty coming from the SOA nonlinearities is seen at these values of OSNR because it is the main limitation in front of others such as ASE noise or Tx/Rx impairments. When decreasing the OSNR, the limiting effect finally becomes the ASE noise. This is the reason why the distance between the three curves reduces. The ASE noise hides nonlinear contributions from SOA.

In the same figure Fig. 2.19-a), we have included the numerical results of our simulations obtained with the reservoir model for the same set up configuration represented in dashed lines. We observe that the model can fit the behavior of the SOA for different OSNR in a very accurate way and efficiently estimate the penalty generated by the nonlinearities of the SOA.

Finally in Fig. 2.19-b), the same curves are plotted for PDM-16QAM but at the values of input power equal to -23 dBm, -17 dBm and -13 dBm, that are quite lower than previous ones. This allows us to conclude that the SOA is more sensitive in advanced modulation formats which will be analyze in more details later in next chapter.

As in previous figure, the sensitivity curve saturates of high OSNR values when the SOA operates in nonlinear regime. The Tx/Rx impairment is not negligible as in PDM-QPSK. This leads us to a little misestimation of the saturation value of the sensitivity curve. However, when the ASE noise becomes the limiting factor, the estimation provided by the model is more precise. Although the model tends to underestimate the impact of SOA nonlinearities at highly nonlinear regime, this does not mean a huge limitation because for transmission purposes where we will always avoid working at this regime.

b) Impact of optical fibre

When propagating a signal along an optical fibre, it is exposed to several effects. One of them is chromatic dispersion. Its impact is the increase of Peak-to-Average Power Ratio (PAPR) of the transmitted signal. As we have previously described, the SOA reacts to power variations of input signal. This is the reason why we study this effect under chromatic dispersion to correctly assess the performance of the reservoir model.

We generate a PDM-QPSK signal modulated at 49 GBd with a randomly-generated sequence of length 36492 symbols. We propagate the signal with a theoretically ideal fibre in terms of attenuation and nonlinearities and with a chromatic dispersion coefficient equal to 17 ps/nm/km which corresponds to a standard single-mode fibre (SSMF). In Fig. 2.20-a) the histogram of the real part of one polarization of the signal is shown for the signal at the input of the fibre in dashed line and after several km in continuous line. When the signal is not dispersed the two peaks observed correspond to the

projection of the QPSK signal on the real axis. Then the distribution becomes more and more Gaussian with the different lengths of the fibre. In Fig. 2.20-b) is plotted the normalized variance of the signal for PDM-QPSK (orange) and other modulation formats PDM-16QAM (gray) and PDM-64QAM (brown) as a function of the fibre length. The effect of becoming a Gaussian distribution is seen if we notice that all the signals converge after a certain number of km to the square root of 0.5. This variance corresponds to a signal with Gaussian distribution with power equal to the unity. It means that after this distance the properties of the signal are the same independently of the initial constellation format. Notice that at the input the different signals have a normalized variance which takes different values, in fact PDM-16QAM and PDM-64QAM signals present a value nearer to the target value than PDM-QPSK. This is due to the fact that these types of modulation formats present a constellation mapping more dispersed, leading to a more Gaussian-like distribution.

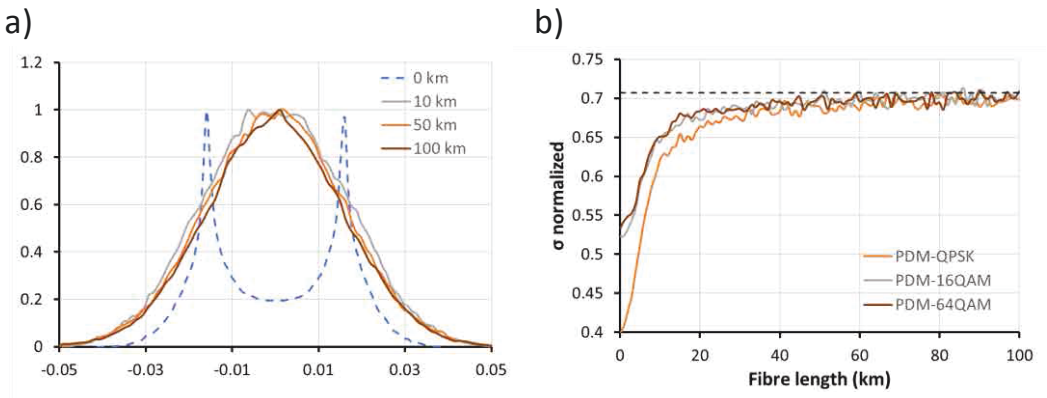

Fig. 2.20: (a) Distribution of the constellation real part of one polarization of a 49 GBd PDM-QPSK after different fibre lengths and (b) normalized variance for 49 GBd PDM-QPSK/16QAM/64QAM as a function of the fibre length

To sum up this section it appears clearly that the signal can be considered as a white random Gaussian process after several km of optical fibre (typically greater than 25 km).

c) Towards WDM transmission systems

In the previous section we have shown that propagating a signal along an optical fibre disperses the distribution of its symbols leading to a more Gaussian-like distribution after several tens of km. Now we consider the case of a WDM transmission system where several channels are spectrally multiplexed together. As in the previous case, it impacts the properties of the signal in a similar way. To analyze this effect, Fig. 2.21 represents the normalized variance of a WDM signal as a function of the number of channels. Each channel is modulated at 49 GBd PDM-QPSK with a sequence of length 36492 symbols equispaced at 50 GHz. All the sequences are randomly-generated to ensure completely independence between them. We observe that when there is only one channel, the normalized value of its variance is 0.4. It increases with the number of independent channels. When the number of channels is large enough, the normalized variance converges to the square root

of 0.5 as previously observed. It means that a WDM signal of more than ~10 channels can be approximated by a Gaussian distribution.

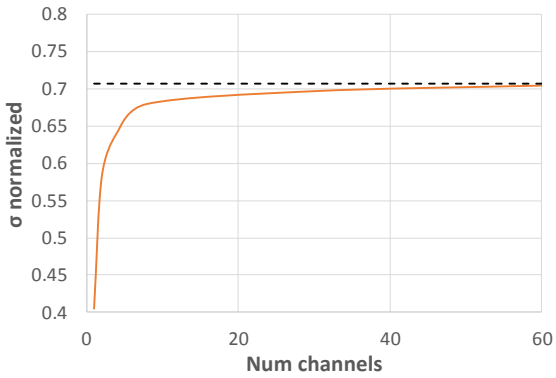

Fig. 2.21: Normalized variance as a function of the number of channels when transmitting a WDM signal with independent channels

If the transmission channels carry correlated signals, the dispersion of the signals is not guaranteed. Now we study the extreme case, where all the channels carry the same signal. In this case the normalized variance does not converge at all but increases linearly infinitely with the number of channels. This case may happen in laboratory experiments where the number of modulators is usually limited.

For laboratory purposes, where only one modulator is used for all the loading channels, the decorrelation of the channels is obtained by adding a fibre spool of several kilometers before combining them with the test channel. Due to the fact that the optical fibre has a dispersion slope, the different channels disperses when they are propagated. This effect decorrelates the sequences transmitted into the different channels. To choose the adequate length of the fibre spool, a numerical simulation has been set to assess how much the channels decorrelate between them. Measuring the power variance of the signal is a good estimator of the decorrelation between channels. In Fig. 2.22, we show the power variance normalized by the numbers of channels for different lengths of the fibre. The different curves show the variance for different number of channels which range from 1 to 60. We observe that independently of the number of channels, all the curves converge to square root of 0.5 when the fibre spool is long enough. This indicates that the signal distribution has decorrelated completely showing a Gaussian-like distribution. Considering a high number of loading channels of at least 60, typically the value used in our experiments, we have determined the required length of fibre that gives a variance difference of 1% with respect to the completely decorrelated case for the simulation with the higher number of channels. This value is 25 km and is the one we used later in our experiments.

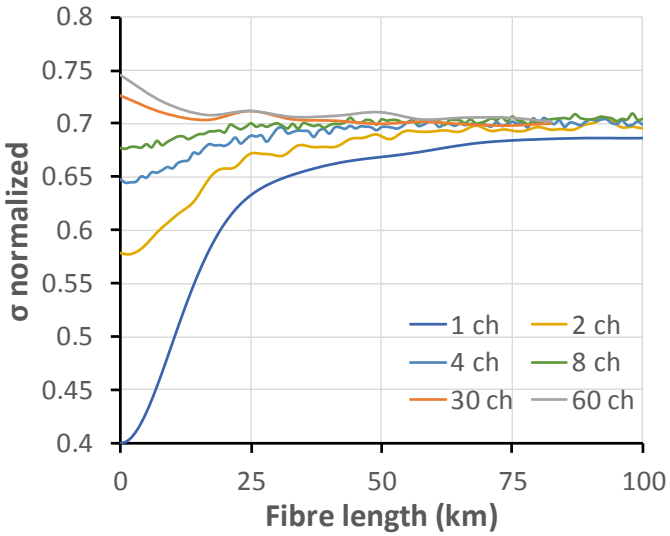

Fig. 2.22: Normalized variance for different number of channels as a function of the fibre length

The setup for this configuration is shown in Fig. 2.23. Sixty-four channels have been generated using independent laser sources following a 50-GHz grid. The 63 loading channels have been generated using a single dual polarization I/Q modulator driven by a dedicated DAC loaded by a randomly-generated sequence of length 36492 symbols at 88 Gsamples/s. In order to study correlation effects between channels, a fibre spool of 25 km of standard single mode fibre (SSMF) is eventually considered to decorrelate them. Optical EDFA amplifiers have been used to compensate for the modulator insertion losses and the losses of the fibre spool.

The test channel is modulated using an independent dual polarization I/Q modulator driven by a dedicated DAC loaded by random sequences of length 36492 symbols at 88 Gsamples/s. After being amplified with EDFA, it is coupled with the 63 loading channels.

The signal used in all the cases is a 44 GBd DP-QPSK. Pulse shaping was performed using root-raised cosine pulses with roll-off factor equal to 0.01. Finally with a VOA we control the input power to the SOA.

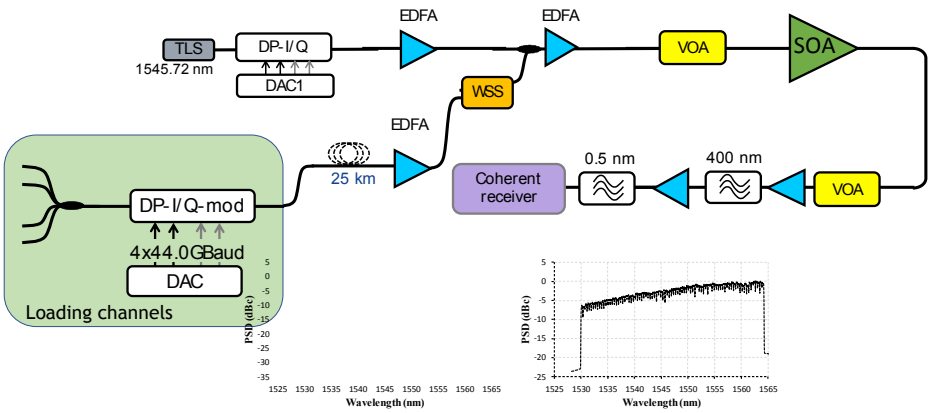

Fig. 2.23: Transmission set-up for WDM measurements

In this experiment, we investigate if there is an extra penalty when the decorrelation spool is removed, which should be induced by the higher PAPR of the input signal to the SOA as shown in previous sections due to the correlation effect between channels.

We consider two different cases: a first one where these channels are decorrelated (decorrelation fibre, DF) using the fibre spool of 25 km of SSMF and a second case where this fibre is removed (no decorrelation fibre, NDF). Furthermore, to completely validate the consistency of the model, the performance as a function of the input power has been measured for two different wavelengths: 1530 nm and 1550 nm.

Fig. 2.24 shows the results of the experiments for the two cases depicted before. We see the Q² factor represented as a function of the input power to the SOA. Firstly, we observe that when the DF is used, the Q² factor becomes higher when the input power increases up to -7 dBm. This is due to the fact that the higher input power values increase the OSNR of the signal. For powers above -5 dBm, the performance saturates. In this region, the link OSNR is very high and the system performance is mainly limited by the Tx/Rx impairments. In linear regime below -10 dBm, we observe a degradation of the performance at 1530 nm of 1 dB. This penalty is attributed to the higher NF at this part of the optical bandwidth that degrades the OSNR.

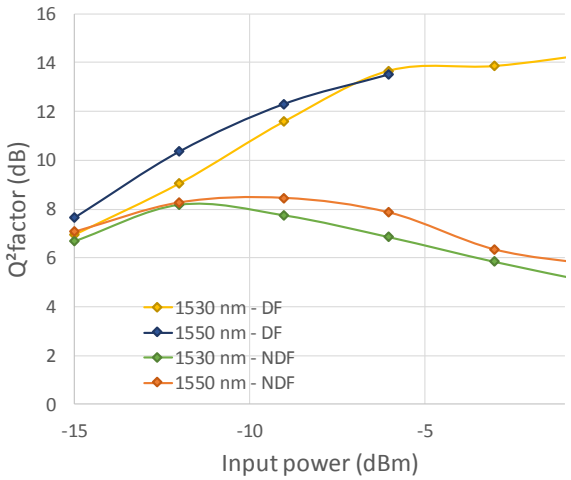

Fig. 2.24: WDM Transmission results for 1530 nm and 1550 nm with (DF) and without decorrelation fibre (NDF).

For the second case where the decorrelation fibre is removed, we clearly see a degradation of the performance with respect to the previous one. This penalty becomes more important at higher input powers. At this point, the system is not limited by the OSNR, but by from other impairments such as the nonlinearities introduced by the SOA and Tx/Rx impairments. The performance decreases with power since the SOA is operated in nonlinear regime.

It is definitely important to notice the degradation experienced if decorrelation fibre is not used for high input powers. These experimental results confirm that the use of a decorrelation fibre in experiments is mandatory if the channels are correlated between them. As explained before, this consideration

should be taken into account in laboratory experiments where the number of modulators is in general limited.

Finally, we have simulated the two cases presented in this section with the reservoir model in order to assess its performance in WDM systems. Furthermore, this is a good test bed for model validation since it permits to see if the model can correctly estimate the extra penalty added by the correlation effects between the channels.

In the numerical tool, we have considered the same two cases with (DF) and without the decorrelation fibre (NDF). Note that we have numerically introduced a short fibre of 10 m in the NDF case to simulate the impact of the optical fibres that connect the modulator and the SOA in the laboratory experiments to match with practical conditions.

Fig. 2.25 shows the same figure as Fig. 2.24 but in dashed line we have added the results of the numerical simulations obtained by the reservoir model. Again the Q²factor is represented as a function of the input power to the SOA. We notice that the model is capable of precisely estimating the performance of the SOA when the decorrelation spool is included. For the case where the decorrelation fibre is removed, the numerical model can predict well the performance in the linear regime of the SOA. But we observe small discrepancies to estimate the performance in nonlinear regime. The model does not match with results in highly nonlinear regime but it is enough for most of our experimental conditions.

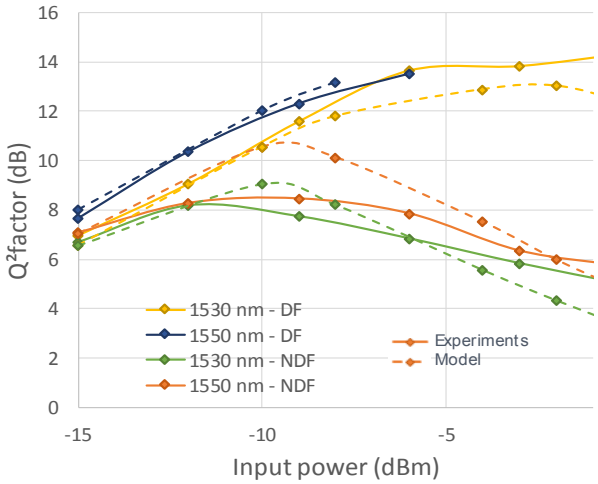

Fig. 2.25: WDM Transmission results for 1530 nm and 1550 nm with (DF) and without decorrelation fibre (NDF) for experiments and numerical simulations

2.9. ***Conclusions***

The aim of this chapter was to find a model able to characterize the performance of a semiconductor optical amplifier in the context of WDM optical transmission system design. The model selected is the reservoir model which

has been introduced and assessed. It is not the most accurate existing model but it presents a good compromise between complexity and precision.

We have divided the assessment in two different parts. In the first part, we have studied the static regime of a state-of-the-art SOA and we have extracted experimentally all the important parameters such as gain and the saturation power as a function of wavelength and input power of a state of the art SOA. In the second part, some experiments have been considered to analyse its dynamic regime. We have measured the relative intensity noise response of the SOA which has permitted to estimate the carrier lifetime of the SOA. Comparing the experimental results with the ones provided by the reservoir model, we have observed a good fit between which allow us to conclude that it can successfully estimate the dynamics of the SOA.

Finally, we have extracted the linewidth enhancement factor. With a coherent receiver equipped with a high-sampling rate oscilloscope, we have obtained some temporal traces of a single polarization OOK after passing through a SOA. We have extracted the amplitude and the phase of the signal by using signal processing techniques and then we have obtained this parameter by fitting the experimental traces with the ones provided by the model. As it was already observed in [66, 67], we have detected a little dependence of this parameter with the input power. This is the first time that the linewidth enhancement factor of a semiconductor optical amplifier has been estimated by using a coherent receiver.

Once we have obtained this last parameter, we have assessed the model by comparing in time domain the experimental traces with the ones obtained in numerical simulations. We have seen that the reservoir model can perfectly fit the experimental curves of both amplitude and phase for linear and weakly nonlinear regimes. The model begins to be imprecise in highly nonlinear regimes, specifically for the signal phase. This is mainly attributed to the overestimation of the model when estimating the SOA gain, and the small dependence of the linewidth enhancement factor with input power.

For more complex modulation formats we observe that the model still offers a good estimation of the SOA dynamics for linear and weakly nonlinear regimes. Although for high nonlinear regimes the reservoir model is too simple and some extra considerations might be considered to fix its imprecisions, for transmission purposes where the SOA will be mainly operated in linear and weakly nonlinear regimes, the reservoir model has been shown as a good alternative to be exploited.

Besides, in the last part of the chapter we emphasise the importance of using decorrelation fibres in the WDM transmission setup to ensure decorrelation between the different channels. This study can be useful in laboratory experiments where the number of modulators used is usually limited and the different loading channels are therefore correlated. Some numerical simulations have been performed to determine the minimum length of the decorrelation fibre which has been established to 25 km of SSMF when

transmitting at least 60 channels and then some experiments have been done to validate it. We observed how the extra spool helped to decorrelate the channels and thus reduce the penalty of the SOA.

Chapter 3. Moving towards ultra-wideband systems

Since the birth of the World Wide Web (WWW) in the last decade of the XX century, the world has undergone a major revolution. Internet has evolved hand in hand to cope with all the new needs that progressively have been demanded by the users. These necessities have been satisfied by the emergence of new technologies which range from the development of the first web navigators in early 90s to the concept of Internet of things in recent years.

Every approximately 5 years a new service has born, has grown up and has become the dominant one. This phenomenon has always been associated with a significant increase of the total data traffic. Fig. 3.1 shows how we can differentiate different eras of about 5 years, in each one the traffic being multiplied by 10. This trend will continue in next years. In Fig. 3.1 we observe that Internet traffic is expected to be tripled or even quadruped from 2015 to 2020. Therefore to further increasing the capacity of the optical systems will be required.

If we look at the optical fibre capacity evolution in previous decades, we observe that in the 80s, we took profit of the advances in light amplification by using techniques such as Erbium doped fibre amplification (EDFA) to compensate fibre losses. In the 90s the benefit of new techniques such as wavelength division multiplexing (WDM) allowed us to increase significantly fibre capacity by transmitting more than one channel simultaneously through a single fibre. This is considered an important breakthrough in optical communications since it allowed us to increase significantly the reach of the links and massively to increase fibre capacity. Fig. 3.2 shows the trend of the fibre capacity in last decades. Fibre capacity has been regularly increased by

an order of magnitude (x10) every 4-5 years. This tendency matches with the one observed previously in Fig. 3.1.

In the previous years, this constant increase of traffic has been accomplished by using different digital signal processing techniques with the purpose of increase the spectral efficiency of system [19][67]. Pulse and constellation shaping or digital fibre nonlinear compensation are two examples of new techniques developed in the 10s.

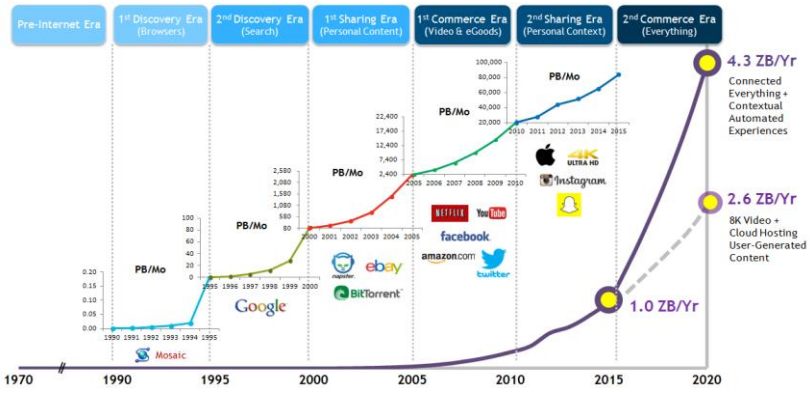

Fig. 3.1: Strong growth in internet traffic taken from [68]

Nevertheless, the effort required to further increase the fibre capacity by these means is becoming more and more challenging since spectral efficiency scales logarithmically with the signal-to-noise ratio (SNR). If we want to keep this trend of x10 every 5 years, a different technology or concept must be exploited.

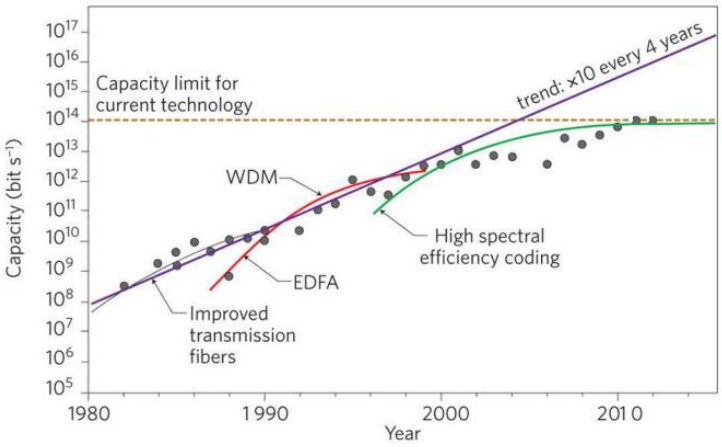

Fig. 3.2: Evolution of fibre capacity in last decades [69]

Fig. 3.3 shows different strategies to increase fibre capacity. Fibre capacity can be increased by exploiting one of these three different orthogonal axes, namely, improving the spectral efficiency of the system, increasing its bandwidth or using spatial multiplexing by propagating different signals in the same cable though multi-mode or multi-core fibres.

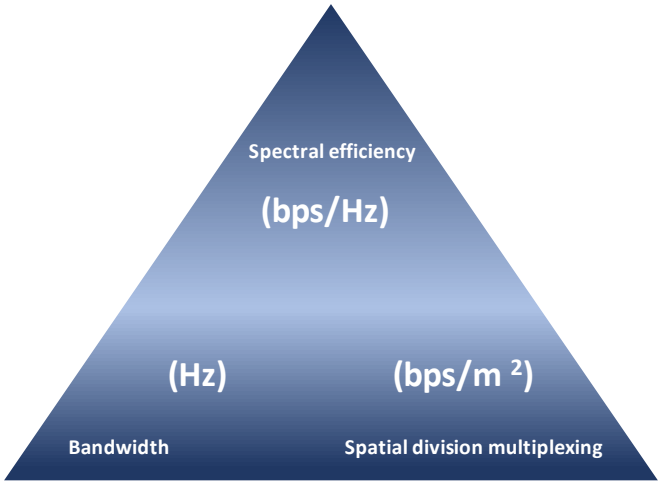

Fig. 3.3: Different strategies to increase fibre capacity

Fibre capacity increases linearly with optical band as depicted in *(1.20)*, so an effective solution to overcome the issue of increasing fibre capacity can be to increase the bandwidth of the system. Fig. 3.4 shows a figure where the fibre capacity is represented in terms of the SNR for two different systems. In green, we represent the capacity of a C Band system and in red, an ultra-wideband system which we suppose to extends the band of the traditional system by a factor of 3. We observe that the UWB system will overcome the traditional system even if we consider a higher implementation penalty due to the additional challenges we would probably need to face up to design this type of system. It can be seen more clearly with a simple example. If we take a traditional C-band system with a SNR of 20 dB, the maximum transmission throughput will be close to 50 Tbps. Imagine now an UWB system where the SNR is reduced to 18 dB due to higher implementation penalties. The capacity of the overall system will be still around of 130 Tbps, improving the fibre capacity, not in a factor of 3, but in a factor of 2.6, which is still of high interest.

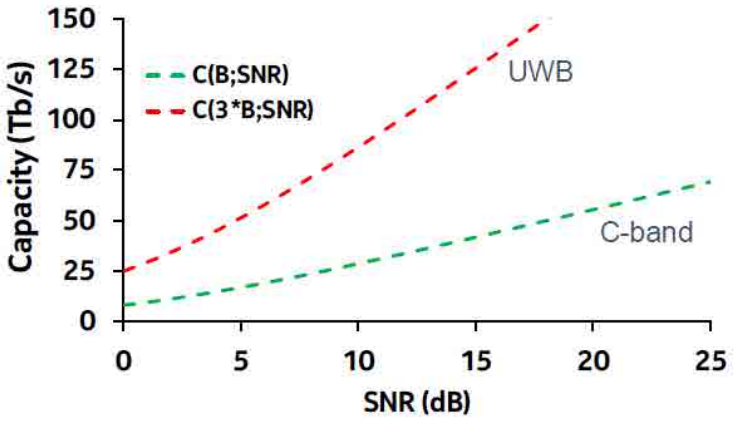

Fig. 3.4: Fibre capacity as a function of SNR for a C Band system and an UWB system

Until now the only alternative able to provide UWB amplification is Raman pumping. However, the fact of being distributed is a major issue for

optical networks. Optical networks require lumped amplification in reconfigurable optical add and drop multiplexers (ROADMs). Using Raman pumping, setups have been proposed to solve this issue, but at the expense of high complexity, cost and power consumption. The other solution to provide wide optical gain is to use of semiconductor optical amplification.

3.1. *SOA for UWB systems*

Although semiconductor optical amplification (SOA) was discovered many decades ago, it has been traditionally rejected for optical transmission purposes and it has hardly been used in limited domains such as passive optical networks (PON) [70]. For WDM transmission systems with a bandwidth of 35/40 nm, SOA is outperformed by EDFA in terms of noise figure and nonlinear induced distortions.

However, the matter of UWB amplification can change the current paradigm. EDFA is an effective technology to amplify a band of 35-40 nm, but it is extremely challenging to extend this band further. On the other hand, the SOA is a technology that can be customized to achieve wider bandwidths. This fact can tip the balance in favour of the SOA which can become the dominant technology for UWB systems. In this section, we show how an innovative and tailored SOA can accomplish the major requisites for an ultra-wideband system.

3.1.1 Polarization diversity

In order to amplify the transverse quasi electric and magnetic (TE, TM) modes simultaneously several bulk structures have been proposed in literature [71, 72, 73]. However, the issue of polarization sensitivity is not solved yet and it is still an undesirable characteristic of SOA. This feature makes the amplifier gain sensitive to the polarization state of the input beam, a property undesirable for lightwave systems in which the state of polarization changes with propagation along the fibre.

On the other hand, another approach has been proposed in [74, 75] which consists in passing the signal twice inside the SOA rotating it in between with a 90-degree polarization rotator. This choice cancels the polarization sensitivity because both polarizations are amplified by the same path. But the interactions between co and contra propagative waves in the same gain medium creates nonlinear distortions at high output power.

Finally, a last alternative is presented which exploits polarization diversity by using two SOA per module. This approach uses each SOA to amplify a single light polarization. This solution has been the preferred one to design the novel UWB SOA because it gives more degrees of freedom in the chip design to improve main characteristics such as gain, saturation power and noise figure.

The scheme used is specified in Fig. 3.5. We observe how the light enters the cavity and is split with a polarization beam splitter (PBS). The TM

mode is rotated 90 degrees with a polarization rotator in order to enter the SOA with the TE mode. Each signal is amplified with a single SOA. The signal which has not been previously rotated is now rotated at the output of the SOA to recover to the original state of polarization and finally, the two signals are recombined.

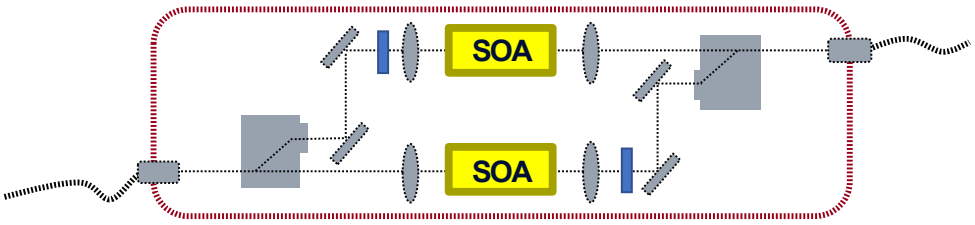

Fig. 3.5: Scheme of the SOA module using a polarization diversity strategy

3.1.2 Chip design

Once solved the issue of polarization diversity, it was necessary to tailor the chip to obtain the features which are expected to an UWB amplifier. The main requisite was a flat gain in a bandwidth close to 100 nm. Nevertheless, it was not the only issue to face up. As discussed in the first chapter, when designing an optical system, a trade-off between the OSNR and the nonlinearities of the fibre must be considered. It sets an optimal power per channel at the input of the optical link typically around 0 dBm/channel. In a traditional system of 100 channels it means to operate the optical amplifier at 20 dBm. If the optical bandwidth, and thus the number of channels, is increased the total input power will also increase. For instance, if we consider a system with 200 channels, the total power would be 23 dBm and so forth. Then, basically what is required to an ultra-wideband amplifier is high gain but also high output power. Finally, in order to increase the OSNR and therefore the reach of the system, noise figure must be as low as possible.

The UWB module done by our colleagues in III-V Labs in the National French project CALIPSO has a material made of an InGaAsP with multi-quantum well structure (MQW) structure was selected [76]. Two different quantum wells significantly increased the bandwidth of the amplifier. The design was also optimized to reach high output power by using an asymmetrical cladding structure with an underlying slab with high refractive index. This additional layer improved the saturation output power by reducing the confinement factor in the active region and in the p-doped InP. The fact that the saturation power has been increased permits to operate the SOA at higher power, this also permitted to increase the carrier lifetime of the SOA according to [65] which minimized the nonlinearities when the SOA operates in saturation regime.

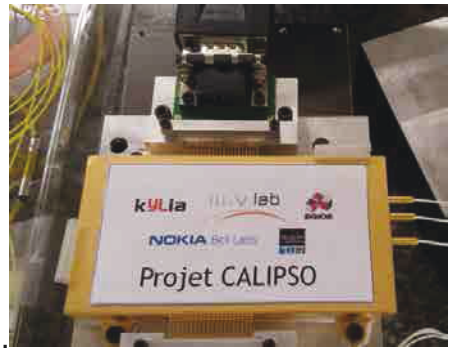

Fig. 3.6: UWB SOA module

The UWB module designed in the Calipso project is shown in Fig. 3.6 with the following dimensions:10x5 cm including optical isolators.

3.2. *UWB SOA characterization*

In following sections, we characterize the different parameters of the UWB SOA delivered in the frame of the Calipso project such as gain, output power and noise figure with the purpose of showing that the custom SOA can be used with UWB systems.

3.2.1 ASE noise profile

A simple measure that gives the optical bandwidth of an amplifier is the ASE spectrum. The SOA is biased in order to force population inversion and the ASE noise is measured as a function of the wavelength with an optical spectrum analyser.

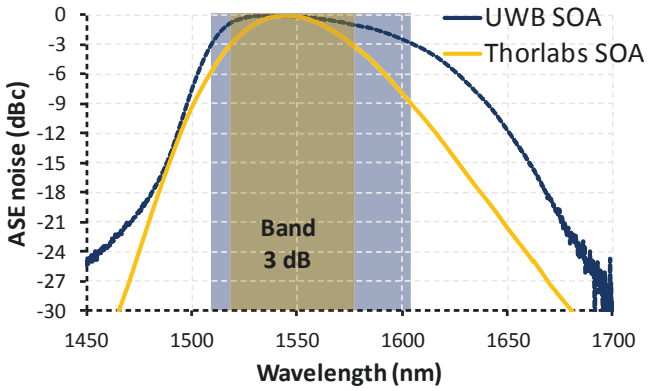

Fig. 3.7: ASE noise measured in the state-of-the-art SOA compared with the novel UWB SOA

Fig. 3.7 shows the ASE noise power spectral density (PSD) of a commercial available SOA and the UWB SOA at 500 mA of bias current. We show these curves together to emphasise the higher band of the novel device. Notice how the UWB SOA almost doubles the band of the state-of-the art SOA. While the SOA Thorlabs goes from 1530 to 1570, the UWB SOA can range from 1510 to 1605 nm.

3.2.2 Gain

The gain is an important parameter to correctly manage in an optical amplifier. It is indeed particularly challenging in an UWB amplifier since not only is needed a high gain but also flat along the whole band. In this section, we characterize the gain of the UWB with the main purpose of operating the SOA the flattest possible for the whole transmission band, let's say 1510-1610 nm.

a) Chip gain

For this novel SOA module, we first measure the gain per SOA to double-check that both integrated chips provide similar values of gain. A single polarization signal composed by several DFB lasers coupled together is used as an input signal. Then the bias current is sent only in the SOA under test. The polarization state is tuned with a polarization beam controller to maximize the power at the output of the device. With this configuration, we ensure that the polarization state is properly aligned and the whole signal enters the SOA under test.

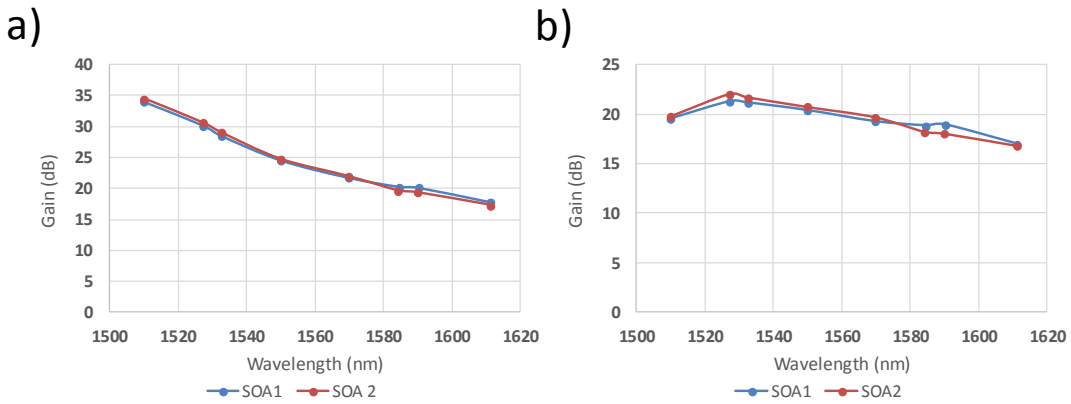

Fig. 3.8: UWB SOA module gain for both SOA for 1000 mA per SOA at input power equal to -15 dBm in (a) and at -1 dBm in (b)

Fig. 3.8 shows the gain per SOA as a function of the wavelength at two different input powers. On one hand Fig. 3.8-a) shows the gain when the device operates at linear regime. This permits us to observe the small-signal gain of the device. Small signal gain presents a tilted shape. It takes values which ranges from 35 dB at shorter wavelengths to 16 dB in longer ones. The cause of this tilt is studied later but it is related basically to the wavelength dependency of the saturation power. On the other hand, Fig. 3.8-b) shows the gain at -1 dBm input power. We have selected this value because it represents the regime where the device operates in flat regime for the whole band. We observe that the gain in average is 18 dB and presents a maximum at the beginning of C band: 1530 nm. In both cases we observe gain values similar for both SOA. So from now on, we are going to measure the gain of the entire module without differentiating per SOA. The bias current will be referred as the bias current per SOA. For instance if it is said that the module SOA operates at 1000 mA, it means that both SOA are biased at 1000 mA.

b) Module gain

In this section, we characterize the gain of the SOA module as a function of the input power and the bias current.

With this purpose we measure the gain at a given bias current for different input powers which range the different regimes of the SOA, let's say from -25 dBm to 4 dBm. With this setup, we analyse the behaviour of the gain with input power. Fig. 3.9-a) shows the results of the gain as a function of the wavelength when the UWB SOA is biased at 700 mA per SOA. For low input powers, there is a negative tilt that is reversing when increasing the power until becoming a positive tilt for high input powers. As discussed in the chapter of SOA modelling, the saturation power of the SOA depends linearly on the frequency. It causes that shorter wavelengths saturate at a lower power than longer ones. This is the reason why the gain at short wavelengths decreases with input power and is thus the responsible for the positive tilt of gain at high input power.

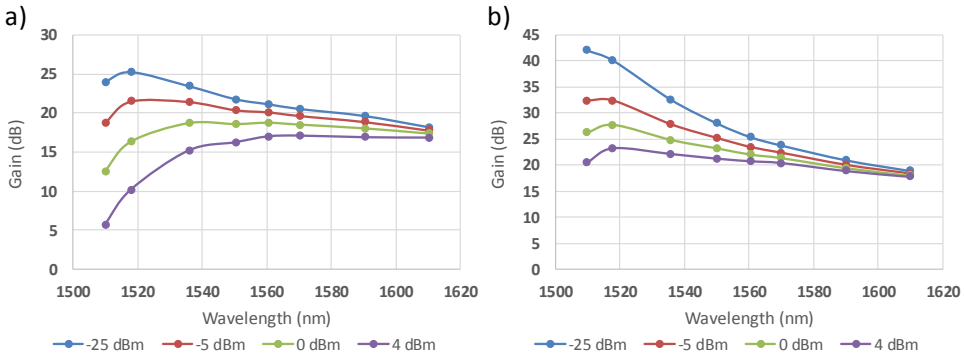

Fig. 3.9: UWB SOA module gain for different input power at 700 mA in (a) and 1500 mA in (b), currents measured per SOA

We can also measure the module SOA gain for different driven currents. In Fig. 3.9-b) the same curves for 1500 mA per SOA are shown. We observe that the negative tilt is more important than in the previous case. The fact of increasing the pumping current increases the population inversion and thus the number of carriers inside the cavity. To obtain a curve with similar tilt than for 700 mA, input power must be increased. In other words, increasing the bias current makes the SOA behave in the same way as if we had reduced the input power, tilting the gain in a negative way.

The wavelength dependency of the saturation power can be used to control the gain tilt by tuning either bias current or input power. In Fig. 3.10-a), the gain is shown for the regime where the module SOA operates at flat regime. We observe that for the whole band a gain of at least 17-18 dB with a difference of 3 dB between the maximum and the minimum gain. We have experimentally checked that for all the input powers there is an optimum driven current per SOA which permits to work at this regime of gain. For low input powers, the flat spectrum can be obtained at 550 mA, which corresponds to the bias current

where the ASE noise power spectral density is flat. Then it increases with input power following the curve shown in Fig. 3.10-b).

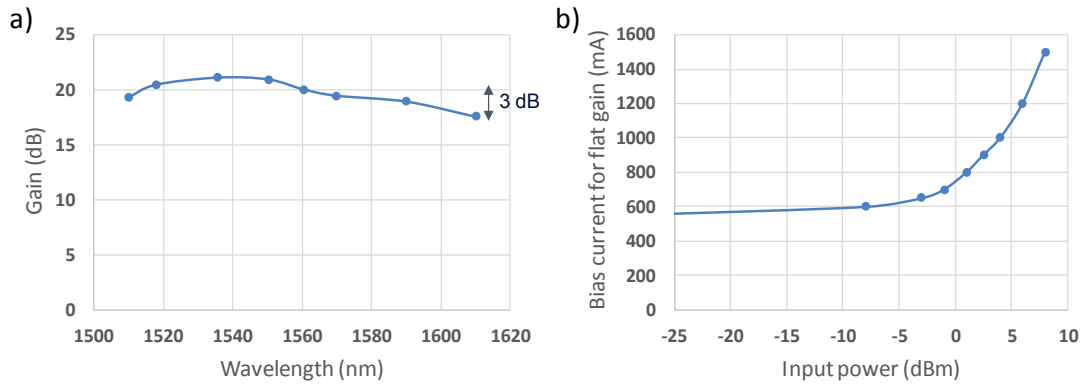

Fig. 3.10: UWB SOA module flat gain in (a) and bias current per SOA for flat gain in (b)

3.2.3 Output power

A challenge in the design of semiconductor optical amplifiers is to increase saturation power and the module output power. In the section 1.9, the trade-off between OSNR and fibre nonlinearities has been discussed and it has been concluded that there is a power at the input of the span which maximizes the performance of the system. This optimum is typically about 0 dBm per channel. For a 50 GHz-spaced C band system, operating at 0 dBm per channel means a total output power of about 19 dBm for a fully loaded system (80-90 channels). For C+L systems, this corresponds to 22 dBm and finally for a UWB system of at least 250 channels, to operate at 24 dBm. Therefore, the output power of the UWB SOA must be extremely high to operate at the fibre optimum.

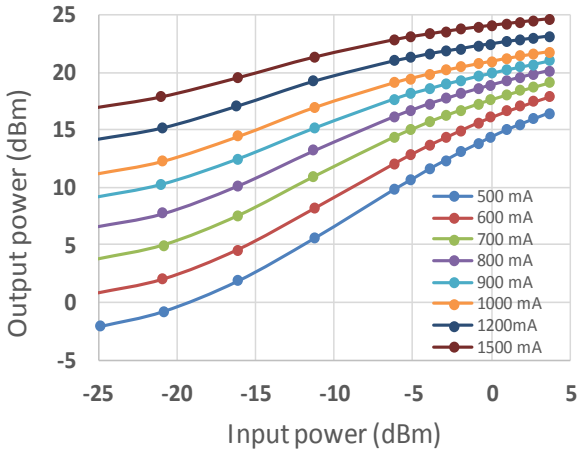

Fig. 3.11: Output power as a function of the input power

In Fig. 3.11, we show the output power of the SOA as a function of the input power for different driven currents. We observe we can overcome easily 20 dBm for driven currents above 1000 mA per SOA. Conventional SOA have difficulties to exhibit output power higher than 15 dBm as showed in chapter 2.

Fig. 2.9 showed that at the operating current of 500 mA the maximum output power is 15 dBm for the state-of-the-art SOA. However, for the novel SOA output powers higher than 20 dBm can be accomplished thanks to its tailored design with polarization diversity. The improvement of the UWB SOA is at least 5-10 dB.

Finally, Fig. 3.12 shows the total output power that we can obtain setting the SOA the flattest possible for a given bias, and then tolerating a positive or negative tilt up to 4 dB. The fact of allowing a slightly tilted gain permits to increase the average gain and therefore the output power. We note that we can set the SOA flat up to 25 dBm, considering a maximum tilt of 4 dB, and we can easily overcome 23 dBm with a bias current higher than 1 A per SOA.

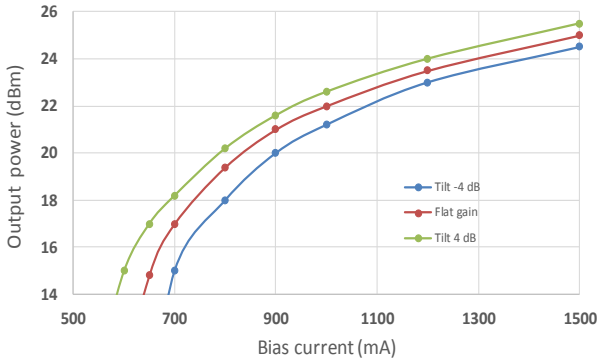

Fig. 3.12: Output power which can be obtained as a function of the bias current with a flat output and with a slightly tilted output up to +/- 4dB

3.2.4 Input saturation power

Input saturation power is the value of input power where the gain of the SOA is compressed by 3 dB. We use this information in system design to have an idea of the input power we must target to operate the SOA in linearly or weakly nonlinear regime, to avoid significant nonlinear distortions on the output signal.

Fig. 3.13-a) shows the gain as a function of the input power for three different wavelengths. It is important to notice the dependence of the input saturation power on the optical wavelength. While the input saturation power at 1530 nm is -3.5 dBm, it is -1.5 dBm at 1545 nm. Finally, it increases up to 7.5 dBm at 1600 nm. This behaviour has already been observed and analysed in chapter 2.

To complement the previous figure, Fig. 3.13-b) shows the input saturation power of the UWB SOA module as a function of the wavelength for 5 different bias currents. We see how it slightly depends on bias current. In fact, it increases when bias current is lower. Another remark is the fact that input saturation power has significantly increased compared with the state-of-the-art SOA. For the novel SOA these values range the interval between -6 and 8 dBm. The state of the art SOA has input saturation power in the range of -18 to -12 dBm (see Fig. 2.9), so the improvement is in the range of 12-15 dB. This has a

huge impact because since these values of input saturation power are required to operate the SOA at the nonlinear threshold (NLT) of the optical fibre.

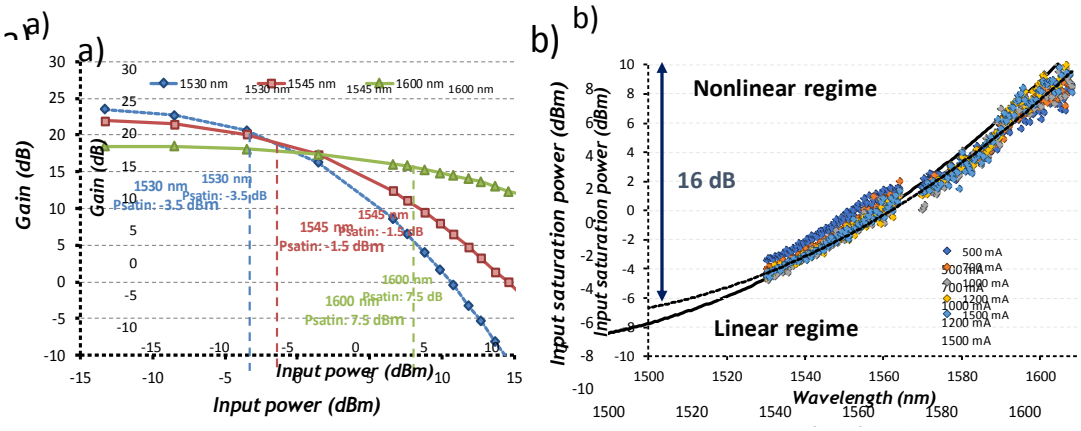

Fig. 3.13: Input saturation power of an UWB SOA module

3.2.5 Relative intensity noise response

The relative intensity noise (RIN) response has also been measured in the UWB SOA module with two different objectives. The first one is to measure the carrier lifetime for this module in order to ensure that the nonlinear regime of the novel UWB SOA has been improved with respect the state-of-the art SOA. The second objective is to double-check if the reservoir model can successfully estimate the dynamic regime for this device.

Fig. 3.14 shows the RIN response for the novel UWB SOA. We have repeated the procedure explained in section 2.7.1-b). For this SOA module, input powers have been ranged from 6 dBm to 18 dBm. The carrier lifetime estimated taking into account the experimental measures is in the range of 700 ps. It is important to remember that for the state-of-the-art SOA this value was estimated in 220 ps. A higher carrier lifetime value implies that the UWB SOA is less sensitive to envelope variations at the output of the signal and therefore the nonlinearities generated by the SOA are expected to be lower.

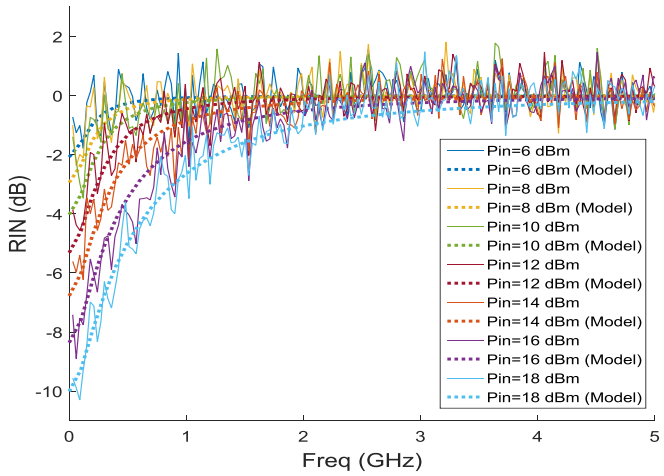

Fig. 3.14: Relative intensity noise response of an UWB SOA

In the same figure (Fig. 3.14), the RIN response obtained with the small signal model has also plotted in dashed lines. We see that the model provides a good estimation of the dynamics of the UWB SOA. The fact that it can successfully estimate the dynamic regime of the UWB SOA is the first step to be done in order to model the performance of an UWB SOA for WDM transmission links.

3.2.6 Noise figure

Noise figure is also an important parameter to be characterized in a SOA module. As depicted in equation *(1.49)*, if we cascade several links of fibre and SOA, every dB of penalty in NF will be translated in one dB of penalty in OSNR. This OSNR degradation will be translated in a reduction of the reach of the overall system.

The procedure followed to measure the noise figure was depicted in chapter 2. In Fig. 3.15 the NF measured for different wavelengths of the novel UWB SOA is shown. Besides, in the same figure, we have plotted the NF of alternative technologies such as the state-of-the-art SOA and a standard EDFA. We observe that NF of conventional SOA present typical values of 9-10 dB whereas the NF of the novel SOA is somewhere in the region of 6 dB when the SOA operates at linear regime. This reduction is due to the fact that coupling losses has been optimized which has allowed us to reduce significantly NF of the module. This is the explanation of the constant value of NF for the whole band. Finally, we compare the UWB SOA NF with the NF of a standard EDFA. We see that it is already at only 1-2 dB to the NF of the last device.

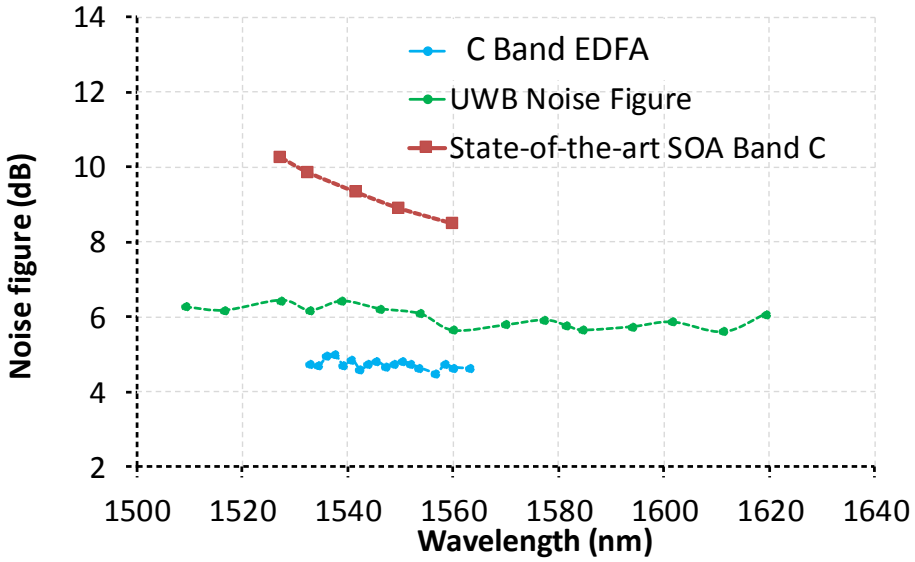

Fig. 3.15: Noise figure of the UWB SOA module compared with a EDFA and a state-of-the art, both in C Band

There is still work to be done in the matter of noise figure reduction, nevertheless this generation of SOA confirms that we are moving in the right

direction in NF reduction of semiconductor optical amplifiers. In [77, 78] a NF below 4 dB has been already achieved by using a Multi-electrode Bulk-SOA

a) Noise figure at flat gain regime

Previous measurements have been done at a low input power in order to ensure precision in NF estimation as discussed in 2.7.1-a). However, at these operating conditions the output spectrum is not flat at all but tilted (Fig. 3.8). Independently of the type of optical amplifier, noise figure increases when the amplifier is saturated. This effect is already discussed in [81] [82] and it is due to the fact that the inversion factor n_{sp} increases in saturation regime due to the fact that the population inversion is not completely accomplished corrupting the OSNR. In system design, we have to take this increase of NF into account because we usually work in a weakly saturated regime in order to find both flat gain and high output power.

Fig. 3.16 shows the noise figure of the UWB SOA as a function of the wavelength when the SOA operates at flat gain regime for every bias current. Address to Fig. 3.10-b) to know the input power for each current. We observe that it has increased from the previous values. Now NF is around 7 dB for the major part of the optical spectrum. It increases to up to 10 dB for shorter wavelengths due to their lower input saturation power. This effect has an impact in the OSNR of the channels located at these wavelengths which will be measured in the transmission experiments presented in chapter 4.

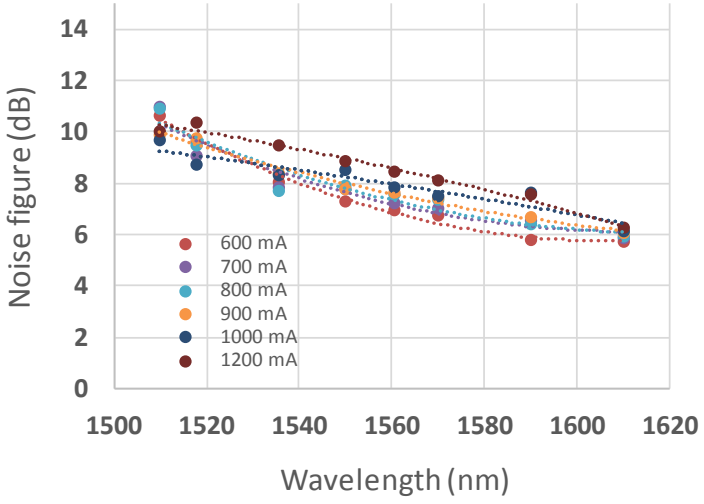

Fig. 3.16: Noise figure of the UWB SOA module

3.3. *SOA Nonlinearities characterization for UWB systems*

3.3.1 Nonlinearities as a function of power

a) For a given input power

We know that if the SOA operates in saturated regime, it implies the addition of nonlinear impairments. We also know that there is not a clear boundary that limits linear regime from nonlinear regime but the change is gradual. That means that performance degradation increases gradually with input power. In this section, we measure experimentally this impact to know in a quantitative way which is the penalty suffered at any given input power.

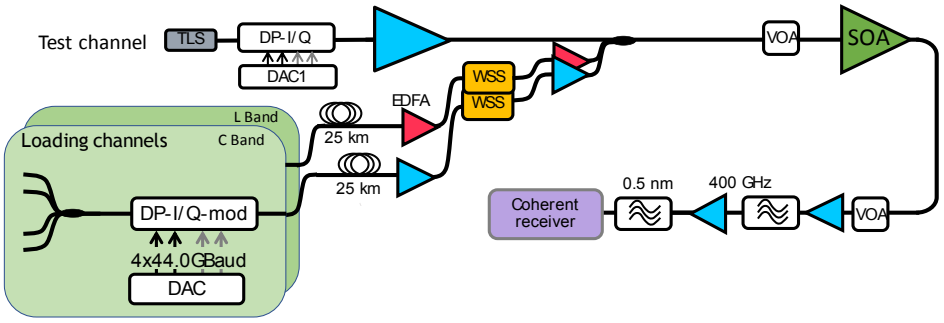

Fig. 3.17: Test-bed for WDM measurements

The test bed used is depicted in Fig. 3.17. A total of 87 C+L loading channels (43 channels per band) have been generated using independent laser sources at 50 GHz spacing modulated by two dual polarization I/Q modulators driven by a dedicated DAC loaded by a randomly-generated sequence of length 36492 symbols at 88 Gsamples/s. A fibre spool of 25 km of standard single mode fibre (SSMF) has been considered in these experiments to decorrelate the channels. Optical EDFA amplifiers have been used to compensate for the modulator insertion losses and the losses of the fibre spool. With two wavelength selective switches (WSS), one per band, we can control the number of channels at their output. In the experiment carried out we consider three different cases of 1, 10 and 87 WDM channels that range the whole spectrum in a uniform distribution inside the SOA. In Fig. 3.18 we show the spectra for the three cases.

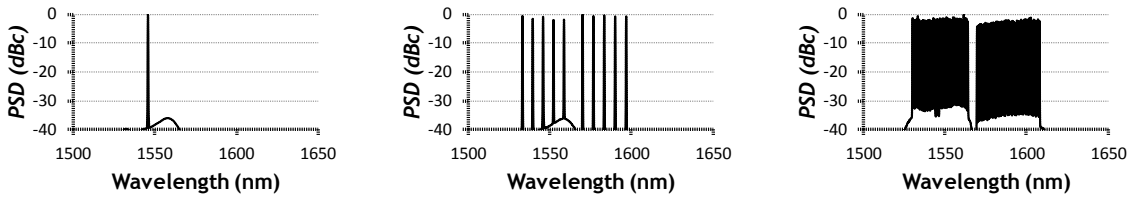

Fig. 3.18: Spectrum of the signal sent to the SOA for 1, 10 and 87 WDM channels

The test channel is generated using an independent dual polarization I/Q modulator driven by a dedicated DAC loaded by random sequences of length 36492 symbols at 88 Gsamples/s. After being amplified with an EDFA, it is coupled with the loading channels. The signal used in all cases is a 32 GBd modulated with either DP-QPSK or DP-16QAM. Pulse shaping was performed using root-raised cosine pulses with roll-off factor equal to 0.01. With a VOA before the SOA we can vary the input power. At the output, the signals go through the back-to-back (B2B) receiver. The module is driven at 1000 mA per SOA. The channel under test is placed at 1545.72 nm where the input saturation power is -1.5 dBm (according to the values of Fig. 3.13).

With this setup, the penalties created by the SOA for every input power with different WDM regimes and different modulation formats are measured. First, we analyse the case of a single-channel modulated with 32 GB DP-QPSK. We have measured several B2B curves after passing the signal through the SOA, each one for a different SOA input power which ranges from -15 dBm to 4 dBm.

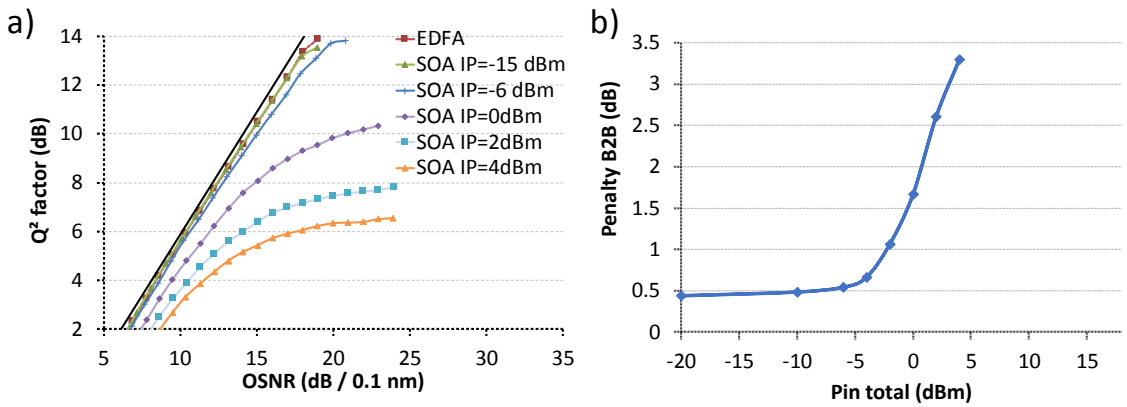

Fig. 3.19: B2B curves for different SOA input powers (IP) compared with theory and with the EDFA reference in (a) and penalty measured at 17 dB of OSNR respect to the theory in (b)

In Fig. 3.19-a) the different curves are plotted together with the theory for 32 GBd DP-QPSK and the EDFA reference. We observe that at lower input powers the B2B curve of the SOA approaches to the EDFA reference. When the input power increases approaching the input saturation power, the B2B curves have penalties due to the addition of SOA nonlinearities. These nonlinearities become more significant in high OSNR regimes where the ASE noise contribution can be neglected.

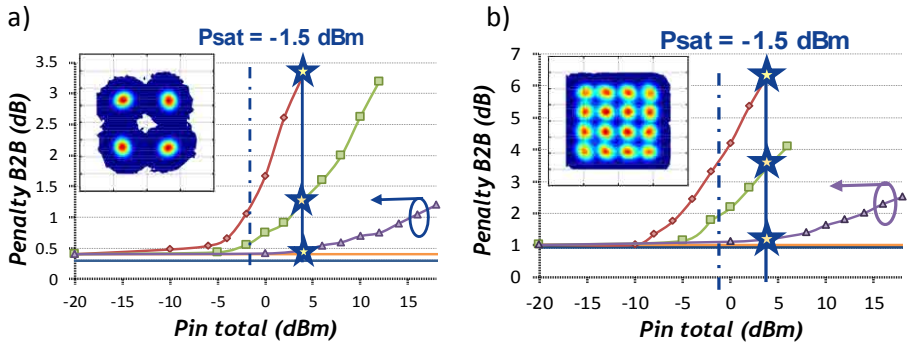

Fig. 3.20: SOA Penalty in back-to-back for different numbers of WDM channels as a function of the input power for PDM-QPSK in (a) and PDM-16QAM in (b)

Fig. 3.19-b) shows the penalty experienced with respect to the theory at an OSNR of 17 dB. We observe that for input powers lower than -5 dBm, the penalty is 0.5 dB. The module SOA operates in linear regime at the input powers and the origin of the penalty is attributed to Tx/Rx impairments. From -5 dBm the penalty starts to increase gradually reaching a value of 1.7 dB for 0 dBm and 3.5 dB for 5 dBm.

Now we analyse the case where several WDM channels are launched into the SOA. We consider the three setups presented in Fig. 3.18 using respectively 1, 10 and 87 channels. Fig. 3.20-a) shows the same curve as in Fig. 3.19-b) but for the three different configurations. Again, the penalty is measured with respect to the theory for an OSNR of 17 dB. We observe that the fact of increasing the number of channels allows us to reduce the penalty for a given total input power. To analyse it let's take as example an input power of 5 dBm. For one channel, the penalty is 3.5 dB as depicted before. Now for 10 channels this penalty is reduced to 1.2 dB and for 87 channels, 0.5 dB (the one associated to Tx/Rx impairments). The fact of increasing the number of channels permits to enter further inside the saturated regime of the SOA without nonlinear impairments. Finally, in Fig. 3.20-a) the decoded constellation is shown for the test channel when 87 channels are transmitted at 5 dBm of total input power.

Finally, Fig. 3.20-b) shows the same figure but for 32 GBd DP-16QAM. Focusing on the case of 87 channels which is the one of our interest, we observe that penalties start being significant again above 5 dBm. That means that input saturation power can be overcome by 5 dB-6 dB with a tolerable penalty caused by SOA nonlinearities (remember that the input saturation power at 1545.72 nm is -1.5 dBm) for both modulation formats DP-QPSK and DP-16QAM. Despite the fact that the nonlinear threshold is the same for both cases, the sensitivity is higher in DP-16QAM. Let's take the penalty of one channel at 5 dBm input power. For DP-QPSK, it is 3.5 dB while for DP-16QAM it increases up to 6 dB.

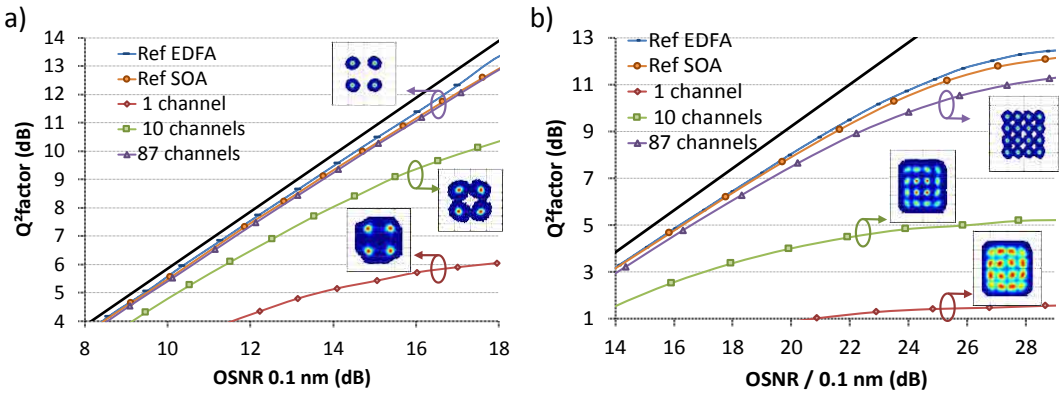

Fig. 3.21: B2B characterization at 4dBm of input power for PDM-QPSK in (a) and PDM-16QAM in (b)

In Fig. 3.21-a) and Fig. 3.21-b), the B2B characterization curves for the three previous spectra at 5 dBm are represented for DP-QPSK and DP-16QAM respectively. Notice that 87 channels can be transmitted through the SOA without penalty for DP-QPSK and with a slightly penalty for DP-16QAM.

Finally, Fig. 3.22 shows the histogram of the received symbols. We can notice that the constellation fits better with the Gaussian distribution when transmitting 87 channels. That's positive from the point of view of channel coding because FEC codes works more efficiently if the received symbols follow a Gaussian distribution.

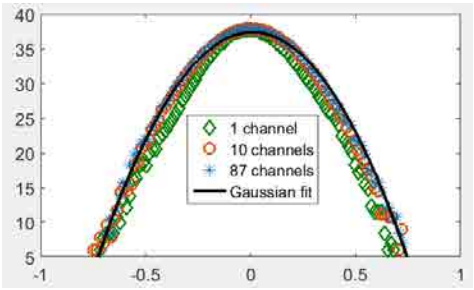

Fig. 3.22: Histogram of the received symbols

b) For a given channel power

In previous section we have measured the penalty of the SOA as a function of its input power. Fig. 3.20 shows a summary of this penalty for different WDM conditions. We have concluded that spreading the power over a large number of channels permitted to increase the tolerance of the saturation regime of the SOA. However, in a UWB system what is usually fixed is the launched power at the input of the optical fibre. As explained before, optical fibre generates nonlinearities at high input power which sets a nonlinear threshold (NLT). This means that the output power of the SOA is generally imposed. In this section we analyse the performance when this power is the constraint. The test bed is depicted in Fig. 3.23. It consists of the same transmitter as the one shown in Fig. 3.17 followed by a span of 100 km of

standard single mode fibre (SSMF). Then we place the SOA which is in charge of compensating the losses of the span. Since the SSMF has a loss of 0.2dB/km, this value is 20 dB. Finally, in the receiver we measure the B2B curve.

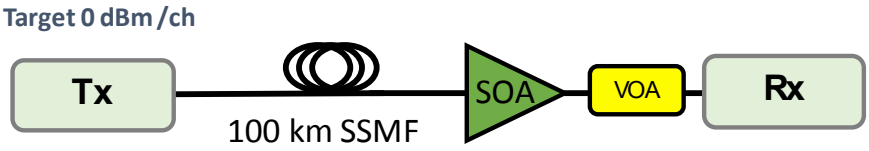

Fig. 3.23: Test bed considered to measure SOA nonlinearities after a span fibre+SOA

Fig. 3.24 shows a table where the 3 different WDM cases under test are explained. We establish the NLT of the fibre to 0 dBm/ch which is a reasonable value for this type of span. The first case under test is a single-channel one. It means that the input power is 0 dBm. At the input of the SOA is -20 dBm since the span has a loss of 20 dB. If we want to leave the SOA with flat spectrum, the driven current at which we should bias the SOA is 600 mA (see Fig. 3.10). With these conditions, we can set the SOA at 0 dBm. This makes sense since in a multi-span link the SOA would be followed by a second span so the output power should be again the NLT.

Channels	Fibre input power	Input power SOA	SOA current	Output power SOA
1	0 dBm	-20 dBm	600 mA	0 dBm
10	10 dBm	-10 dBm	800 mA	10 dBm
178	23 dBm	3 dBm	1200 mA	>22 dBm

Fig. 3.24: Table of considered cases

The second case is now a 10-channel WDM transmission. We have selected 0 dBm/channel again which means 10 dBm of total power at the input of the optical span. At the output, it is -10 dBm (20 dB of span losses). In order to recover the 10 dBm at the output, the module SOA is biased at 800 mA per SOA. In this case the output power spectral density is little tilted in the positive sense due to the fact that the driven current has been pushed to increase output power till 10 dBm. Finally last case is an UWB system of 178 channels at 0 dBm/channel, which gives a total power of ~23 dBm. At these conditions, the input power of the SOA is 3 dBm and we have to fix a bias current of 1200 mA to get at least 22 dBm. The output spectrum is also tilted by 4 dB.

For the three setups, the B2B curves are plotted as a function of the OSNR. Fig. 3.25-a) shows the results for DP-QPSK and Fig. 3.25-b) for PDM-16QAM. As previously measurements, the theoretical curve and the EDFA

reference are also plotted to compare the obtained results. We see how the penalty begins to be noticeable when the number of channels increases specifically at high OSNR values while it is negligible for single channel transmissions.

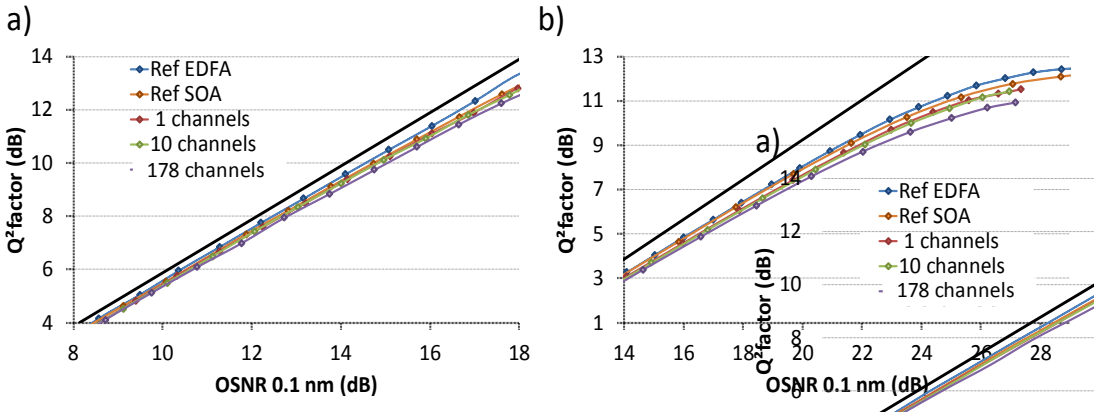

Fig. 3.25: B2B curves for the three considered setups with DP-QPSK in (a) and DP-16QAM in (b)

This experiment leads us to reach several conclusions. The first one is that a SOA system with a low number of channels is feasible in terms of system design. This is a good conclusion for new optical systems which sometimes are not completely full in the first years of operation and number of channels is increased afterwards.

The second conclusion is the fact that it is difficult to obtain flat gain and high output power at the same time. When the number of channels increases the gain of the SOA gets saturated. We can push the SOA to compensate this loss of power at the output by either: increase the input power or increase the bias current. If the input power is fixed, we have to increase this last parameter. Increasing the bias current has important consequences. First it tilts the spectrum, but it also affects to input saturation power. Input saturation power decreases at high bias currents and this generates nonlinearities coming from SOA. The overall result is seen in Fig. 3.25. As it can be noticed, when the number of channels is increased a little penalty appears for both constellations. It is difficult to operate the SOA at a power higher than 23 dBm without penalties. In that sense improvements have to be done in next generations of SOA in order to pull the saturation power. These improvements will permit the SOA to operate at high output powers with flat gain and without nonlinearities.

3.3.2 Nonlinearities as a function of the wavelength

In this section, we quantify the nonlinear penalty produced by the SOA when it operates in saturated regime for different wavelengths. As shown in Fig. 3.13, the input saturation power is not constant but it increases at higher wavelengths: while the input saturation power is -5 dBm at 1510 nm, it takes a value above 8 dBm at 1610 nm. It means that the latter wavelength is more tolerant to nonlinearities than the first one.

We did the measurements with the setup presented in Fig. 3.17 but now modulating the test channel with a tuneable laser source (TLS) so we can test different wavelengths. With the WSS we can easily multiplex it with the loading channels. We have transmitted 87 channels along the whole C+L band. Fig. 3.18-c) shows the power spectral density of the transmitted signal. With a VOA the input power to the SOA has been controlled ranging a set of values between -10 dBm to 10 dBm with the aim of operating the SOA in different saturation regimes. The performance in terms of Q²factor and OSNR is measured for the two extremes of the 100-nm bandwidth: 1510 nm and 1610 nm. OSNR can be easily measured with an optical spectrum analyser.

Fig. 3.26-a) and Fig. 3.26-b) show the results at 1610 nm for DP-QPSK and DP-16QAM respectively. In Fig. 3.26-a), OSNR increases with input power as expected but for higher input powers it saturates. This saturation is attributed to the higher NF of the SOA when increasing the input power and the fact that the gain profile becomes tilted which affects the overall OSNR. Q²factors have been estimated from the SNR measured at the output. We observe that it saturates at 20 dB which is the penalty associated to our Tx/Rx. It means that the main limit is the Tx/Rx and SOA nonlinearities are negligible. Same behaviour is measured with 16QAM in Fig. 3.26-b). It has sense since SOA input saturation power is above 8 dBm for this wavelength.

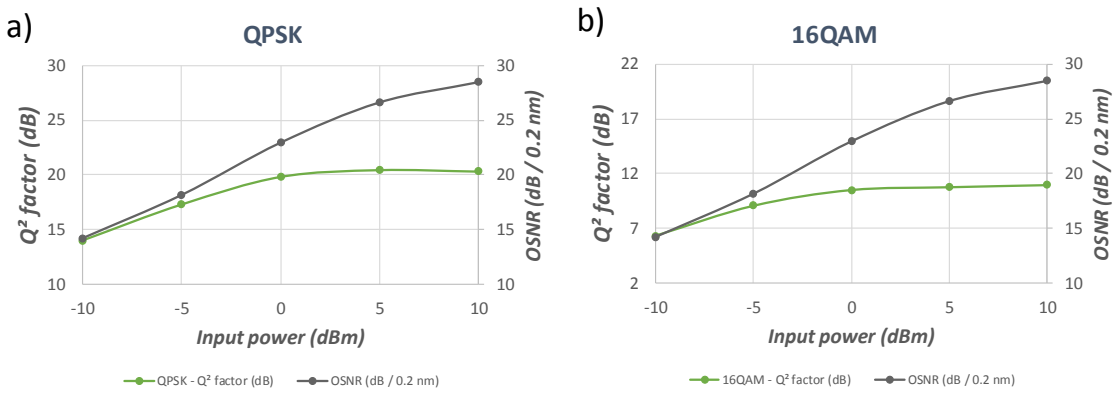

Fig. 3.26: Measurements at 1610 nm for PDM-QPSK in a) and PDM-16QAM in b)

On the other hand, the input saturation power for 1510 nm is -5 dBm, so the behaviour in terms of Q²factor is expected to be different here because SOA saturates earlier in power. Fig. 3.27 shows Q²factor and OSNR for both modulation formats at this wavelength. We observe how Q²factor decreases with high input powers due to the nonlinear impairments which come from the SOA.

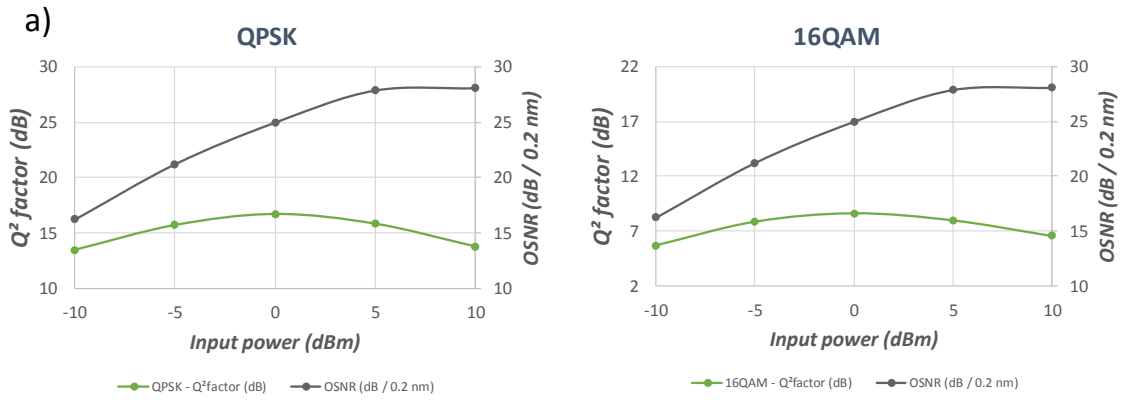

Fig. 3.27: Measurements at 1510 nm for PDM-QPSK in a) and PDM-16QAM in b)

Again, there is a trade-off between OSNR and nonlinearities. For low input powers the performance is limited by ASE noise (observe how the OSNR takes lower values). For high input powers the OSNR increases and the main limitations come from the SOA since it operates at saturated regime. In between there is an optimum value. Fig. 3.27 shows that the optimum input power at 1510 nm is 0 dBm that corresponds at an input saturation power (-5 dBm) + 5 dB. Last experiment leads us to the conclusion that as expected higher wavelengths are more tolerant to SOA nonlinearities than lower ones. In fact, curves shown in Fig. 3.20 for 1545.72 nm can be easily extrapolated for any wavelength if the values of the x axis (input power) are normalized with the corresponding input saturation power.

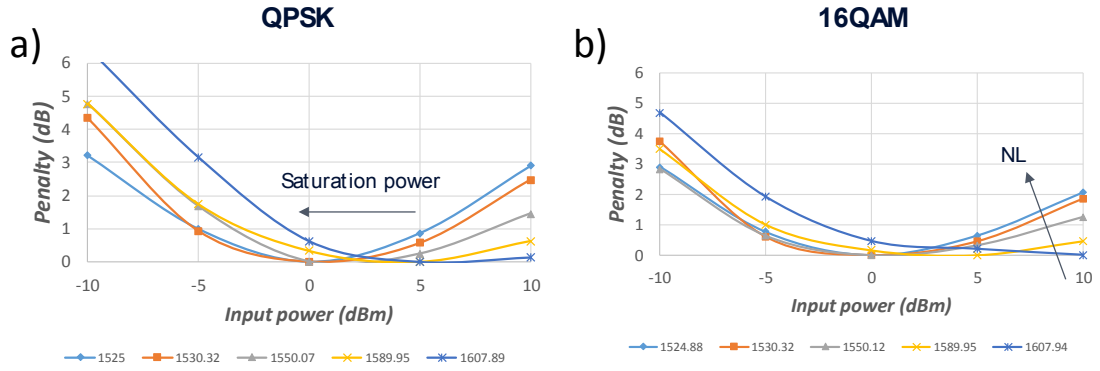

Fig. 3.28: Penalty measured at different wavelength for PDM-QPSK in a) and PDM-16QAM in b)

Finally, to double-check the conclusion reached previously, Fig. 3.28 shows the penalty for different wavelengths distributed along the whole band. Curves as the ones shown in Fig. 3.26 and Fig. 3.27 have been done for every wavelength. Penalty is measured as the Q²factor normalized to the maximum Q²factor measured for each one. We clearly see the effect highlighted before. The saturation power increases with the band as expected.

3.4. *Fibre nonlinearity mitigation for UWB systems*

In an optical transmission system, as discussed in section 1.9, there is the issue concerning the addition of fibre nonlinearities which limits the input power into the optical span and therefore the OSNR. If these nonlinearities could be partially or totally compensated, the fibre nonlinear threshold (NLT) would increase allowing us to transmit at higher OSNR and thus, increasing the potential reach of the system.

In the past, some techniques have been presented in order to mitigate fibre nonlinearities such as digital-back propagation (DBP) or perturbative nonlinear compensation. These techniques take into account the perturbations that the signal suffers through the propagation along the optical fibre and tries to reverse them. These perturbations are modelled by the Schrödinger equation discussed in section 1.5.2. However, when the number of channels is increased the DBP is not as effective since it does not take into account the interchannel effects which become important as long as the bandwidth is increased. If these effects are considered, we talk about multichannel DBP. This extension is quite more effective than the single channel DBP however it suffers from high computational complexity making too complex the implementation in real systems. It is the reason why in this section we focus on the mitigation of fibre induced nonlinearities in the context of ultra-wideband transmission systems.

In recent years, new analytical models such as the Enhanced Gaussian Noise model (EGN) have been proposed in literature [54]. These models predict the existence of an optimum symbol rate in terms of nonlinearities and according to the theory, it seems possible to mitigate partially fibre nonlinearities by transmitting at this optimum symbol rate, what is known as symbol rate optimization (SRO). These models provide a closed formula [79] which depends of the parameters of the system that permits find the proper symbol rate given the length of the spans, the dispersion accumulated and the number of spans. In typical systems, the optimum symbol rate falls in the region between 2 and 10 GBd. The existence of this optimum symbol rate is discussed in [80] [81]. Multicarrier multiplexing is the technique which has become the most popular to exploit this optimum symbol rate is which consists in splitting the signal in different subcarriers each one transmitted at this optimum symbol rate.

Moreover, transmitting signals with different subcarriers at the optimum symbol rate could not only increase the reach of optical systems but also reduce the complexity in the management of Chromatic Dispersion, one of the bottlenecks in the digital signal processing (DSP) for dispersion non-managed links. It is why we have decided to study this technique in the context of UWB systems.

Some experiments have confirmed the analytical model predictions for single-channel transmissions. For instance, in 2012 was successfully increased

the transmission reach in 22% transmitting in QPSK 8 carriers at 3 GBd instead of only one at 24 GBd [75]. However, at that time there was still a lack of confirmation for WDM systems. It is why we planned to make some experiments specifically to see the evolution of the multicarrier benefit when increasing the optical bandwidth. The confirmation of the predictions done by semi-analytical models could be crucial in order to tackle the problem of fibre nonlinearities for ultra-wideband systems.

3.4.1 Multicarrier transmitter and receiver DSP

In this section is presented how these subcarriers are generated in the transmitter and how they are detected in the receiver-side [82].

For single-carrier modulation, symbol sequences are generated using delayed decorrelated sequences and filtered by a root-raised cosine (RRC) filter with a roll-off factor of α. In the case of multicarrier generation, the subcarriers are generated digitally according to Fig. 3.29-a). Symbol sequences are generated using delayed decorrelated sequences which are divided into N streams, where N is the number of desired subcarriers. We have computed the correlation of these sequences to ensure that the correlation peak between adjacent carriers is 30 dB below the power of the signal. The sequences of each subcarrier are filtered by the RRC filter with a roll-off factor of α, up converted in frequency domain to generate the different subcarriers and shifted to their corresponding intermediate frequencies (Subcarrier positioning), before summation and time domain conversion of the overall multicarrier spectrum.

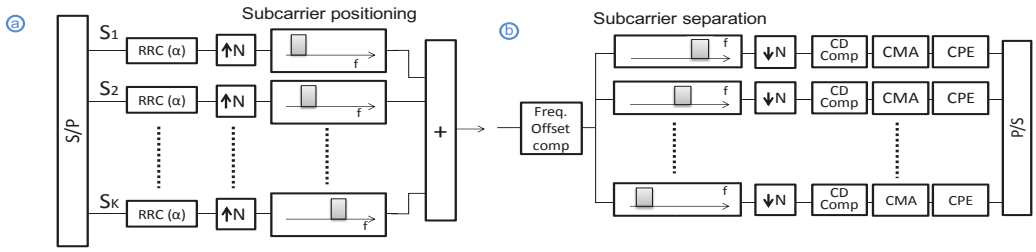

Fig. 3.29: Multicarrier transmitter (a) and receiver DSP (b).

At the receiver side, the sampled signal obtained after a coherent detection were processed to recover the transmitted data as described in Fig. 3.29-b). Frequency offset compensation is performed in the frequency domain before subcarriers separation. Then digital signal processing of each subcarrier includes chromatic dispersion compensation, polarization demultiplexing and carrier phase Estimation (CPE). The length of the CPE algorithm has been optimized for each measurement. Our DSP does not include an 8x8 LMS real-valued butterfly equalizer to compensate the interference between symmetric carriers as suggested in [81] since no significant improvement (<0.1 dB) has been observed in our experiment. Finally, their bit error rates (BER) are computed and subsequently converted into Q^2 factor. In Fig 2.2-b) is shown as example signals generated respectively with one, four and eight subcarriers.

3.4.2 Test bed

a) Terrestrial link

Our terrestrial link experiments have been done using the test bed depicted in Fig. 3.30-a) which consists of eight tuneable laser sources (TLS) with 100 kHz linewidth, including the laser under test at 1545.72 nm, plus fifty six loading Distributed feedback (DFB) lasers. All sixty-four lasers are spaced by 50 GHz as aforementioned. Our eight TLS are separated into odd and even sets and sent to separate PDM I/Q modulator driven by distinct digital-to-analog converters (DAC) operating at 88-GSamples/s. These two sets are then passed into separate low-speed (<10Hz) polarization scramblers (PS) and spectrally combined through an optical coupler. Loading DFB lasers are modulated independently to generate the same format, modulation scheme and symbol rate as our eight TLS channels.

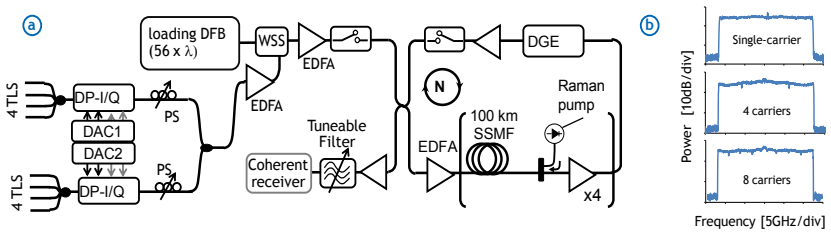

Fig. 3.30: a) Terrestrial link scheme and b) Spectra of the 24 GBd Signals for Single-carrier and Multicarrier (4 and 8 carriers).

After being generated, all channels are recombined using a wavelength selective switch (WSS). The resulting multiplex is boosted through a single stage erbium doped fibre amplifier (EDFA) and sent into the recirculating loop. The loop consists of four 100 km-long spans of SSMF. No dispersion-compensating fibre is used here. Hybrid Raman-EDFA optical repeaters compensates for fibre losses. The Raman pre-amplifier is designed to provide ~10dB on-off gain. Dynamic gain equalization (DGE) is performed thanks to a 50-GHz grid WSS inserted at the end of the loop.

b) Submarine link

Our experiments done in the submarine link have been done with the scheme depicted in Fig. 3.31, which consists of sixty-three loading DFB channels plus one tunable laser source (TLS) with 100 kHz linewidth at 1545.72 nm, being our laser under test. The light from the TLS and that from the loading channels are separately sent to distinct dual polarization I/Q modulators driven by digital-to-analog converters (DAC) operating at 88-GSamples/s, but are identically modulated (same modulation format, symbol rate, Nyquist pulse shaping and modulation scheme).

Loading channels are then passed through one kilometer of standard single mode fibre (SSMF) to ensure decorrelation between channels, before

being recombined with the laser under test using a wavelength selective switch based on 50GHz-spacing grid. This WSS is used to vary the number of WDM channels. The resulting multiplex is boosted through a single stage erbium doped fibre amplifier (EDFA) and sent into the recirculating loop. The loop consists of twelve spans of 55 km of Corning Vascade® EX3000 fibre having in average an attenuation of 0.157dB/km and an effective area of 150μm². No dispersion-compensating fibre is used. EDFA optical repeaters compensate for fibre losses. Dynamic gain equalization (DGE) is performed thanks to a 50-GHz grid WSS inserted at the end of the loop.

At the receiver side, the channel under test at 1545.72 nm is selected by a tunable filter and sent to a coherent receiver comprising a 80GS/s real-time digital oscilloscope having a 33-GHz electrical bandwidth. For each measurement, five different sets of 40 μs are stored. The received samples are processed off-line.

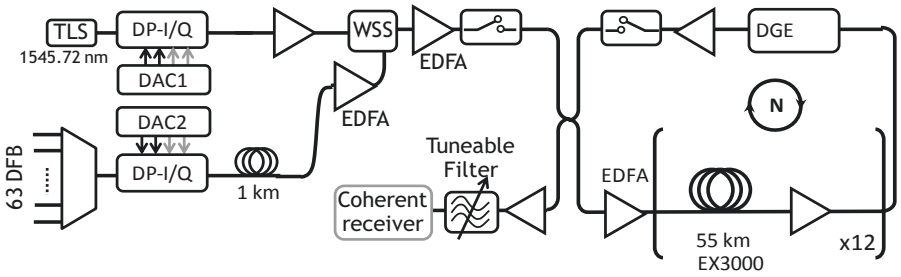

Fig. 3.31: Submarine link scheme

3.4.3 Numerical simulations

We considered different modulation schemes and assessed their nonlinear tolerance in single-channel and WDM transmission systems with 1, 4 and 8 subcarriers and 9 channels. For WDM configuration, we defined the bandwidth efficiency as $\eta = R/\Delta f$ with R being the symbol rate of one WDM channel and Δf being the spacing between channels. In the case of a multicarrier modulation scheme, R corresponds to the total baud rate of all the subcarriers. As schematically described in Fig. 3.32, for multicarrier modulation we consider that the spacing between carriers is equal to their bandwidth, namely R·(1+α)/N, with N being the number of carriers and α a generic roll-off factor. Therefore, the total bandwidth of multicarrier modulated channels is the same as the bandwidth of the single-carrier modulated ones, and they experienced the same WDM bandwidth efficiency.

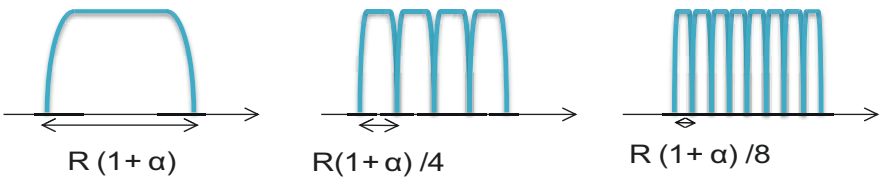

Fig. 3.32: Single-carrier and multicarrier signals for a roll-off factor α and a symbol-rate R.

For the single-channel case, we transmit a 24 GBd signal with, as said previously, 1, 4 and 8 subcarriers. For the WDM systems we define two configurations which are summarized in table I. We used two total symbol rates of 24 GBd and 48 GBd, so considering a constant channel spacing of 50 GHz, the bandwidth efficiency is $\eta = 0.48$ and $\eta = 0.96$ respectively. In both cases, single-channel and WDM, we use a roll-off factor of 0.01 and our sequences have 2^{15} symbols. The wavelength considered for the single-channel system is 1550 nm and this wavelength will be the central channel for the WDM systems. All the laser considered in this study have a linewidth of 100 kHz. The transmitted signals are applied to an uncompensated transmission link made of 100-km long of standard single-mode fibre (SSMF). The dispersion, attenuation and nonlinear index of the fibre are 17 ps/nm/km, 0.2 dB/km and 2.6×10^{-20} m/W respectively and the fibre effective area is 80 μm^2. To compensate the loses in transmission the power profile of the signals along the fibre propagation has been modeled to emulate a Hybrid Raman-EDFA optical amplifier. The power profile of a span is shown in Fig. 3.33. The distance of the configurations has been selected to provide a similar Q^2 factor target in both configurations and is 8,000 and 6,400 km, respectively. Noise is loaded at the end of the transmission line and BER is measured after counting at least 500 errors.

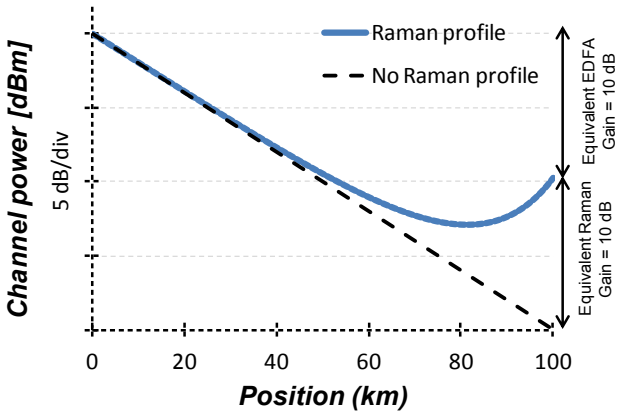

Fig. 3.33: Power profile of the transmission link emulating a Hybrid Raman EDFA amplification system

We first assessed the performance of 24 GBd DP-QPSK signals made of 1, 4 and 8 carriers. Fig. 3.34 shows Q^2 factor versus channel power at the input of each span after 8000 km long transmission. We observe that a single-carrier signal reaches the optimum performance when the launch power per channel is -0.9 dBm. We also see that multicarrier signals obtain the optimum performance when the launch power is 0.4 dBm for 8 subcarriers and -0.1 dBm for 4 carriers, which is 1.2 dB and 0.8 dB higher respectively than in single-carrier. This difference demonstrates higher nonlinear tolerance of multicarrier signals in single-channel transmission which allows the 4-carrier and 8-carrier signals to provide a gain of 0.5 dB and 0.7 dB respectively in the optimum Q^2 factor if we compare them with the single-carrier signal.

Then we assessed the performance of the multicarrier architecture in a WDM system composed of 9 channels as previously mentioned. We used the two

configurations presented in table I to obtain two values of bandwidth efficiency.

TABLE I
CONFIGURATIONS USED IN WDM SIMULATIONS

Parameters	Configuration 1	Configuration 2
Baud rate (GBd)	24	48
Channel Spacing (GHz)	50	50
Bandwidth efficiency (η)	**0.48**	**0.96**
Roll-off factor	0.01	0.01
Bandwidth (GHz)	24.2	48.5
Modulation format	DP - QPSK	DP - QPSK
Distance (km)	8,000	6,400

In configuration 1, 24 GBd DP-QPSK signals made of 1, 4 and 8 carriers are transmitted in a 50 GHz WDM grid. The bandwidth efficiency is thus 0.48. In Fig. 3.35-a) is shown the Q² factor versus channel power at the input of each span after 8000 km long transmission. We observe an optimum launch power for the multicarrier signals of -0.8 dBm for 8 carriers and of -1.3 dBm for 4 carriers, while the one of the single-carrier signal is -1.7 dBm. The improvement in nonlinear tolerance in this case is 0.9 dB and 0.4 dB for 8 and 4 carriers, and the gain has been reduced to 0.4 dB for 8 carriers and 0.2 dB for 4 carriers.

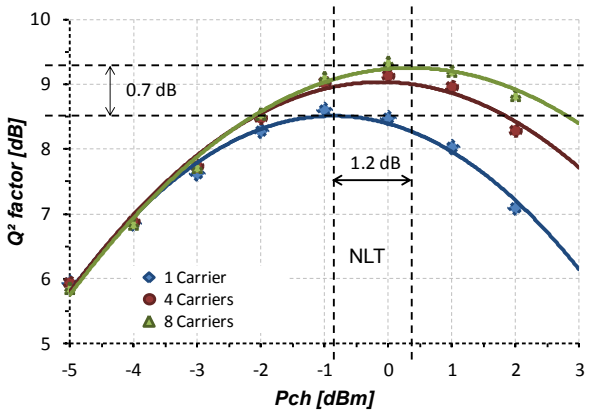

Fig. 3.34: Q²Factor versus launch power after 8000 km for single-carrier, 4-carrier and 8-carrier signals in a single channel transmission

In configuration 2, 48 GBd DP-QPSK signals made of 1, 4 and 8 carriers are transmitted in a 50 GHz WDM grid, which corresponds with a bandwidth efficiency of 0.96. Fig. 3.35-b) shows the Q² factor versus channel power at the input of each span after a reduced distance of 6400 km to obtain similar Q² factors with respect to the symbol rate increase of the signal. We observe the optimum launch power for the multicarrier signals is now about 1.6 dBm and 1.5 dBm for 8 and 4 carriers; while for the single-carrier signal is 1.2 dBm. The improvement in nonlinear tolerance is in this case is 0.4 dB and 0.3 dB respectively and the gain is 0.3 dB for 8 carriers and 0.2 dB for 4 carriers. These results clearly indicate a reduction of nonlinear mitigation provided by splitting high baud rate signals into low baud rate ones when we operate at high spectral efficiency.

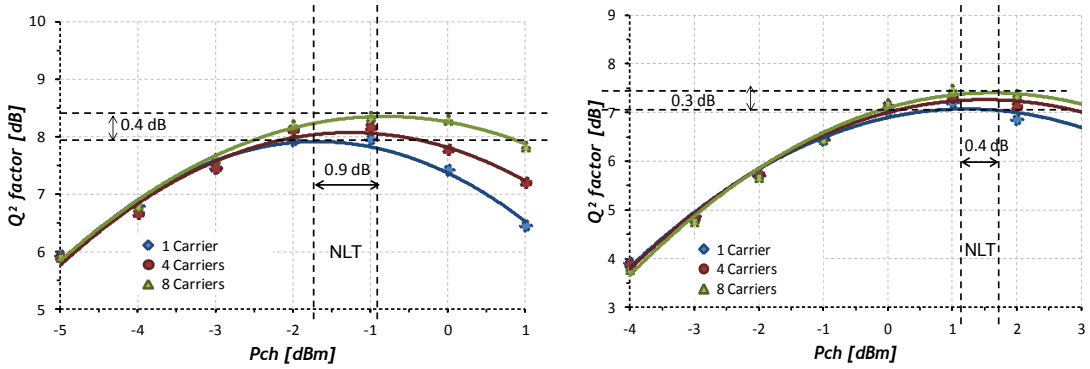

Fig. 3.35: Q²factor versus launch power after 8000 km for single-carrier, 4-carrier and 8-carrier signals with 9 channels for (a) η=0.48 after 8000 km and (b) η=0.96 after 6400 km.

The numerical investigations performed here particularly show that the gain obtained in single-channel is reduced significantly when adding the surrounding channels. It demonstrates the significant impact of these channels on the multicarrier gain. Furthermore, these results indicate that the bandwidth efficiency plays an important role in the benefits of multicarrier modulations. In next section, we carry out an experimental investigation of this effect using a WDM comb composed of sixty-four channels for the two configurations presented in table I.

3.4.4 Experimental results

a) Back-to-back characterization

Fig. 3.36 shows the performance in back-to-back of single-carrier, 4-carrier and 8-carrier configurations with 24 and 48 GBd DP-QPSK data together with theoretical expectations. At both symbol rates, the multicarrier scheme exhibits higher OSNR penalties at Q² factor above 10 dB, which can be attributed to its highest peak-to-average power ratio. At 8 dB Q² factor, the 8-carrier modulation exhibits 0.1dB penalty with respect to single- and 4-carrier at the symbol rate of 24 GBd. When symbol rate is increased to 48 GBd, 4- and 8-carrier modulations exhibit both an OSNR penalty of 0.2 dB with respect to single-carrier

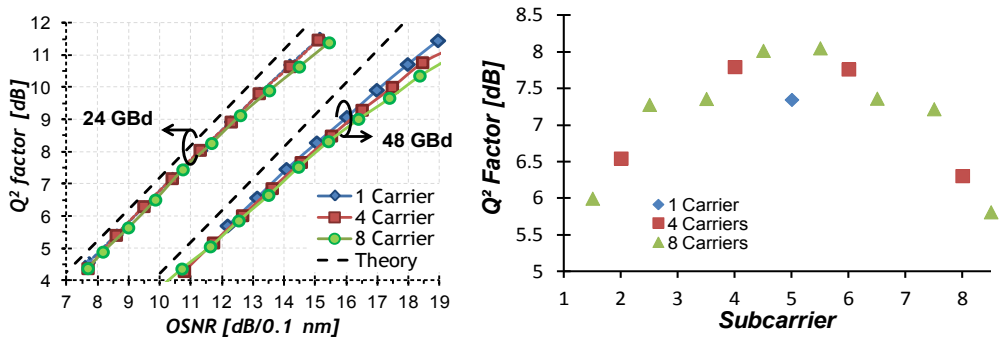

Fig. 3.36: a) Back-to-back characterization at 24 and 48 GBd and b) for 48 GBd the performance per carrier at 14 dB/0.1 nm.

b) Multicarrier signals vs bandwidth efficiency

We considered different modulation schemes and assessed their nonlinear tolerance in single-channel and WDM transmission systems with 1, 4 and 8 subcarriers. For multicarrier modulation we consider that the spacing between carriers is equal to their bandwidth, namely R*(1+α)/N, with N being the number of carriers and α a generic roll-off factor. Therefore, the total bandwidth of multicarrier modulated channels is the same as the bandwidth of the single-carrier modulated ones, and they experienced the same WDM bandwidth efficiency.

Next, we investigated the tolerance to nonlinear impairments of single-carrier and multicarrier systems depending on the bandwidth efficiency using our terrestrial recirculating loop described previously. First, we measured their performance at a symbol rate of 24 GBd, leading to a bandwidth efficiency of 0.48. Fig. 3.37-a) shows the evolution of the Q² factor as a function of channel launch power after 20 loop round-trips, corresponding to 8000 km. In this figure, we can observe that, contrary to the numerical case, the 4-carrier signal slightly outperforms the 8-carrier one. Nevertheless, they exhibit almost the same optimum channel power around -1.7 dBm, which is 0.8 dB higher than the single-carrier one. The performance at this optimum power is 7.4 dB for single-carrier, 7.8 dB for 4-carrier and 7.6 dB for 8-carrier. These results indicate that the multicarrier signals outperform the single-carrier by 0.4 dB and 0.2 dB respectively for 4-carrier and 8-carrier. It also shows that the best results are obtained using 4-carrier that corresponds with a baud rate equal to 6 GBd per carrier. The 0.4 dB performance improvement would be translated into 8% reach increase with respect to single-carrier systems.

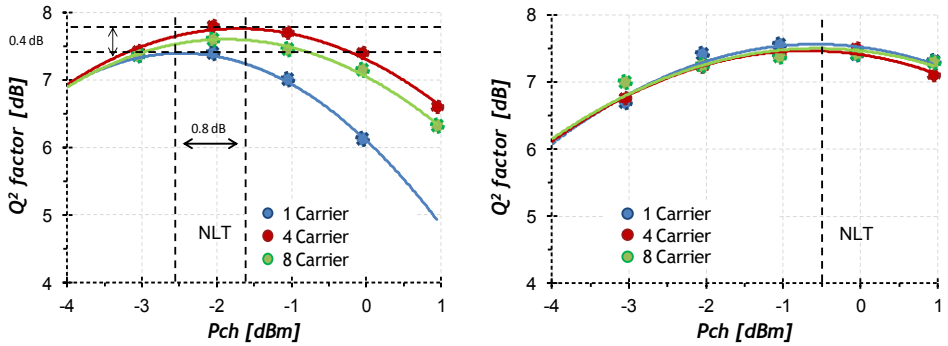

Fig. 3.37: Q²factor versus launch power for single-carrier, 4-carrier and 8-carrier signals. In a) after 8000 km and η=0.48 and b) after 6400 km km and η=0.96.

Then, we modulated all 50-GHz spaced channels with the symbol rate of 48 GBd, thus doubling the bandwidth efficiency of the system at 0.96. Fig. 3.37-b) shows the performance of the single-carrier, 4-carrier and 8-carrier signals versus launch channel power at the transmission distance of 6400 km, which corresponds to 16 loops. We observe in this figure that all the signals exhibit similar tolerance to nonlinear impairments and the same optimum channel power of -0.6 dBm. Contrary to the previous experiment, the three

configurations show nearly identical Q² factor around 7.5 dB in the optimum power.

So with this experiment we observe that the multicarrier signals has better tolerance to nonlinearities however this gain obtained depends on the bandwidth efficiency. When this parameter increases we shown that the gain is reduced significantly

c) Multicarrier signals vs number of channels

Next, we investigated the dependency of the performance of single, 4-carrier and 8-carrier signals with the optical WDM bandwidth with a 48 GBd QPSK signal at 0.96 of bandwidth efficiency. In this experiment, we use the submarine loop where the number of loop round trips is set to twenty-two, corresponding to a transmission distance of 14,520 km. We first measure the performance evolution of the three modulation schemes in the configuration with 64 channels, while varying the total launch power from 13 to 19 dBm. Then we repeated the experiment after reducing subsequently the number of WDM channels to 48, 32 and 16 as it can be shown in Fig. 3.39-a). Fig. 3.38-a) and Fig. 3.38-b) show examples of the measured performance in the configurations with 64 and 32 channels.

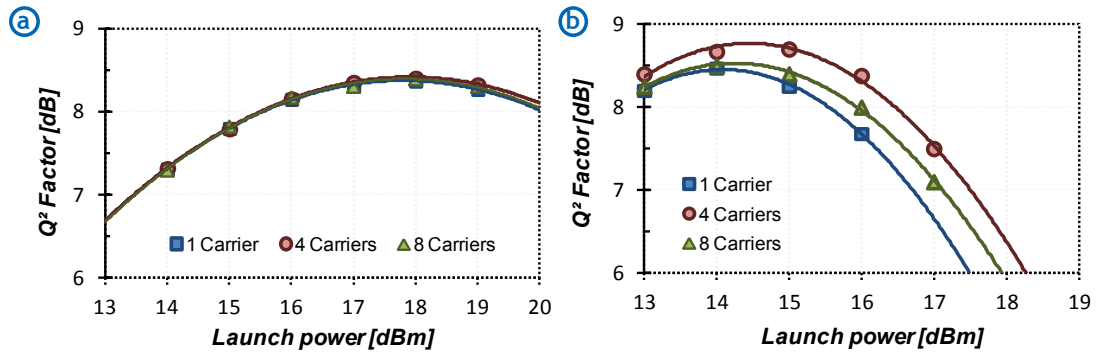

Fig. 3.38: Experimental results with a) 64 channels and b) 32 channels

As it can be seen, although the performance of single carrier modulation is unchanged, the performance of the multicarrier modulation is improved when reducing the number of channels, particularly in the case of 4-carrier here, corresponding to 12 GBd. Finally, we plotted in Fig. 3.39-b) the gain of multicarrier versus single carrier as the difference between the optimum performance of the best number of subcarriers and the optimum one of single carrier. The results clearly show that the maximum gain of 0.4 dB is obtained with 16 channels only. However, one can observe a clear decrease of the gain when the number of channels is increased, leading to much reduced benefit with up to 64 channels. This result, obtained at a high bandwidth efficiency of 0.96, indicates a dependency of nonlinear tolerance of MC systems versus WDM bandwidth.

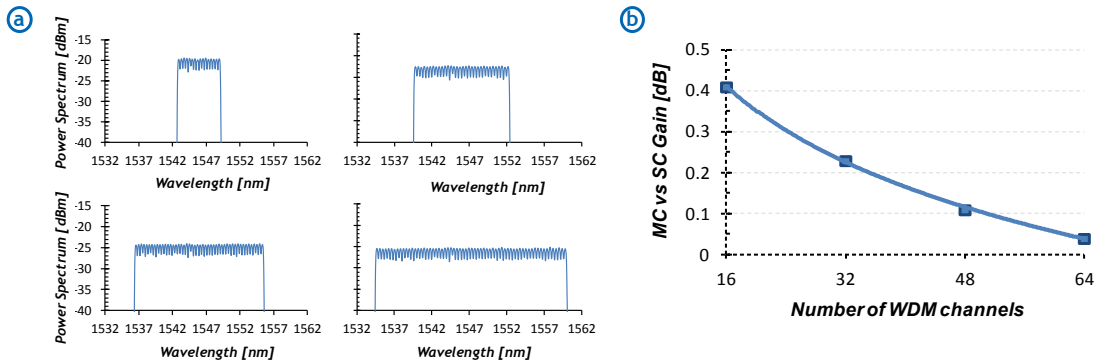

Fig. 3.39: a) Spectra of WDM comb with 16, 32, 48 and 64 50GHz-spaced channels and b) Measured gain of multicarrier versus single carrier transmission as a function of the optical WDM bandwidth.

3.5. *Conclusions*

In this third chapter, an UWB SOA has been presented and characterized. For this novel device, a polarization diversity structure has been selected with the purpose of both, increasing output saturation power and minimizing noise figure with respect to state-of-the-art SOA introduced in previous chapter.

The resulting SOA has a high gain of 20 dB in a bandwidth of at least 100 nm. Saturation power has significantly increased allowing the SOA to operate with higher output powers. Coupling losses has been reduced reaching values of NF down to 6 dB.

Then the module has been characterized experimentally to quantize the penalty introduced when it operates in different regimes in different WDM conditions. We have obtained the measure of penalty as a function of input power for one wavelength and we have seen that it can be generalized for any given wavelengths taking into account the concept of input saturation power. We have assessed that for DP-QPSK and DP-16QAM, the input saturation power can be overcome by 5 dB without significant penalty. This is a very positive conclusion since it permits to consider for the first time this novel UWB SOA capable for WDM transmission purposes and it becomes a huge alternative to EDFA for becoming the next generation optical amplifier.

On the other hand, due to the fact that what really matters is output power, some progress is expected in coming years in the chip design to further increase the output saturation power of the SOA module or in the matter of noise figure reduction. One of these new possibilities is using SOA with different lengths or a Multi-electrode structure. The use of this last structure could improve significantly the features of this novel SOA in terms of gain flatness and noise figure and which would approach even more the performance to EDFA.

Finally, we have studied the matter of fibre nonlinear compensation for UWB systems. Current technologies used for nonlinear mitigation have been

demonstrated to be less effective when a large bandwidth system is studied. So a new modulation scheme has been proposed in literature in order to optimize the symbol rate of the signal to reach an optimum from the point of view of fibre nonlinearities: the multicarrier multiplexing. Analytical models claimed that the benefit of this approach can be considered in UWB systems. However, our experiments and numerical simulations did not show the same tendency. We attribute this difference to the fact that analytical model cannot consider all the possible effects: Tx/Rx limitations, or the problems for a standard CPE algorithm to remove nonlinear phase noise as explained in [87] [88]... Advanced joint-subcarrier CPE algorithms are currently being investigated [90] which can help in the removal of nonlinear phase noise. On the other hand, experiments in laboratory have also some practical limitations. For instance, the incapability of independently modulating all the loading channels. To solve this issue, experiments should be done in a real system with completely independent channels. However, it will be difficult to carry out since we have seen that the gain of this approach is not high enough to pull the implementation of this approach in next generation transponders. In fact, all the experiments done are in line with the fact that multicarrier gain is clearly reduced for advance modulation formats that are the ones used in this type of high spectral efficiency systems. Furthermore, studies done in parallel even neglect the gain for Gaussian modulation formats [82]. In next chapter probabilistic shaped modulation formats are used in order to approach to the Shannon capacity limit at high spectral efficiency, therefore digital multicarrier will not be used in our UWB experiments because it would not provide any benefit for this modulation format.

Chapter 4. 100 nm continuous band experiments for DCI applications

In this chapter, we show an experimental demonstration of the novel UWB SOA capabilities for data-centre-interconnect (DCI) applications. This type of network is a good option to begin with simply because the number of spans tends to be limited so the number of amplifiers required is not extremely large. Furthermore, its traffic data has exploded in the last years, so they require a constant increase of capacity of their systems. In recent years, the number of users of this social network has multiplied by 20 [83]. Fig. 4.1 shows the traffic machine to user and machine to machine. Although the traffic machine to user has scarcely changed, the traffic machine to machine has grown exponentially. An important percentage of this growth is due to the increment of traffic between data centres. UWB amplification might be a good solution to improve significantly the data throughput of this type of networks without the necessity of deploying new optical links.

We have demonstrated the first 100-nm continuous band transmission though 100 km of EX2000 fibre to show the potential of the novel UWB SOA to become the next generation optical amplifier. But first we have had to generate such a wide band signal. It is important to do the measurements with a large band signal to really study all the additional effects in UWB systems such as the Stimulated Raman Scattering of the optical fibre. Finally, we have tested the stability of the UWB SOA with a 24 hours soak test transmitting real time date between two POP deployed by Facebook in Paris area.

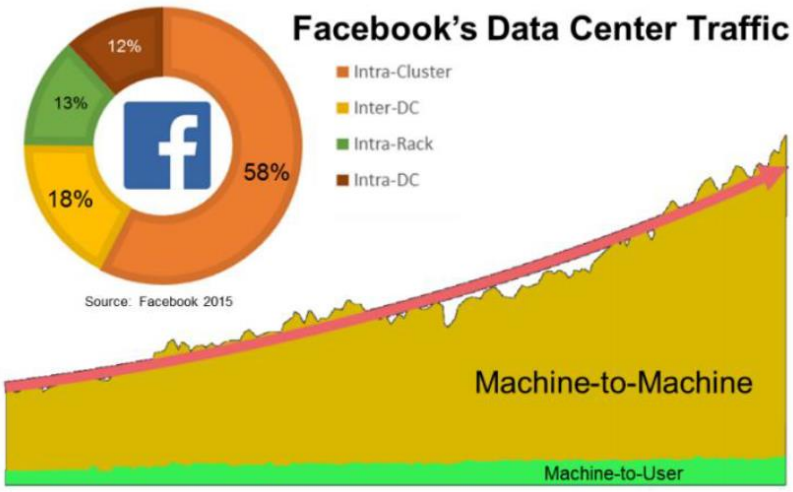

Fig. 4.1: Facebook's Data Centre traffic (from https://research.fb.com/)

4.1. *100-nm continuous band signal generation*

To assess the performance of a real UWB system, a signal of at least 100 nm must be generated to really study all the effects associated to the transmission of such a wide band signal. For instance, the stimulated Raman scattering of the optical fibre is not negligible anymore tilting the whole spectrum and varying thus the conditions of the transmission system. But generating this signal is not straightforward since available commercial products in S Band are generally scarce. To solve this issue, we have decided to use the ASE Noise generated by several stages UWB SOA to simulate the transmission of channels at this part of the spectrum.

The test bed to generate this signal is depicted in Fig. 4.2. In C and L bands, 86 and 92 laser sources, at 50GHz spacing, are separately modulated with distinct dual polarization I/Q modulators, each modulator being driven by a dedicated digital-to-analog convertor (DAC) loaded with different randomly-generated sequences and operating at 88 GS/s. Modulated light is amplified through C- and L-band amplifiers respectively to compensate for modulation insertion losses. Fibre spools of 25-km long are used to decorrelate loading channels. Owing to the lack of laser sources in the upper part of S band (1508 to 1530 nm) as well as in the transition interval between C and L bands (1564 to 1569 nm), we combined ASE noise to the sets of C-band and L-band channels through different input ports of a home-made LCOS based ultra-wideband wavelength selective switch (WSS), having 250 slots spaced by 50GHz ranging from 1507.63 to 1608.33 nm. The WSS exhibits an average insertion loss of 5.5 dB. The generated 100-nm wide optical spectrum is then coupled to the channel under test which is made of a tuneable laser source (TLS) modulated with a dual polarization I/Q modulator (DP I/Q) driven by a dedicated DAC fed with a randomly-generated sequence of length 36492 symbols. The channel under test as well as loading channels are modulated with 49 GBd probabilistic constellation shaping (PCS) of 64-ary quadrature

amplitude modulation (64-QAM) having a source entropy of 5.41. Pulse shaping was performed using root-raised cosine pulses with roll-off 0.01.

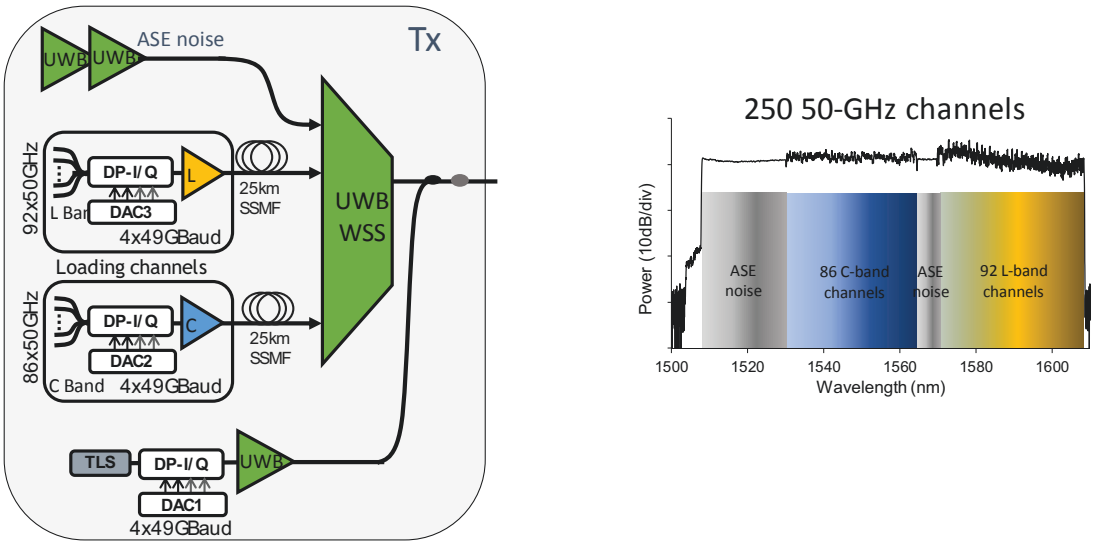

Fig. 4.2: Test-bed for generating the 100-nm continuous band signal (a) and spectrum of the generated signal (b)

4.2. *Stimulated Raman scattering (SRS) experimental characterization*

In this section, we measure the impact of stimulated Raman scattering (SRS) in UWB systems. As it has been discussed in chapter 1, SRS is an inelastic nonlinear effect of optical fibres that consists in the transfer of energy from shorter wavelengths to the longer ones. It can even be considered as a positive effect since it is used to obtain the gain of backward Raman optical amplifiers, but at the same time SRS is negative for WDM systems since this transfer of energy tilts the optical spectrum at the output of the optical fibre.

Until now this effect for WDM systems was well known for amplification techniques, but it was no significant in conventional C-band systems with a bandwidth much below 100 nm. Moving to UWB systems changes the paradigm and this effect is not negligible anymore for two main reasons: first, if the bandwidth is tripled, we should have to triple the total power of the signal if we want to keep the same power per channel and the fact of triple the input power means to cross the SRS threshold. And second, moving to a higher bandwidth magnifies the tilt between the first and the last channel.

The fact of generating a 100-nm continuous band permits us to measure for the first time the SRS tilt in a WDM system in such a wide spectrum. We have measured the power spectral density at the input and at the output of a span of 100 km of standard single mode fibre (SSMF) for different input powers with an optical spectrum analyser and we have computed the SRS tilt from these two measures. Fig. 4.3 shows the resulting curves for different input

powers which ranges from 10 dBm to 24 dBm. Firstly, we observe that at 10 dBm input power the spectrum is not tilted indicating we are still in linear regime of the fibre. When the input power is increased, we observe how the energy begins to gradually be transferred from the lower wavelengths to upper ones. Finally, when input power is 24 dBm (~0 dBm/ch) it reaches a value of 4-5 dB of tilt.

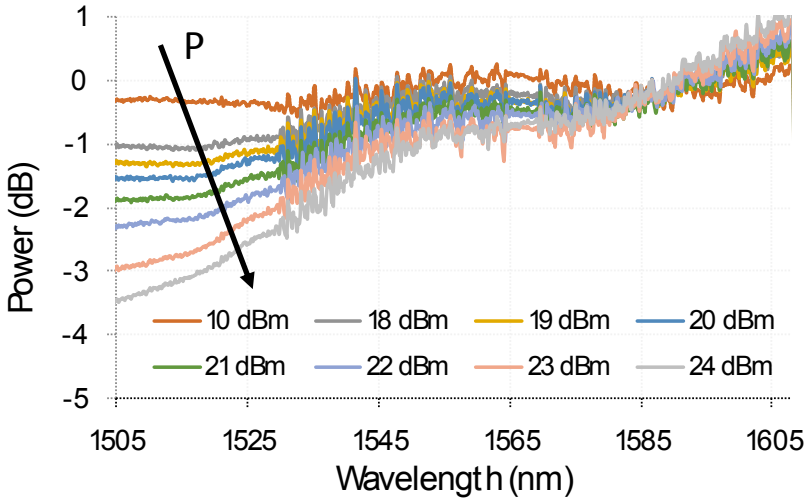

Fig. 4.3: Raman tilt for 100 km of SSMF at different input powers for a 100-nm continuous band signal

SRS also depends on the power density, which vary with the effective area of the optical fibre used. Fibres with larger effective area have less SRS effect and therefore a lower tilt in the spectrum. Fig. 4.4 shows the SRS tilt after 100 km of like Corning's Vascade® EX2000 which is a pure-silica core fibre (PSCF) with affective area of 110 μm^2, compared with the results obtained with SSMF (80 μm^2), both at 24 dBm input power. Pure-silica core fibres have been optimized to reduce the fibre losses and the nonlinear effects. It can be clearly noted in this figure. We observe that the tilt of EX2000 is 1-2 dB lower than in SSMF.

It has an important consequence in the design of a gain flattening filter (GFF). A gain flattening filter is a passive component whose aim consists in attenuating adequately the different wavelengths in order to have at its output a flat spectrum. The fact that the SRS changes with the type of the fibre and the input power makes essential the design of different GFF according to these characteristics.

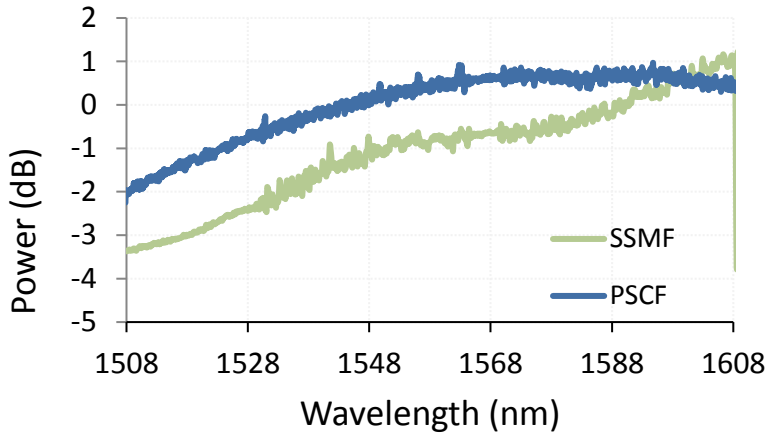

Fig. 4.4: Raman tilt for 100 km of SSMF (80 μm²) and EX2000 (80 μm²), at 24 dBm of fibre input power

4.3. *115 Tbps DCI experimental set up*

Once the 100-nm signal is generated, we have deployed a test bed adequate to simulate a DCI system. The test-bed used is shown in Fig. 4.5. The generated 100-nm wide optical spectrum is coupled to the channel under test which is made of a tuneable laser source (TLS) modulated with a dual polarization I/Q modulator (DP I/Q) driven by a dedicated DAC fed with a randomly-generated sequence of length 36492 symbols. Pulse shaping was performed using root-raised cosine pulses with roll-off 0.01. The 100-nm wide optical signal, covering 250 slots of 50GHz, which is shown in Fig. 4.2-b), is then sent into a first ultra-wideband amplifier (UWB1) and launched into the optical link. The UWB1 amplifier is designed to have a slightly smaller gain than the second one used at the end of the line so that to accommodate with the 9dBm input power. The link is composed of 100 km of pure silica core fibre with an effective area of 110 μm². At the end of the link, the second ultra-wideband amplifier (UWB2) is used to compensate for span losses. The losses experienced by shortest wavelengths are about 2dB higher than those of longest ones, which is mainly due to the stimulated Raman scattering (SRS) effect occurring on such a wide optical signal. Both UWB amplifiers are operated at 1.2A to set the output power at 22dBm to maximize system performance.

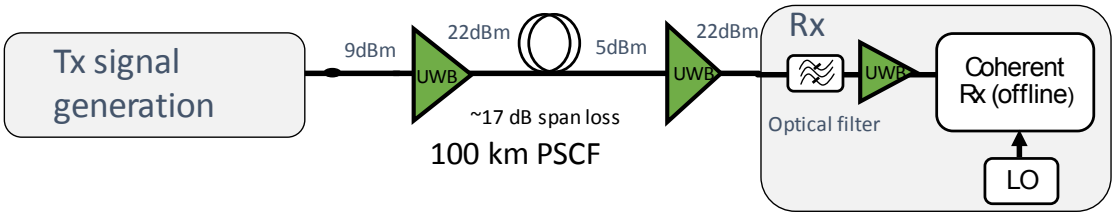

Fig. 4.5: Test-bed for the 100-nm continuous band transmission

In the absence of neither dynamic nor static gain equalization at the time this experiment took place, we chose to operate the first amplifier UWB1 in a

pre-equalization mode by introducing 2-dB higher power level on shortest wavelengths, to manage optical spectrum flatness at the span output.

After the second amplifier UWB2, the signal is sent to a tuneable optical filter to select the channel under test, which is then pre-amplified by a last UWB amplifier before the coherent receiver, including a coherent mixer, a tuneable local oscillator, balanced photodiodes and a 33GHz bandwidth high speed sampling scope operating at 80 GS/s. Signal processing is performed as in [19] to compute SNR and the generalized mutual information (corrected for pilot overheads), before applying multi-rate spatially coupled low-density parity check (SC-LDPC) FEC decoding.

4.3.1 Fibre nonlinearities characterization

To find the operating point from the point of view of the optical fibre, we have deployed the transmission setup but using EDFA amplification. Like this we only have nonlinear effects which come from the fibre. We have changed the input power to the fibre to find the NLT. To simplify the test bed we have only used C band EDFA. We can consider that the NLT is the same for the whole band. In Fig. 4.6, it is shown the SNR measured at the receiver for a reference signal at 44 GBd modulated with PDM-16QAM for two different wavelengths as a function of the fibre input power.

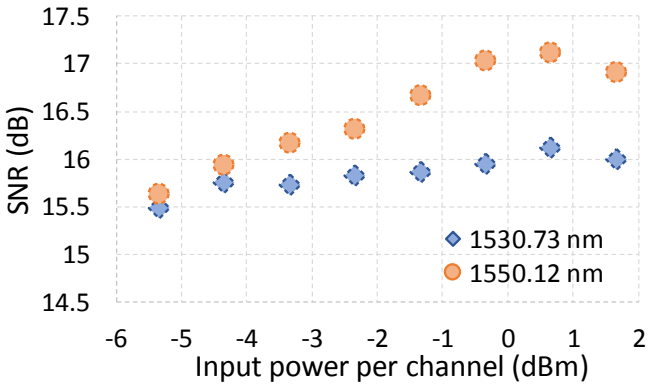

Fig. 4.6: SNR measured with EDFA for different input powers

We observe that the optimum input power, from the point of view of the optical fibre is between 0 and 1 dBm per channel. If we consider 250 channels it means a total input power of at least 24 dBm. Here we can see why is important a UWB SOA with high output power. This first generation of SOA can deliver at 24 dBm but we have preferred to operate at 23 dBm to avoid the important nonlinearities coming from the SOA as we have measured in previous chapter.

4.3.2 Baud rate and modulation format optimization

To choose the adequate modulation format for the transmission experiment firstly we compare the performance of the different options in order

to select the one that offers higher generalized mutual information (GMI). That means the modulation format that maximizes the transmission of useful data for a SNR given. Fig. 4.7 shows the evolution of GMI as a function of the SNR measured for 64QAM, 64 APSK, PS64QAM, 32 QAM and finally 16 QAM. We note that for every SNR there is a modulation format that maximizes the GMI. For high SNR values with total absence of noise, the modulation format with more symbols (64QAM and 64APSK) obviously becomes the most efficient one. However, if the channel is corrupted by additive white Gaussian noise (AWGN), as we have discussed in first chapter, modulation formats which are more similar to a Gaussian constellation tend to become more efficient in terms of GMI [8]. It is why PCS-64QAM dominates for SNR values below 17 dB. As a consequence, we have decided to use this modulation format in our experiment because for the expected SNR around 15 dB, PSC64QAM is the modulation format which presents the closest to the Shannon limit between the considered formats.

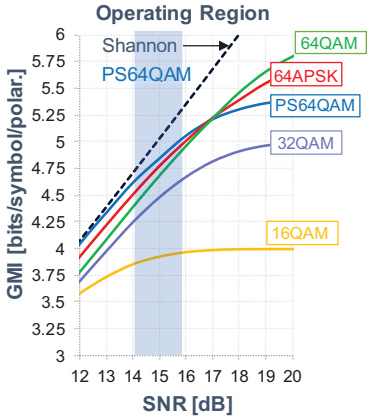

Fig. 4.7: GMI different constellations as a function of the SNR

Several symbol rates between 44 and 49.5 Gbd in a 50 GHz-grid have been considered with the purpose of optimizing the channel bit rate. We observe that at a constant spectral efficiency the channel bit rate depends linearly of the bandwidth. However, for higher symbol rates some degradation is expected due to cross talk between channels or filtering effects which might penalize the spectral efficiency. Therefore, there is a trade-off between these two effects which generates in the middle an optimum transmitting symbol rate.

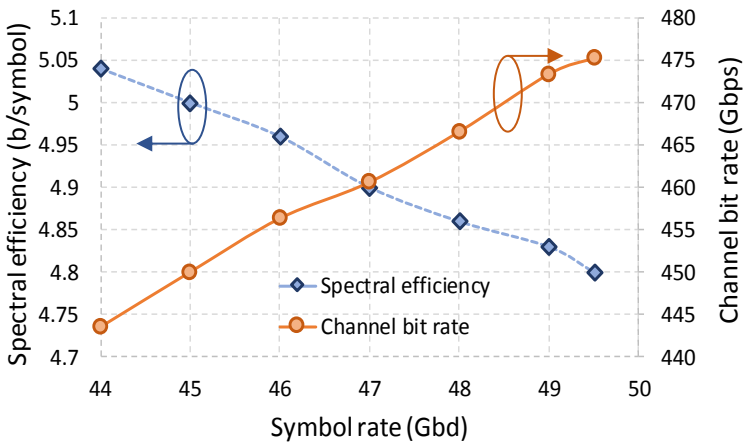

Fig. 4.8: Spectral efficiency (left) and channel bit rate (right) as a function of the symbol-rate for a PCS-64QAM signal

Fig. 4.8 shows the spectral efficiency values for all the symbol rates considered. As expected, this parameter decreases with symbol rate: while for 44 GBd the spectral efficiency is 5.05, for 49.5 GBd it decreases pretty much linearly up to 4.8. However, this decrease is much slower than expected at the beginning and the fact of increasing the symbol rate, in the range of symbol rates considered, always dominates in front to the loss in spectral efficiency. Potential channel bit rate extracted from spectral efficiency is also plotted in the figure. Notice how it gradually increases despite losing in spectral efficiency. It means that the optimum symbol rate is higher than 49.5 Gbps. The maximum value for the interval analysed is 475 Gbps per channel at 49.5 Gbps.

The symbol rate finally chosen for the transmission is 49 GBd. We have selected this baud-rate to leave a margin between channels and avoid interchannel cross-talk due to the fact that lasers are not perfect in practical implementations and some detuning is expected in a 50 GHz grid.

4.3.3 Results

We then performed experimental measurements of the performance of our ultrawide transmission system by sweeping the wavelength of the test channel over all the 250 channels ranging from 1507.63 to 1608.33 nm. The recorded waveforms of all channels were then processed offline as previously described. Fig. 4.9 shows the measured SNR obtained after FEC decoding. The average SNR is about 15 dB, with a deviation of +/-1 dB over the bandwidth. A significant part of the SNR degradation across shorter wavelengths is attributed to the combined effects of SRS, noise figure and higher fibre attenuation.

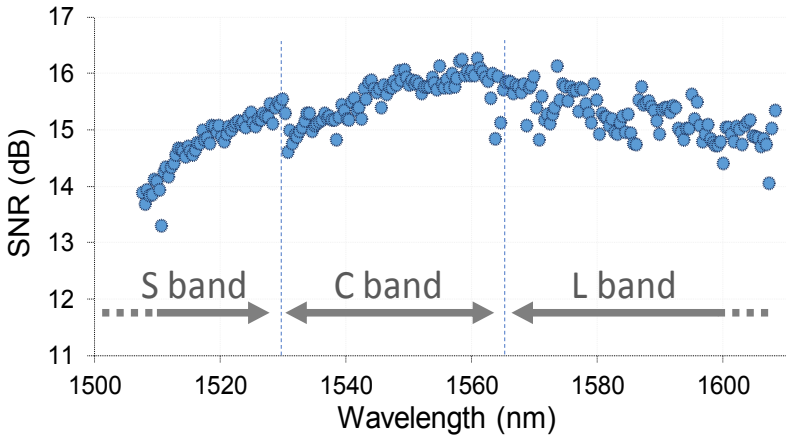

Fig. 4.9: SNR measured after FEC for the 250 channels

Finally, all PS64QAM channels were decoded using 11 members of a family of SC-LDPC codes with rates between 0.8 and 0.91. For each wavelength, the maximum rate resulting in error-free FEC decoding was found.

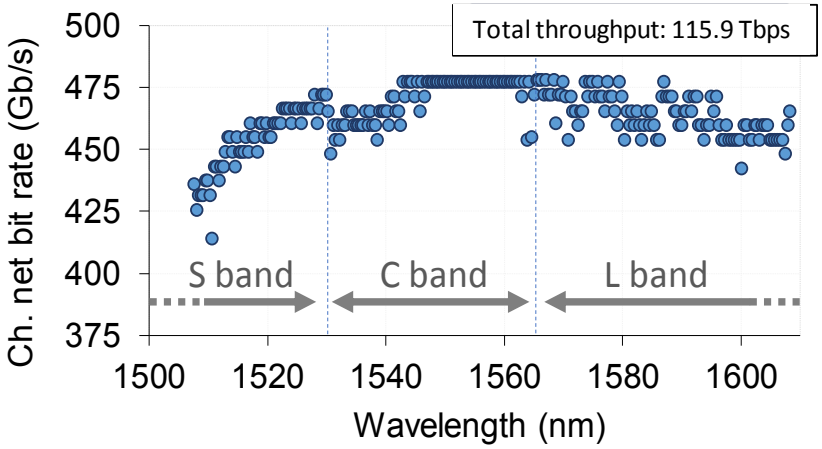

Circles in Fig. 4.10 now show the maximum net throughput for each of the 250 channels, leading to a total throughput of 115.9 Tb/s. We can also note that all the 250 channels show a net throughput above 400Gb/s. This demonstrates that, assuming a single code rate of 0.8 for all the channels, the seamless UWB system enables 100-Tb/s data transport over 100km. Moreover, this capacity can be further enhanced by leveraging the raise of flexible bit rate transceivers. Considering a granularity of 50Gb/s, obtained with the use of two code rates of 0.8 and 0.87, our experiment demonstrates the transmission of 25 x 400Gb/s channels and 225 x 450Gb/s leading to a total net capacity of 111.25 Tb/s.

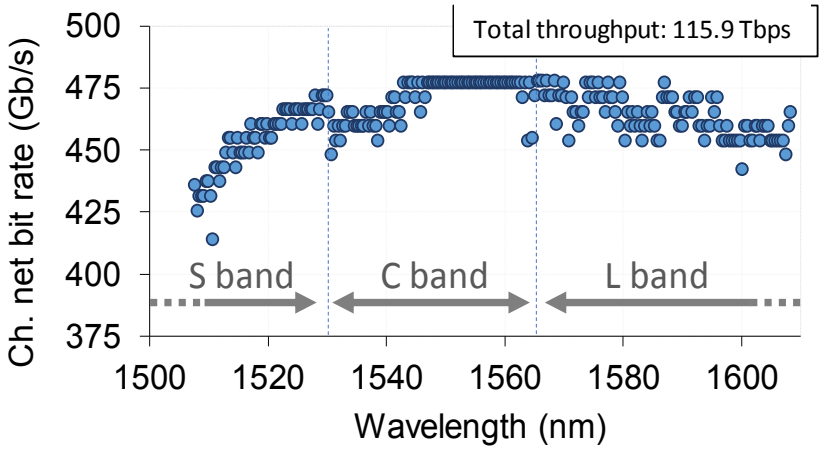

Fig. 4.10: Channel net bit rate for the 250 channels

4.4. *Data centre Interconnect Field Trial*

In this section we present a field trial experiment of SOA-based ultra-wideband systems between two points of presence (POP) of Facebook deployed in the Paris area. The >100-nm ultra-wideband (UWB) system is operated over two spans of standard single mode fibre (SSMF) with SOA-based line amplifiers, including a dual stage SOA with gain flattening filter (GFF) integrated. Two ultra-wideband wavelength selective switches (WSS) are used for combining and dropping channels at POP1 and POP2 respectively.

We demonstrate the successful transport of 64GBd PCS-64QAM channels spaced by 66.7GHz over the whole optical bandwidth. We also demonstrate real time traffic at 250Gb/s per wavelength with PDM-16QAM over C- and L-bands using Nokia 1830 PSS.

4.4.1 Field trial setup

Most of the equipment is located at POP1 in the north of Paris and it is shown in Fig. 4.12. The test bed is depicted in in Fig. 4.11, the transmission line is loaded with wideband ASE noise generated separately in S-, C- and L-bands, in order to minimize the amount of equipment on site. However, this set-up represents also a worst case in term of nonlinear propagation [84] [88] due to the Gaussian distribution of the ASE noise. Two UWB SOA are used to generate ASE noise from 1509nm to 1529nm. C-band and L-band EDFAs are used to generate flat ASE spectra from 1529nm to 1567nm and 1568nm to 1609nm respectively. The availability of ASE source above 1609nm being challenging, five DFB have been added in L+ band up to 1614nm, with a channel spacing set to 1nm. The channels power is set to be equal to the ASE power when observing the spectrum with a 1nm resolution. Then, three consecutive modulated channels spaced by 66.7GHz are generated and combined. The channel under test is obtained from a first tuneable laser (TLS2), which is sent into a PDM I/Q modulator to generate 64GBd probabilistic constellation shaped (PCS) 64QAM signal. Two other lasers (TLS 1 and 3) are combined by a 3dB coupler and modulated separately with 64GBd PCS-

64QAM. The three wavelengths are then combined by a 3dB coupler and amplified by an UWB SOA before being combined with ASE noise through a first UWB WSS by opening the port over 200GHz as depicted in the inset of Fig. 4.13-a).

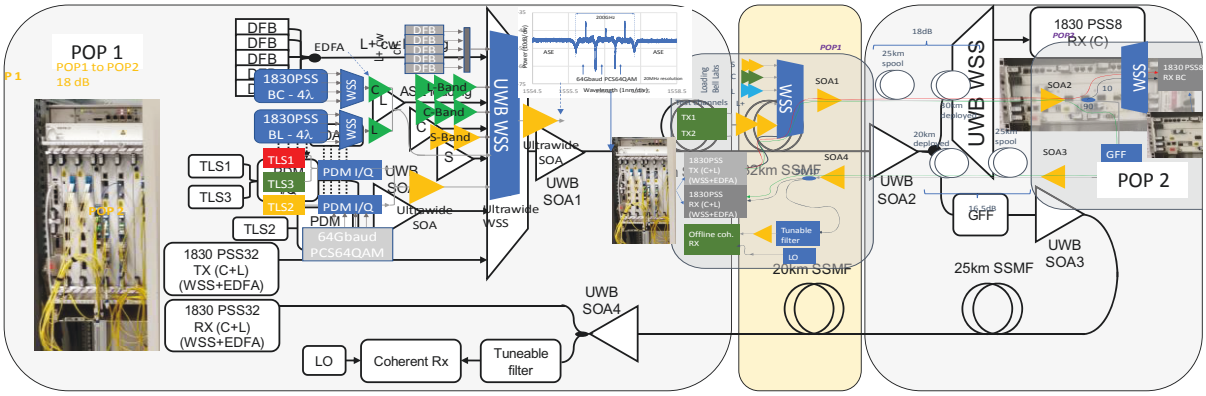

Fig. 4.11: Schematic of the field trial test bed between Facebook POP1 and POP2

Eventually, 4 commercially available D5X500 cards inserted in Nokia 1830PSS shelf are used to generate two sets of four adjacent 50GHz spaced channels modulated at 42GBd with PDM-16QAM, one set in the C-band and the other one in the L-band. These two sets of channels are coupled together and inserted one input port of the UWB WSS.

The first line UWB SOA amplifies the signal coming from the UWB WSS from 10dBm up to 21dBm before being injected into the fibre. The fibre loss from one POP to another POP in a dense urban area is composed of fibre attenuation but also from lumped losses coming from connectors, splices, patch panel in the POP… OTDR measurements have indicated up to 3dB losses within the building, before reaching the transmission fibre. In order to avoid underestimating nonlinear effects occurring within the systems, we have inserted a 25km long spool of SSMF at the output of SOA1 to ensure capturing the majority of Kerr and Raman nonlinear effects. The signal is then amplified at POP2 by SOA2 up to 21dBm followed by a 90/10 coupler. The signal on the 90% port enters a specifically tailored GFF before being amplified again by SOA3 up to 21dBm. Here again, a 25km long spool of SSMF is used to avoid underestimation of Kerr and Raman nonlinear effect because of lumped loss within the building. The 10% output port of the 90/10 coupler is used to extract part of the signal to a second UWB WSS, allowing to select some real-time channels and measure Pre-FEC BER of two channels in C-band on a compact shelf. The two channels are sent together to the two receivers of the coherent card through a simple 3dB coupler. Channel selection is performed by coherent receiver selectivity by adjusting the wavelength of each local oscillator.

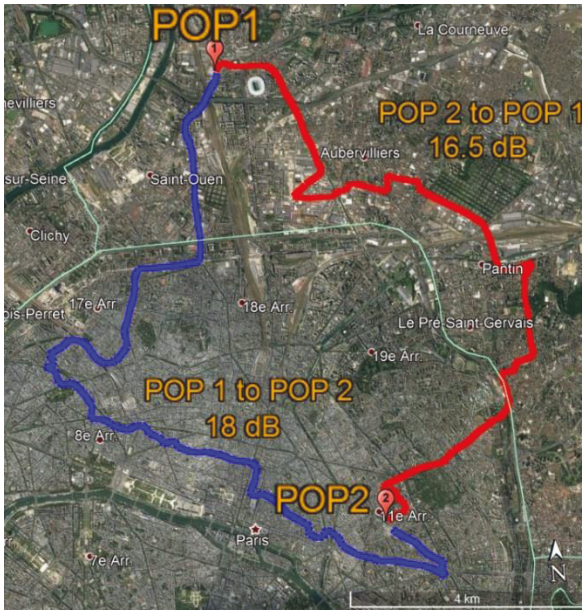

Fig. 4.12: Map of the Paris area and location of POP and fibre

Returning to POP1 from the second light path, the signal is amplified by SOA4 up to 21dBm. First, a 90/10 coupler is used to extract 10% of the signal which is sent into the 1830PSS receiver, composed first of C+L band EDFA, followed by a 1x20 WSS (C-Band and L-Band), before reaching four receivers in C-Band and four in L-Band. The 90% part is sent towards a tuneable filter which selects the 64GBd PCS-64QAM test channel for offline measurements. The filtered signal is then amplified by another UWB SOA before entering the coherent receiver, including a coherent mixer, a tuneable local oscillator, balanced photodiodes and a 33GHz bandwidth high speed sampling scope operating at 80 GS/s. Signal processing is performed as in [19] to compute SNR and generalized mutual information (corrected for pilot overheads), before applying multi-rate spatially coupled low-density parity check (SC-LDPC) FEC decoding.

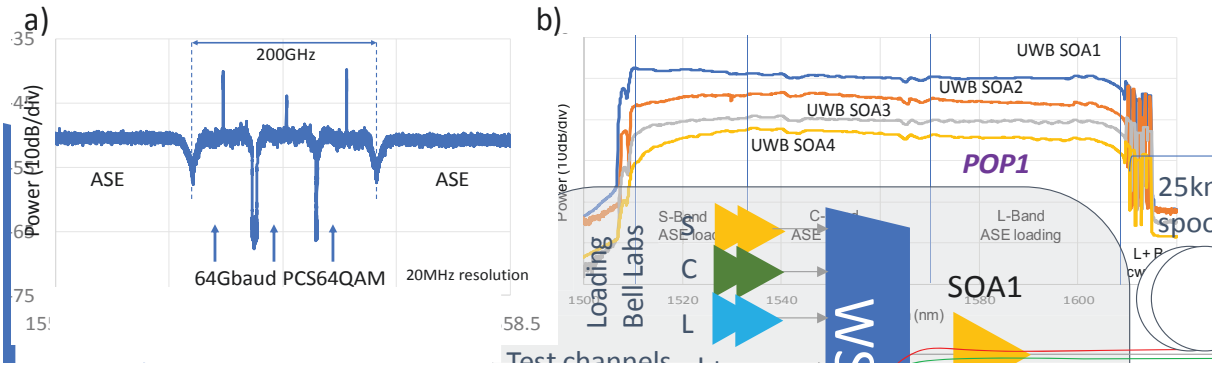

Fig. 4.13: The three test channels combined with ASE noise through a first UWB WSS by opening the port over 200GHz in (a) and schematic of the field trial test bed between Facebook POP1 and POP2 in (b)

The spectrum at the output of each line optical amplifier is shown in Fig. 4.13-b). A slight pre-emphasis is applied at SOA1 to compensate for higher loss

experienced by shorter wavelengths. The GFF is designed to compensate for gain excursion of SOA2 and SOA3 only. The design of the dual stage is shown in more details in Annex C. After SOA4, a significant gain excursion is measured, with significantly lowers the power on the two edges of the >100nm optical bandwidth.

4.4.2 Field trial results

For offline measurements of the PCS-64QAM, the generated set of three channels is then scanned over 13 different spectrum positions, while measuring the performance of the central channel under test. The channel power of test channels is adjusted to be equal to the ASE level when setting the OSA resolution to 0.5nm (62.5GHz resolution).

Similarly to [19], we extract the SNR from the constellation recovered by the coherent receiver. We measured 13 wavelengths across 102nm, roughly every 10nm to obtain an overview of the performance as well as the wavelength dependence of the SNR coming from fibre attenuation variation, stimulated Raman scattering tilt (inducing larger loss for short wavelengths), noise figure and SOA nonlinearity. Still one main contribution to performance degradation of the edge channels comes from the gain non-flatness. Indeed, a single GFF is inserted between SOA2 and SOA3, which compensates the gain excursion of these 2 amplifiers only. The lowest SNR, around 11dB is reported for the shortest wavelength at 1510.9nm. For the centre wavelengths, SNR peaks around 13dB before going down around 12dB for 1612.9nm as depicted in Fig. 4.14. Finally, all PCS64QAM channels were decoded using 24 members of a family of SC-LDPC codes [19] with code rates between 0.67 and 0.91. For each wavelength, the maximum rate resulting in error-free FEC decoding was found and is indicated in Fig. 4.14. Maximum data rate varies from 315Gb/s for the shortest wavelengths up to 525Gb/s for the channels having the highest SNR in the middle of the band.

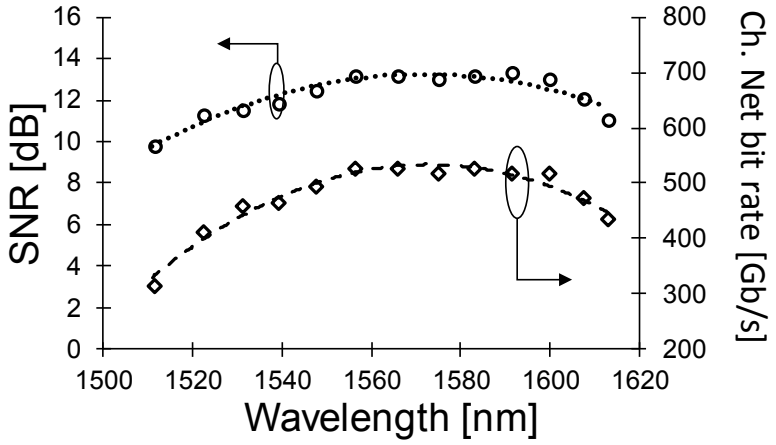

Fig. 4.14: Measured SNR and channel net bit rate measured PCS-64QAM channels over the ultra-wideband system

The performance of 250Gb/s real-time transponders was first measured over 30 minutes for two wavelengths after the first span at POP2 using the 1830 PSS8. These two wavelengths were dropped by the UWB WSS device located at POP2. Then forty wavelengths spread over C- and L- bands were measured over 30 minutes after two spans at POP1 using our PSS32. Typical pre-FEC BER results are reported in Fig. 4.15-a) and clearly show stable performance at each location in both C- and L- bands. Finally, stability measurements have been done at POP1 after two spans over 24 hours. Pre-FEC BER has been converted to Q²-factor and Q²-factor distribution is depicted in Fig. 4.15-b) for one wavelength in C band. The min-max deviation has been measured to be below 0.2 dB for this transponder.

We have demonstrated the transmission of an average 475 Gb/s data rate on a two-span amplified SOA-based ultra-wideband system (>100nm) in the field. In addition, two 100 nm, continuous WSS devices were fabricated to match the ultra wide bandwidth of these amplifiers and were demonstrated in this field trial. Under these conditions the ultra-wideband amplifier would be able to support a potential 90 Tb/s of capacity per fibre when fully loaded. Moreover, the performance with real time line cards, both in C and in L bands, running PDM-16QAM at 250Gb/s per wavelength has been demonstrated to be extremely stable over a 24-hour soak test.

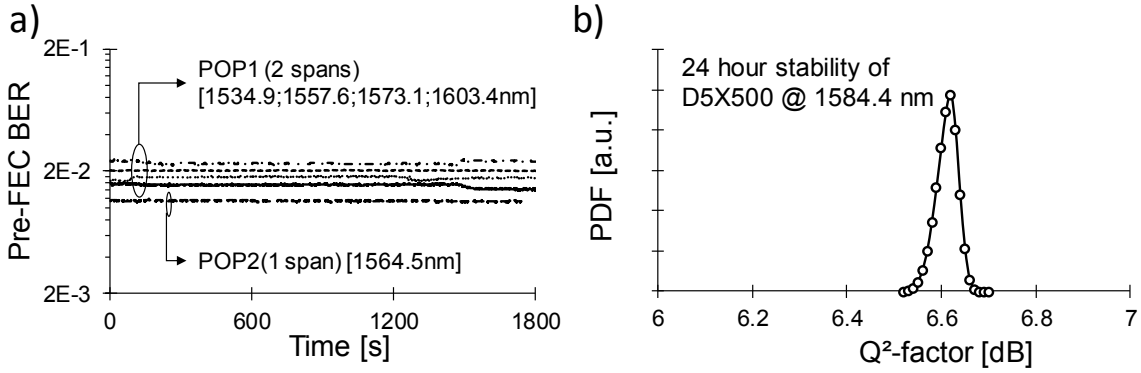

Fig. 4.15: Performance of 250Gb/s 16QAM real time transponders over 1 and 2 spans in (a) and long term stability measurements in C and L-Band for 250Gb/s 16QAM in (b)

4.5. *Towards metro and long-haul applications*

4.5.1 Hybrid Raman/SOA amplification

One of the main drawbacks of semiconductor optical amplification with respect to Erbium-doped fibre amplification is the higher noise figure they usually have. As Fig. 3.15 shows, EDFA presents a NF around 4 and 5 dB while it is 6-7 dB in SOA. This degradation of between 1 and 2 dB along the band is mainly attributed to the extra losses inside the cavity. The gap is even higher if the SOA is operated in flat gain regime. At this operational regime the SOA is weakly saturated, specifically in S Band, making the NF of increase up to 8-10

dB. When several stages of SOA are concatenated, this degradation has an impact on the OSNR of the channel. Consequently, the maximum reach of the system is reduced. It is actually one of the main limitations of the SOA to be used in metro and long-haul applications.

On the other hand, we can take advantage of the stimulated Raman scattering of the optical fibre to obtain an ultra-wideband gain by pumping the transmission fibre with adequate pumps in the range from 1410 to 1510 nm. Although using Raman backwards amplification by itself is not a good alternative because lumped amplification is usually preferred, it can be successfully integrated in a hybrid solution Raman and SOA. This combination offers some advantages because the SOA solves the problem of lumped amplification and at the same time Raman pumping increases the minimum power reached along the fibre so it permits to reduce significantly the equivalent noise figure of the whole amplification system. To illustrate this effect a small test bed has been used with hybrid amplification. Fig. 4.16 shows main parts.

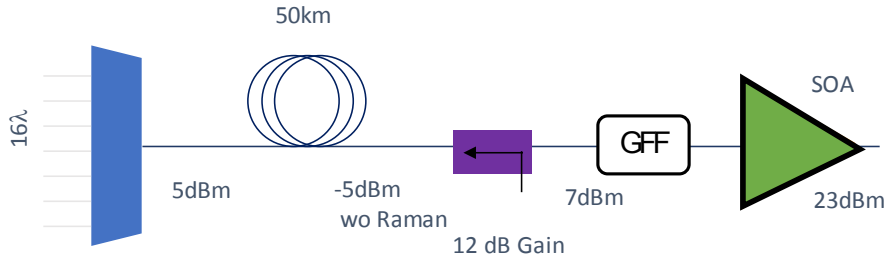

Fig. 4.16: Test bed for Hybrid Raman and SOA amplification

Firstly, 16 continuous wavelengths distributed along the band from 1510 to 1620 nm are coupled in order to simulate a 110-nm transmission as Fig. 4.17-a) shows. The total input power is set to 5 dBm. This signal goes through a fibre spool of 50 km of SSMF so the output power without Raman pumping is -5 dBm (10 dB of losses). If Raman pumping is done the output power increases up to 7 dBm. Finally, a gain flattening filter is placed at the input of the SOA with 5 dB of losses. The current of the SOA is set to obtain an output up to 23 dBm. In Fig. 4.17-b), the spectrum at the output is shown. We have measured the range from 1400 to 1620 nm in order to see the Raman pumps. There is a total of 5 pumps located at 1410, 1430, 1455, 1490 and 1510 nm respectively. Notice that the signal is flat in the entire band from 1510 nm to 1615 nm.

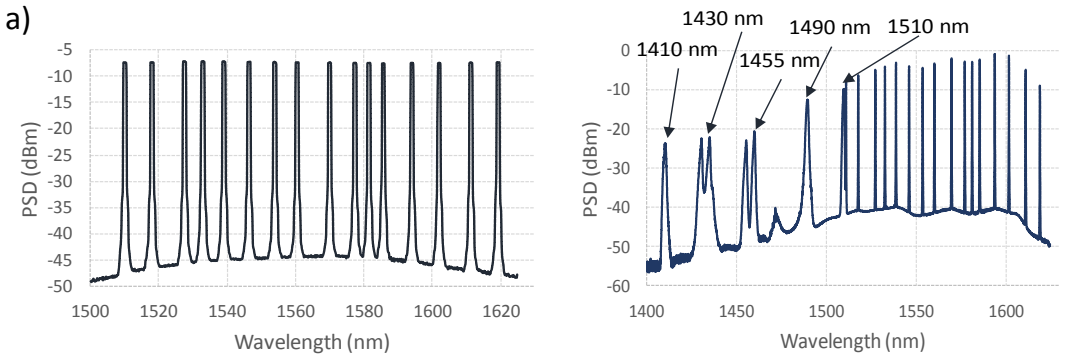

Fig. 4.17: Input spectrum in a) and output spectrum in b)

In Fig. 4.18 the equivalent noise figure is shown. Firstly, we have measured the noise figure of the system when the Raman pumps are not enabled. In this case the noise figure observed is the one obtained when a single SOA operates in flat regime, between 8 and 10 dB. Then the Raman pumps are switched ON. Then we can measure the equivalent noise figure of the Raman pumping and the equivalent noise figure of the hybrid solution. As we can observe in the graphic the Raman pumping scarcely adds noise so the equivalent NF is even negative in dB. The values obtained ranges from 2 dB in S band to -3 dB in L band.

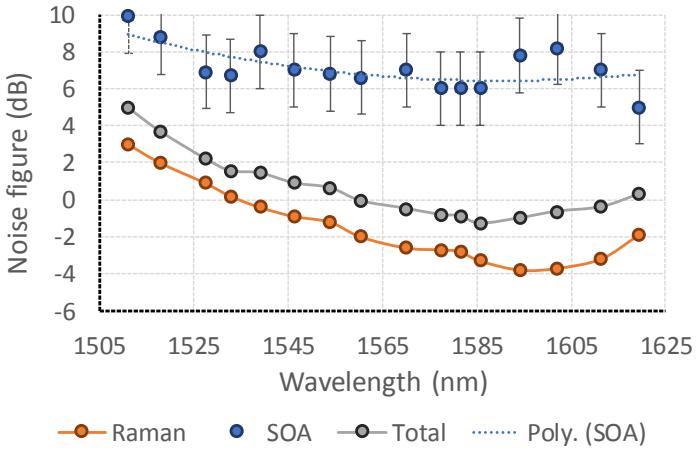

Fig. 4.18: Equivalent Noise Figure with and without Raman.

To measure the equivalent NF of the whole system we use the well-known Friis formula. In this formula the equivalent NF of the first component dominates in front of other contributions. As the equivalent NF of Raman pumping is low it strongly reduces the equivalent NF of the Hybrid solution. In the figure we see how it is lower than 5 dB along the whole band.

With this experiment we have shown how the hybrid solution has the advantage of the two amplification approaches. Thanks to the Raman pumping we have successfully reduced significantly the NF of the SOA. In the future, hybrid solutions Raman pumping and SOA are promising because an UWB amplification system with low equivalent NF can be obtained in the line and the SOA could be used stand-alone in add/drop nodes.

Outlook and conclusions

Internet data traffic has experienced an exponential growth in the two previous decades which has caused the necessity of constantly increase of capacity of existing networks. From the point of view of optical networks, several alternatives have been studied in order to increase the capacity of the optical. Pulse and constellation shaping, fibre nonlinear compensation are some examples of the effort done which have successfully increased the data throughput of current optical networks. Generally, the goal of these approaches consists in increasing the spectral efficiency of the system with the aim of transmitting more bits inside a single symbol. However, improving further the capacity by these means begins to be a huge challenge since the spectral efficiency is already reaching the fundamental Shannon limit.

In this work we have investigated increasing the fibre capacity by exploiting an orthogonal axis: the bandwidth of the system. Since capacity increases with the band, if we increase this last parameter, the capacity of the system is also expected to improve almost linearly. Until now the bandwidth of optical systems was traditionally limited to the bandwidth of the line amplifiers. Since EDFA is the technology most used worldwide, it has become the main limitation. In fact, the amplification provided by an EDFA is usually limited to two different bands of 35 nm, what is known traditionally as C and L bands.

Improving the bandwidth of an EDFA is extremely challenging so a different alternative must be taken into account. Semiconductor optical amplification is a technology that was abandoned in the past for WDM transmission systems simply because its higher nonlinear nature made this technology more complex in front to EDFA. This extra complexity together with its poorer performance (compared with EDFA), restricted the used of the SOA to other fields where its nonlinear nature can be exploited. However, the fact that the bandwidth of a semiconductor optical amplifiers can be extended

beyond 70 nm with a tailored design has converted this technology in a good candidate for the next generation amplifier.

The French project CALIPSO was born some years ago encouraged by some partners such as Nokia Bell Labs, III-V Labs, Egide and Kylia with the aim of developing a tailored SOA with high gain, low noise figure, low nonlinearities and indeed a bandwidth of at least 100 nm. These are the requirements that an ultra-wideband amplifier must fit in order to become the next generation optical amplifier.

The use of semiconductor optical amplification obliges us to take into account its nonlinear nature in our numerical and analytical models to really estimate the performance of the system. Indeed the fact of moving to UWB systems is not straight forward, since the increase of optical bandwidth carries out the necessity of tackle new challenges we used to not care in conventional systems such as the Stimulated Raman Scattering of the optical fibre. On the other hand, the increase of optical bandwidth increments the complexity to manage the flatness of the enter bunch of channels after several spans, the OSNR...

This work has studied all the required points to follow before implementing a technology into a real optical system. In the first part of the work the matter of modelling the SOA nonlinear nature has been investigated. Firstly, the model under test has been introduced. We have decided to work with the reservoir model which has provided a good estimation of the SOA nonlinear dynamics. Using a state-of-the-art SOA provided by Thorlabs we have successfully obtained experimentally all the parameters required to tune this model in static regime. Then we have characterized its dynamic regime by measuring its relative intensity noise (RIN) response and the linewidth enhancement factor. The measure of this last parameter has been obtained by processing the temporal traces of a modulated signal after the pass though the SOA with a high sampling rate oscilloscope. A value of 4.8 of linewidth has been obtained for the Thorlabs SOA which is in line with previous measurements of this parameter. This is the first time that the linewidth factor of an SOA is obtained using a coherent receiver. We have concluded that despite not being the most accurate existent model, the reservoir model can be adequate for analysing the performance of an optical system generally limited to a linear regime or weakly nonlinear regime. Furthermore, we have observed a good fit of this model with the experimental measurements of the RIN response reaching the conclusion that the reservoir model is a powerful tool capable to adequately estimate the dynamic regime of an SOA. Finally, we have assessed that correlation between channels in a WDM causes an increase of SOA nonlinearities. Some numerical simulations have been performed to determine the minimum length of the decorrelation fibre which has been established to 25 km of SSMF when transmitting at least 60 channels in a 50-GHz grid and then some experiments have been done to validate it.

Then, the second part of our work has mainly focused on the study of the capabilities of the SOA to become the next generation optical amplifier for ultra-wideband systems. To do that we have firstly characterized the novel UWB SOA provided by the CALIPSO project. We have observed all the improvements done with respect to the state-of-the art SOA which have allowed this novel SOA to take the step to finally be deployed in WDM transmission systems. In a first case we have observed how the tailored design has permitted to improve significantly the saturation power of the system. Noise figure is other parameter that has been significantly improved passing from 9-10 dB to 6-7 dB. Finally, the carrier lifetime factor has been increased from 220 ps measured in the ThorLabs SOA up to 700 ps. All these improvements have contributed to reduce the nonlinear nature of the novel SOA.

Furthermore, we have studied experimentally the saturation regime of the SOA to see how the nonlinearities are progressively added when the SOA when the input power is progressively increased. We have also observed how shorter wavelengths saturate at lower input power than longer ones. All these aspects are important to be known because they are needed in system design. In this chapter a new technique has been investigated to compensate the nonlinearities of the optical fibre in UWB systems: the multicarrier approach. However, the conclusion reached is that the benefit obtained by this technique in our experiments done is not high enough to justify its inclusion in our UWB transmission systems.

Finally, the last part of the work has been to test the novel UWB SOA in a real transmission environment. The target application selected is data centre interconnection. In fact, the traffic in data centres has exploited since the birth of social networks and some manufactures such as Facebook requires increasing the traffic. In this work the first continuous bandwidth transmission over 100 km of EX2000 fibre is demonstrated with a total throughput net of 115.9 Tbps. This experiment has allowed to measure for the first time all the possible impairments associated with such a wide bandwidth such as the SRS effect of an optical transmission fibre. Then, we have also demonstrated the transmission of an average 475 Gb/s data rate on a two-span amplified SOA-based ultra-wideband system (>100nm) between two points of presence (POP) of Facebook deployed in the Paris area. Moreover, the performance with real time line cards, both in C and in L bands, running PDM-16QAM at 250Gb/s per wavelength has also been demonstrated assessing the extremely stable performance of the UWB SOA over a 24-hour soak test.

With this field trial we have demonstrated all the capabilities of the SOA to become the next generation optical amplifier. Nevertheless, further improvement is expected to improve its performance. One feasible approach is to concept a hybrid Raman and SOA amplification system. Hybrid amplifier solves finally the problem of the high noise figure of the SOA and simultaneously the issue of lumped amplification for networks with ROADMs.

This is a good approach to be used in next years which paves the way to implement the UWB SOA for metro and long-haul links.

List of acronyms and symbols

List of acronyms

ADC	analog to digital converter
ASE	amplified spontaneous emission
BER	bit error rate
BPSK	binary phase shift keying
CD	chromatic dispersion
CMA	constant modulus algorithm
CPE	carrier phase estimation
CW	continuous wave
DAC	digital to analog converter
DEMUX	demultiplexer
DCI	data-centre-interconnect
DFB	distributed feedback laser
FEC	forward error correction
FWM	four wave mixing
GVD	group velocity dispersion
GMI	generalized mutual information
LDPC	low-density parity codes
MUX	multiplexer

MZM	Mach-Zendher modulator
NF	noise figure
NLPN	nonlinear phase noise
NLT	nonlinear threshold
OSA	optical spectrum analyser
OSNR	optical signal to noise ratio
PBS	polarisation beam splitter
PDM	polarisation division multiplexing
PMD	polarisation mode dispersion
PSCF	pure silica core fibre
QPSK	quaternary phase shift keying
ROADM	reconfigurable optical add and drop multiplexer
SE	spectral efficiency
SER	symbol error ratio
SNR	signal to noise ratio
SOA	semiconductor optical amplifier
SPM	self-phase modulation
SRS	stimulated Raman scattering
SSMF	standard single mode fibre
TLS	tuneable laser source
UWB	Ultra-wide band
VOA	Variable optical attenuator
WSS	wavelength selective switch

List of symbols

$\langle\,\rangle$	ensemble average
α	attenuation coefficient
β	mode-propagation constant
λ	optical wavelength
λ_0	zero-dispersion wavelength
γ	nonlinear coefficient
Φ_{NL}	nonlinear induced phase modulation
σ_g	differential gain
τ_c	carrier lifetime
τ_{eff}	effective carrier lifetime
τ_p	photon lifetime
η_{sh}	shot noise
ω	angular frequency
A_{eff}	effective fibre area
B_{ref}	reference bandwidth
c	speed of light in the vacuum ($c=2.99792\cdot10^8$ m/s)
CB	conduction band
d_{min}	minimum Euclidian distance
D	dispersion factor
D'	dispersion factor slope
f	frequency
F	noise factor
g_R	Raman gain coefficient
G	gain (amplifier)
G_{eff}	effective Raman gain
$G_{ON/OFF}$	on-off Raman gain
h	Planck's constant ($6.626068\cdot10^{-34}$ J·s)
I	in-phase component
I_{PD}	photocurrent
j	imaginary unit

L	fibre length
L_D	normalised dispersion length
L_{eff}	effective fibre length
n	refractive index
N_0	noise power spectral-density
N_{spans}	number of spans in the transmission line
n_0	linear refractive index
n_2	nonlinear refractive index
N	number of electrons in conduction band
N_0	transparency value
NF	noise figure
n_{sp}	spontaneous emission factor
P	power
Ph	Photons
P_{ch}	power per channel
P_{sat}^{-3dB}	3-dB output saturation power
$P_{sat,in}^{-3dB}$	3-dB input saturation power
P_s	Reservoir model saturation power
Q	quadrature component
R_{sp}	spontaneous emission term
R_b	bit rate
RIN	Relative intensity noise
t	time
T_S, T_0	symbol period
VB	valence band
V_π	characteristic voltage of a modulator
z	transmission distance

Acknowledgements

I would like to thank to Jeremie Renaudier, Gabriel Charlet and Yann Frignac for their participation in the survey that supported my work in this way and helped me get results of better quality. I would also thank to them for offering me the possibility to do research in this very interesting topic with a great potential which has permitted me to improve my career prospects. I am specifically grateful with Jeremie for their patience and support in overcoming numerous obstacles I have been facing through my research and for his good advice.

I would like to thank my colleagues in Nokia Bell Labs for their feedback, cooperation and of course friendship: Ivan, Rafael, Amir, Patrice, Patrick, Elie… In addition I would like to express my gratitude to the members of project CALIPSO because they always give me good feedback to steer my research in the good direction specifically to Romain Brenot, Hélène Debrégeas and Agnès Verdier.

Last but not the least, I would like to thank my family: my parents for supporting me spiritually throughout writing this thesis and my life in general and all my friends they were there always I needed them.

Also, I would like to thank to all the members of the jury for accepting our invitation specifically to the reviewers of this manuscript.

Finally I would like to acknowledge the French government for the funding of the CALIPSO project which developed the novel UWB SOA is studied in this work.

Appendices

A. Bit error ratio and Q^2 factor

The performance of an optical transmission system is often measured in terms of bit error ratio (BER) or Q^2-factor. The BER is defined as the ration between the number of errors found after decoding, N_{errors}, and number of detected bits, N_{tot}:

$$BER = \frac{N_{errors}}{N_{tot}} \tag{A.1}$$

Hence, the lower the BER, the better the system behaves. The most important feature of a digital transmission system is indeed the ability to operate with a sufficient small BER. A transmission is considered "error-free" when BER is smaller than 10^{-13} after propagation.

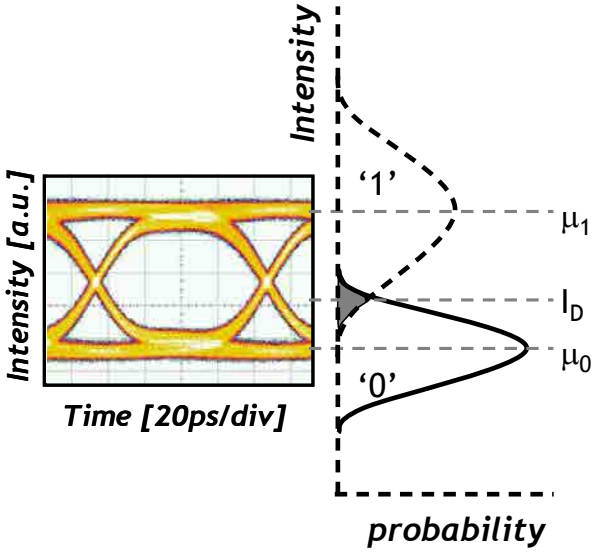

Fig. A.1: Probability symbol density of a noisy OOK signal

The Q-factor was first defined to estimate the performance of OOK systems. Fig. A.1 depicts the probability density of the two symbols of an OOK signal, '0' and '1'. One can express the optimal decision threshold on a signal degraded by ASE:

$$I_D = \frac{\sigma_0\mu_1 + \sigma_1\mu_0}{\sigma_0 + \sigma_1} \tag{A.2}$$

where μ_0 and μ_1 are the mean photocurrents of the symbol '0' and '1', respectively; and σ_0 and σ_1 are the standard deviations. The Q factor is then defined as:

$$Q = \frac{\mu_1 - \mu_0}{\sigma_0 + \sigma_1} \tag{A.3}$$

The photocurrent of an ideal photodiode can be approximated with a Gaussian distribution for high enough OSNR (>10 dB) and low ISI. Under these assumptions, Q-factor can be used to estimate the BER following the expression:

$$BER = \frac{1}{2}\,erfc\left(\frac{Q}{\sqrt{2}}\right) \tag{A.4}$$

where $erfc(x)$ is the complementary error function, which for a Gaussian distribution is:

$$erfc(x) = \int_{x}^{\infty} \exp(-y^2) \tag{A.5}$$

Throughout this thesis, Q factor is not used to estimate BER but it is used as a conversion of a *measured* BER and expressed in [*dB*], so as:

$$Q^2\,factor = 20\log_{10}\left[\sqrt{2}\;erfc^{-1}(2BER)\right] \tag{A.6}$$

Q^2 factor in [*dB*] has the advantage of being proportional to the OSNR. 1-dB increase in OSNR results in ~1 dB increase in Q^2 factor. Fig. A.2 shows the relation between the BER and the Q^2 factor as well as the correspondence of several usual values.

BER	Q^2 factor[dB]
$1\cdot10^{-2}$	7.33
$4\cdot10^{-3}$	8.47
$1\cdot10^{-3}$	9.80
$1\cdot10^{-4}$	11.40
$1\cdot10^{-5}$	12.60
$1\cdot10^{-6}$	13.54
$1\cdot10^{-7}$	14.32
$1\cdot10^{-8}$	14.98
$1\cdot10^{-9}$	15.56

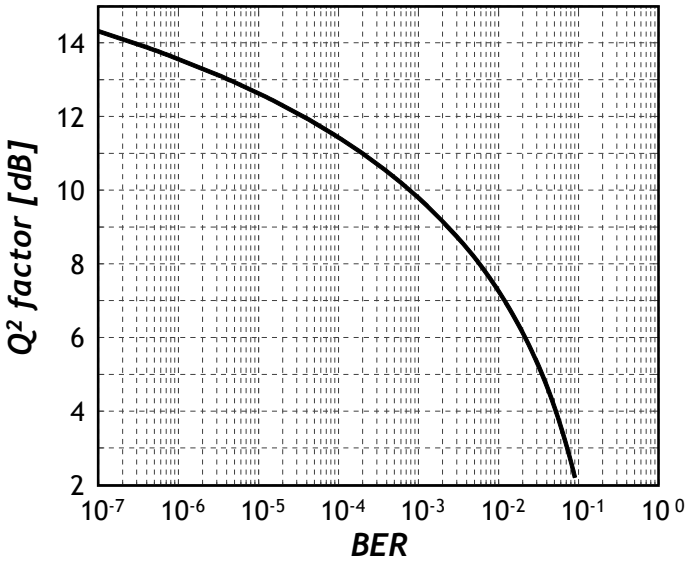

Fig. A.2: Relation between bit error ratio and Q^2 factor.

B. Small signal model equation derivation

Let's start for the general equation for the reservoir model:

$$\tau_c \quad \frac{dh_i(t)}{dt} = \; h_0 \quad - \; h_i(t) - \left[e^{h \;\; (t)} - 1\right] \bar{p}_{out}(t) \tag{B.1}$$

Let consider:

$$h(t) = \; \bar{h} + \partial h(t) \tag{B.2}$$

So substituting *(B.2)* in *(B.1)* and arranging the terms we obtain:

$$\partial h \left[\tau_c \frac{d}{dt} + 1 + \frac{\overline{P_{out}}}{P_{sat}}\right] = \; h_0 - \; \bar{h} + \left[1 - e^{\bar{h}} \;\right] \frac{\overline{P_{in}}}{P_{sat}} + \left[1 - e^{\bar{h}} \;\right] \frac{\overline{\partial P_{in}}}{P_{sat}} \tag{B.3}$$

Now applying the perturbative theory, we remove all the terms which are not dependent of the time. Finally we transform it to the frequency domain knowing that:

$$F\left[\frac{d}{dt}\right] = j\omega \tag{B.4}$$

We obtain:

$$\partial H(\omega) \left[j\omega\tau_c + 1 + \frac{\overline{P_{out}}}{P_{sat}}\right] = \; \left[1 - e^{\bar{h}} \;\right] \frac{\overline{\partial P_{in}(\omega)}}{P_{sat}} \tag{B.5}$$

We rearrange the terms:

$$\partial H(\omega) = \frac{\dfrac{\left[1 - e^{\bar{h}} \;\right]}{1 + \dfrac{\overline{P_{out}}}{P_{sat}}}}{\left[1 + j\omega \dfrac{\tau_c}{1 + \dfrac{\overline{P_{out}}}{P_{sat}}}\right]} \overline{\partial P_{in}(\omega)} \tag{B.6}$$

We define K and τ_{eff} as:

$$\tau_{eff} \triangleq \frac{\tau_c}{1 + \dfrac{\overline{P_{out}}}{P_{sat}}} \tag{B.7}$$

$$K_i \triangleq \frac{1 - e^{\bar{h}}}{\tau_c} \tag{B.8}$$

So simplifying we obtain:

$$\partial H(\omega) = \frac{\overline{\partial P_{in}(\omega)}}{P_{sat}} \frac{K\,\tau_{eff}}{\left[1 + j\omega\tau_{eff}\right]} \tag{B.9}$$

This in time domain can be expressed as:

$$dh_i(t) \approx l_i(t) * \overline{\partial \mathrm{P_{in}(t)}} \tag{B.5}$$

Where * denotes convolution in time domain and $l_i(t)$ is a low-pass filter. The impulsional response is the one expected for a first order low-pass:

$$l_i(t) \triangleq K_i e^{-t/\tau_{eff_i}} u(t) \tag{B.6}$$

C. Dual stage SOA

As we showed in chapter 3, the bias current injected in the SOA can be tuned to make the SOA work in flat gain regime for any given input power. Fig. 3.10-a) shows the gain when the SOA operates at this regime. Despite the fact that there is no tilt between the two extremes, it can be observed that the gain in these regions of the spectrum is almost 3 dB lower than in the centre part. This faintness in the gain causes a curvature of the spectrum at the output of the module. When several modules are concatenated, this curvature is becoming more and more important, limiting significantly the number of spans we can transmit. To solve this issue, a gain flattening filter (GFF) can be properly designed. A GFF is a static gain equalizer designed to obtain a flat spectrum at the output of an amplification stage. Typical GFF generate losses of around 4-5 dB because they attenuate the wavelengths with higher gain reducing the effective gain of the SOA to the lower gain of the band. To compensate the losses of the GFF a second SOA is considered.

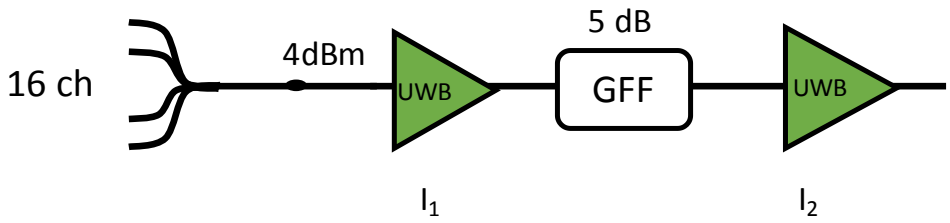

Fig. C.1: Test bed for GFF characterization

The design of the dual stage SOA is considered in this section. With this goal, we have used the test bed depicted in Fig. C.1. First 16 continuous wavelengths are coupled and launched into the first SOA at 4 dBm of input power. After the SOA, the GFF is placed. The GFF has been specifically designed to remove the curvature in the gain after two SOA. Finally, a second SOA is used to compensate the losses of the GFF. The variables to be characterized are the two bias currents of both SOA. To do it the gain and the tilt are measured at the output of the system for all the possible combinations of bias currents which ranges from 600 to 1500 mA. The measure to be optimized is the flatness at the output so the ratio between Δg and G is considered. Let's call Δg to the difference between the maximum and the minimum gains along the spectrum and G, the mean gain. The lower this value, the flatter the spectrum becomes. But also we are interested in leaving the dual stage at maximum output power and maximum OSNR.

Fig. C. 2-a) shows the ratio between Δg and G for all the input bias currents. It can be observed that giving an I_1, it always exists a I_2 which minimizes this parameter. It is why we have plotted a strong black line. This line represents the good combination of currents that minimizes the tilt of gain at the output.

The second parameter to be optimized is output power. Fig. C. 2-b) shows its evolution again with bias currents. As it is noticed the SOA which

acquires the main role is the second SOA. It is the SOA that mainly determine the output power. On the contrary, the SOA which is the one that determines the OSNR at the output is the first one. Fig. C. 2-c) shows the mean OSNR at the output. We observe that the higher the first bias current, the higher the OSNR at the output. It has sense since the OSNR depends basically of the power at the input of the SOA.

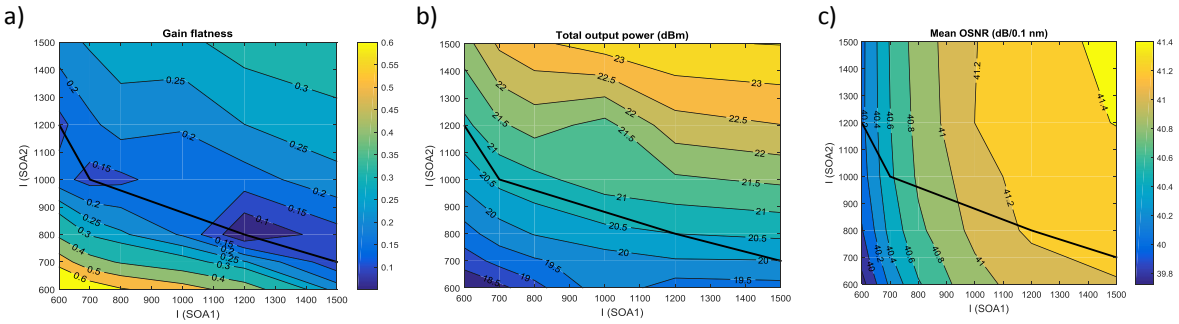

Fig. C. 2: Ratio between Δg and G in (a), output power in (b) and mean OSNR in (c) for different I_1 and I_2

Finally, the line that optimizes the gain flatness is also plotted in Fig. C. 2-b) and Fig. C. 2-c). We observe that at 4 dBm of input power the output is 21 dBm. It means that this dual stage can provide 17 dB of real flat gain.

Anyway in our case, we are not interested in working at flat regime because the SRS effect has also to be considered. If we want to compensate the Raman tilt we have to operate the SOA at higher bias currents. It is why we fix both bias currents to 1200 mA. Like this we can push the dual stage amplifier to at total output power of 22-23 dBm and higher OSNR.

With this characterization, we assess that the optimal point of work of the dual stage SOA is not the one that provides flat output power but the one with a tilt that permits to compensate the Raman tilt. In this case the fact of having SRS becomes even positive because allows us to push the SOAs to obtain higher gain and higher OSNR. So the higher the SRS, the higher gain can be obtained but the SOA.

Bibliography

[1] C. Cox et al, «Techniques and performance of intensity-modulation analog optical links.,» *IEEE Transactions on Microwave theory and techniques,* vol. 45, n°18, p. 1375–1383, 1997.

[2] L. Mach, «Über einen Interferenzrefraktor,» *Zeitschr. für Instrumentenkunde,* vol. 12, pp. 89-93, 1982.

[3] L. Zehnder, «Ein neuer Interferenzrefraktor,» *Zeitschr. für Instrumentenkunde,* vol. 11, pp. 275-285, 1981.

[4] J. S. G. Evangelides et al, «Polarization multiplexing with solitons,» *Journal of Lightwave Technology,* vol. 10, n°11, pp. 28-35, Jan 1992.

[5] A. R. Chraplyvy et al, «1-Tb/s Transmission Experiment,» *Photonics Technology Landters,* vol. 8, n°19, p. 1264–1266, 1996.

[6] I. P. Kaminow et al, Optical Fiber Telecommunications IIIA & IIIB, Academic Press, 1997.

[7] ITU-T, Optical System Design and Engineering Considerations, Feb. 2006.

[8] C. E. Shannon, «A Mathematical Theory of Communication,» *Bell Syst. Tech. J,* vol. 27, n°13, pp. 379-423, 1948.

[9] R. W. Hamming, «Error Detecting and Error Correcting Codes,» *Bell Syst. Tech.,* vol. 29, n°12, pp. 147-160, 1950.

[10] A. Hocquenghem, «Codes correcteurs d'erreurs,» *Chiffres,* vol. 2, pp. 147-156, 1959.

[11] R. C. Bose and D. K. Ray-Chaudhuri, «On A Class of Error Correcting Binary Group Codes,» *Information and Control,* vol. 3, n°11, pp. 68-79, 1960.

[12] I. S. Reed and G. Solomon, «Polynomial Codes over Certain Finite Fields,» *Journal of the Society for Industrial and Applied Mathematics (SIAM,* vol. 8, n°12, pp. 300-304, 1960.

[13] R. J. McEliece et al, «Turbo decoding as an instance of Pearl's "belief propagation" algorithm,» *IEEE Journal on Selected Areas in Communications,* vol. 16, n°12, p. 140–152, 1998.

[14] R. Gallager, «Low-density parity-check codes,» *IRE Trans. Inf. Theory,* vol. 8, n°11, pp. 21-28, Jan. 1962.

[15] David J.C. MacKay and Radford M. Neal, «Near Shannon Limit Performance of Low Density Parity Check Codes,» *Electronics Letters,* 1996.

[16] I. B. Djordjevic et al, «Using ldpc-coded modulation and coherent detection for ultra highspeed optical transmission,» *Journal of Lightwave Technology,* vol. 25, n°111, p. 3619–3625, 2007.

[17] H. D. Pfister, «A Brief Introduction to Spatially-Coupled Codes and Threshold Saturation,» Chinese University of Hong Kong, 2015.

[18] S. Kudekar et al, «Threshold Saturation via Spatial Coupling: Why Convolutional LDPC Ensembles Perform So Well over the BEC,» *IEEE Trans. Inf. Theory,* vol. 57, n°12, p. 803–834, 2011.

[19] A. Ghazisaeidi et al, «65Tb/s Transoceanic Transmission Using Probabilistically- Shaped PDM-64QAM,» *Proc ECOC, Th.3.C.4*, Düsseldorf, 2016.

[20] K. C. Kao and Hockham G. A., «Dielectric-fibre surface waveguides for optical frequencies,» *Proc. of Institution of Electrical Engineers,* vol. 113, n°17, pp. 1151-1158, 1966.

[21] E.-G. Neumann, Single-Mode Fibers., Springer Verlag, 1988.

[22] H. G. Unger, Planar Optical Waveguides and Fibers, Oxford, 1977.

[23] A. W. Snyder, «Excitation and Scattering of Modes on a Dielectric or Optical Fibre,» *IEEE Transactions on microwave theory and techniques*, n°112, pp. 1138-1144, 1969.

[24] ITU-T Recommendation, «G.652.D».

[25] Chigusa Y. et al, «Low-loss Pure-Silica-Core Fibers and Their Possible Impact on Transmission Systems,» *Journal of Lightwave Technology,* vol. 23, n°111, Nov Nov. 2005.

[26] S. Sudo et al, «Low-OH content optical fiber fabricated by vapour-phase axial-deposition method,» *Electronics Letters,* vol. 14, 1978.

[27] K. H. Chang et al, «New Hydrogen Aging Loss Mechanism in the 1400 nm Window,» *OFC, post-deadline paper PD22*, San Diego, 1999.

[28] ITU-T G.Sup39, Optical System Design and Engineering Considerations, 2006.

[29] K. Nagayama et al, «Ultra-Low-Loss (0.1484 dB/km) Pure Silica Core Fibre and Extension of Transmission Distance,» *Electronic Letters,* vol. 38, n°120, 2002.

[30] G. Keiser, Optical Fiber Communications, third edition, McGraw-Hill, 2000.

[31] G. P. Agrawal, Fiber-Optic Communication Systems, 3rd ed. John Wiley & Sons, 2002.

[32] E. L. Bucklet et al, «Electrostrictive contribution to the intensity-dependent refractive index of optical fibers,» *Optics Letters,* vol. 21, n°115, p. 1117–1119, 1996.

[33] S. V. Chernikov. and J. R. Taylor, «Measurement of normalization factor of n2 for random polarization in fiber,» *Optics Letters,* vol. 21, n°119, p. 1559–1561, 1996.

[34] P. M. Krummrich et al, «Experimental Comparison of Raman Thresholds of Different Transmission Fibre Types,» *Proc. ECOC, paper 4.4.1.*, Munich, 2000.

[35] S. Namiki et al, «Ultrabroad-Band Raman Amplifiers Pumped and Gain-Equalized by Wavelength-Division-Multiplexed High-Power Laser Diodes,» *Journal of Selected Topics in Quantum Electronics,* vol. 7, n°11, pp. 3-16, Jan-Feb. 2001.

[36] E. Desurvire et al, «High-Gain Erbium-Doped Traveling-Wave Fiber Amplifier,» *Optics Letters,* vol. 12, n°111, p. 888–890, Nov 1987.

[37] Mears R. J. et al, «Low-Noise Erbium-Doped Fiber Amplifier Operating at 1.54 µm,» *Electronics Letters,* vol. 23, n°119, p. 1026–1028, 1987.

[38] A. Einstein, «Zur Quantentheorie der Strahlung,» *Physikalische Zeitschrift,* vol. 18, p. 121–128, 1917.

[39] E. Desurvire, Erbium-Doped Fiber Amplifiers, Wiley Interscience, 1994.

[40] E. Desurvire et al, «Erbium-Doped Fiber Amplifiers,» *Device ans System Developements,*, Wiley Interscience, 2002.

[41] Q. Wang et al, «Carrier lifetime in erbium-doped GaN waveguide emitting in 1540 nm,» *Applied Physics Letters,* vol. 97, 2010.

[42] R. H. Stolen, «Raman Oscillation in Glass Optical Waveguide,» *Applied Physics Letters,* vol. 20, n°12, p. 62–64, 1972.

[43] J. Hegarty, «CW Pumped Raman Preamplifier in a 45 km-Long Fibre Transmission System Operating at 1.15µm and 1Gbit/s,» *Electronics Letters,* vol. 21, n°17, p. 290–292, 1985.

[44] Finisar, «Applications for Distributed Raman Amplification,» *White paper,* 2012.

[45] R. A. Linke and A. H. Gnauck, «High-capacity coherent lightwave systems,» *Journal of Lightwave Technology,* 1988.

[46] K. Kikuchi, «Coherent optical communication systems,» *Optical Fiber Telecommunications VB: systems and networks,* 2008.

[47] S. J. Savory, «Digital filters for coherent detection,» *Optics Express,* vol. 16, n°12, pp. 804-817, 2008.

[48] S. J. Savory et al, «Digital Equalisation of 40Gbit/s per Wavelength Transmission over 2480km of Standard Fibre Without Optical Dispersion Compensation,» *ECOC*, Cannes, 2006.

[49] M. J. Ready et al, «Blind equalization based on radius directed,» *1990 International Conference on Acoustics, Speech, and Signal*, 1990.

[50] M. Morelli et al, «Feedforward frequency estimation for PSK: A tutorial,» *Eur. Trans. Telecommun*, 1998.

[51] I. P. Kaminow et al, Optical Fiber Telecommunication, IVA & IVB,, Academic press, 2002.

[52] H. Haus, «The proper definition of noise figure of optical amplifiers,» *Proc. of Optical Fiber Communication Conference OFC, paper ThU3 1*, San Diego, 1999.

[53] A. Carena et al, «Statistical Characterization of PM-QPSK Signals after Propagation in Uncompensated Fiber Links,» *ECOC*, 2010.

[54] P. Poggiolini, «The GN Model of Non-Linear Propagation in,» *Journal of lightwave technology,* vol. 30, n°124, 2015.

[55] A. Carena, «EGN model of non-linear fiber propagation,» *Optics Express,* vol. 22, n°113, pp. 16335-16362, 2014.

[56] A. Vannucci et al, «The RP Method: A New Tool for the Iterative Solution of the Nonlinear Schrödinger Equation,» *Journal of Lightwave Technology,* vol. 20, n°17, pp. 1102-, 2002.

[57] Paolo Serena and Alberto Bononi, «Perturbative Propagation Models for Coherent Systems,» *ACP*, 2014.

[58] Paolo Serena and Alberto Bononi, «An Alternative Approach to the Gaussian Noise Model and its System Implications,» *Journal of Lightware Technology,* vol. 31, n°122, pp. 3489-3499, 2013.

[59] Carlos L. Janer and Michael J. Connelly, «On the correct modeling of semiconductor optical amplifier RIN and phase noise for optical phase shift keyed communication systems,» *Optics Express,* vol. 18, n°126, pp. 27455-27467, 2010.

[60] P Berger et al, «Dynamic saturation in semiconductor optical amplifiers: accurate model, role of carrier density, and slow light,» *Optics Express,* vol. 18, n°12, pp. 685-693, 2010.

[61] Michael J. Connelly, «Wideband Semiconductor Optical Amplifier,» *Journal of quantum electronics,* vol. 37, n°13, pp. 439-446, 2001.

[62] G. P. Agrawal and N. K. Dutta, Long-wavelength Semiconductor Lasers, Van Nostrand Reinhod, 1986.

[63] H. Ghafouri-Shiraz, The Principles of Semiconductor Laser Diodes and Amplifiers, Imperial College Press, 2004.

[64] M. J. Connelly, Semiconductor Optical Amplifiers, Kluwer Academic Publishers, 2002.

[65] G. P. Agrawal, Nonlinear Fiber Optics, John Wiley and Sons, 2003.

[66] G.P. Agrawal and N.A. Olsson, «Self-Phase Modulation and Spectral Broadening of Optical Pulses in Semiconductor Optical Amplifiers,» *IEEE J. Quantum Electron,* pp. 2297-2306, 1989.

[67] William Rideout et al, «Relative Intensity Noise in Semiconductor Optical Amplifiers,» *IEEE Photonics Technology Letters,* vol. 1, n°112, pp. 438-440, 1989.

[68] Ki-Hyuk Lee and Woo-Young Choi, «Measurement of SOA Differential Carrier Lifetimes and a-Factors using SOA Optical Modulation Responses».

[69] N. Storkfelt et al, «Measurement of Carrier Lifetime and Linewidth Enhancement Factor for 1.5-μm Ridge-Waveguide Laser Amplifier,» *Photonics Technology letters,* vol. 3, n°17, pp. 632-634, 1991.

[70] A. Ghazisaeidi et al, «Advanced C+L-Band Transoceanic Transmission Systems Based on Probabilistically Shaped PDM-64QAM,» vol. 35, n°17, 2017.

[71] M. K. Weldon, The Future X Network: A Bell Labs Perspective, CRC Press, 2016.

[72] P. Winzer, «Spatial multiplexing in fiber optics: The 10x scaling of metro/core capacities,» *Bell Labs Technical Journal,* p. 19:22–30, 2014.

[73] Wooram Lee et al, «Bidirectional WDM-PON Based on Gain-Saturated Reflective Semiconductor Optical Amplifiers,» *Photonics Technology Letters,* vol. 17, n°111, pp. 2460-2462, 2005.

[74] M Itoh et al, «Polarization-Insensitive SOA With a Strained Bulk Active Layer for Network Device Application,» *Photonics Technology letters,* vol. 14, n°16, pp. 765-767, 2002.

[75] N. Yoshimoto et al, «Four-channel polarization-insensitive SOA gate array integrated,» *Electronic Letters,* vol. 33, pp. 2045-2046, 1997.

[76] P. Doussiere et al, «1.55 um polarization independent semiconductor optical amplifier with 25 dB fiber,» *Photonic Technology Letters,* vol. 6, pp. 170-172, 1994.

[77] Z Zhu et al, «A Polarization Insensitive Semiconductor Optical Amplifier,» *Photonics technology letters,* vol. 28, n°117, pp. 1831-1834, 2016.

[78] M. Qiu et al, «Digital subcarrier multiplexing for fiber nonlinearity mitigation in coherent optical communication systems,» *OFC*, San Francisco, 2014.

[79] Agnès Verdier et al, «Wideband material for Low linewidth Widely Tunable Laser and Reach Extender for Optical Access Networks,» *Proc ECOC, M.1.C.2*, Gothenburg, 2017.

[80] K Carney et al, «Characterization of a Multi-Electrode Bulk-SOA for Low NF,» *ICTON*, 2010.

[81] K Carney et al, «Method to improve the noise figure and saturation power in multi-contact semiconductor optical amplifiers: simulation and experiment,» *Optics Express,* vol. 21, n°16, pp. 7180-7195, 2013.

[82] Riyam A. Johni et al, «Effects on Semiconductor Optical Amplifier Gain Quality for Applications in Advanced All-optical Communication Systems,» *Research Journal of Applied Sciences, Engineering and Technology,* vol. 7, n°116, pp. 3414-3418, 2014.

[83] P. Poggiolini et al, «Analytical results on system maximum reach increase through symbol rate optimization,» *OFC*, Los Ángeles, 2015.

[84] William Shieh et al, «Ultrahigh-Speed Signal Transmission Over Nonlinear and Dispersive Fibre Optic Channel: The Multicarrier Advantage,» *IEEE Photonics Journal,* pp. 276-283, 2010.

[85] P. Poggiolini et al, «Analytical and Experimental Results on System Maximum Reach Increase Through Symbol Rate Optimization,» *Journal of Lightware Technology,* vol. 34, n°18, pp. 1872-1884, 2016.

[86] A. Carbo et al, «Impact of Bandwidth Efficiency in Nonlinear Tolerance of Multicarrier Modulations,» *Journal of lightwave technology,* vol. 34, n°18, 2016.

[87] G. Bosco et al, «Impact of the Transmitter IQ-Skew in Multi-Subcarrier Coherent Optical Systems,» *OFC*, Anaheim, 2016.

[88] E. P. Guiomar et al, «Combining Probabilistic Shaping and Nonlinear Mitigation: Potential Gains and Challenges,» *OFC*, San Diego, 2018.

[89] E.P. Guiomar et al, «Nonlinear mitigation on subcarrier-multiplexed PM-16QAM optical systems,» *Optics express,* vol. 24, n°14, pp. 4298-4311, 2017.

[90] M. P. Yankov et al, «Phase Noise Compensation for Nonlinearity-Tolerant Digital Subcarrier Systems With High-Order QAM,» *IEEE Phothonics Journal,* vol. 9, n°15, 2017.

[91] Ronen Dar et al, «Digital Subcarrier Multiplexing in Optically Routed Networks,» *OFC*, 2017.

[92] Statista, «Number of monthly active Facebook users worldwide as of 4th quarter 2017 (in millions),» https://www.statista.com/statistics/264810/number-of-monthly-active-facebook-users-worldwide/, 2018.

[93] A. Ghazisaeidi, «A Theory of Nonlinear Interactions Between Signal and Amplified Spontaneous Emission Noise in Coherent Wavelength Division Multiplexed Systems,» *JLT,* vol. 35, n°123, pp. 5150-5175, 2017.

[94] Thomas Richter et al, «Comparison of WDM Bandwidth Loading Using Individual Transponders, Shaped, and Flat ASE Noise,» *OFC*, San Diego, 2018.

[95] D.J. Richardson et al, «Space-division multiplexing in optical fibres,» *Nature Photonics.*

[96] A. Nespola et al, «Effectiveness of Digital Back-Propagation and Symbol-Rate,» *OFC*, Anaheim, 2016.

[97] M. Morelli and U. Mengali, «Feedforward frequency estimation for PSK: A tutorial review,» *Eur. Trans. Telecommun.,* vol. 9, n°12, p. 103–116, 1998.

Publications

As first author

[I] A. Carbo et al, “Experimental Analysis of Non Linear Tolerance Dependency of Multicarrier Modulations versus Bandwidth Efficiency”, Proc. ECOC, Th.2.6.6, Valencia, 2015

[II] A. Carbo et al, “Impact of Bandwidth Efficiency in Nonlinear Tolerance of Multicarrier Modulations”, Journal of lightwave technology. Vol 34, Issue 8, 2016

[III] A. Carbo et al, “Experimental Analysis of Non Linear Tolerance Dependency of Multicarrier Modulations versus Number of WDM”, Proc. OFC, Tu3A.6, Anaheim, 2016

As co-author

[IV] A. Ghazisaeidi et al, “65Tb/s Transoceanic Transmission Using Probabilistically- Shaped PDM-64QAM”, Proc ECOC, Th.3.C.4, Düsseldorf, 2016

[V] A. Ghazisaeidi et al, “Advanced C+L-Band Transoceanic Transmission Systems Based on Probabilistically Shaped PDM-64QAM”, Vol 35, Issue 7, 2017

[VI] J. Renaudier et al, “First 100-nm Continuous-Band WDM Transmission System with 115Tb/s Transport over 100km Using Novel Ultra-Wideband Semiconductor Optical Amplifiers”, Proc ECOC, Th.PDP.A.3, Gothenburg, 2017

[VII] J. Renaudier et al, “Data-Center Interconnect Field Trial of 100nm Ultra-Wideband Optical Transport with 42GBd 16QAM Real-Time and 64GBd PCS64QAM Channels”, Proc ECOC, submitted, Rome, 2018

[VIII] Agnès Verdier et al, “Wideband material for Low linewidth Widely Tunable Laser and Reach Extender for Optical Access Networks”, Proc ECOC, M.1.C.2, Gothenburg, 2017